



**UNIVERSITY OF
KWAZULU-NATAL**

**INYUVESI
YAKWAZULU-NATALI**

CONSIDERATION OF THE EFFECTS OF SYMMETRICAL AND ASYMMETRICAL
VOLTAGE DIPS IN THE CONTROL AND OPERATION OF A GRID-CONNECTED
DOUBLY-FED INDUCTION GENERATOR

Khanyisani Makhoba

212520932

A thesis submitted to
the University of KwaZulu-Natal,
College of Agriculture, Engineering and Science,
in partial fulfillment of the requirements for the degree of

Master of Science

Supervisor: Prof David Dorrell

School of Engineering

University of KwaZulu-Natal

March 2020

Copyright © 2020 Khanyisani Makhoba

All Rights Reserved

I, Khanyisani Makhoba , declare that:

- (i) The research reported in this thesis, except where otherwise indicated, is my original research.
- (ii) This thesis has not been submitted for any degree or examination at any other university.
- (iii) This thesis does not contain other persons' data, pictures, graphs or other information, unless specifically acknowledged as being sourced from other persons.
- (iv) This thesis does not contain other persons' writing, unless specifically acknowledged as being sourced from other researchers. Where other written sources have been quoted, then:
 - a) their words have been re-written but the general information attributed to them has been referenced:
 - b) where their exact words have been used, their writing has been placed inside quotation marks, and referenced.
- (v) This thesis does not contain text, graphics or tables copied and pasted from the Internet, unless specifically acknowledged, and the source being detailed in the dissertation/thesis and in the References sections.

Candidate: Khanyisani Makhoba

Signature:  _____

As the candidate's supervisor I agree to the submission of this thesis for examination.

Supervisor: Prof David Dorrell

Signature:  _____

ABSTRACT

CONSIDERATION OF THE EFFECTS OF SYMMETRICAL AND ASYMMETRICAL VOLTAGE DIPS IN THE CONTROL AND OPERATION OF A GRID-CONNECTED DOUBLY-FED INDUCTION GENERATOR

Khanyisani Makhoba
School of Engineering
Master of Science

Grid integration of Type 3 Wind Energy Conversion Systems (WECS) based on the doubly-fed induction generator (DFIG) is a great challenge since the direct connection of the stator side to the grid makes it susceptible to loss of control and rotor over-voltages during voltage dips. Without effective countermeasures in place, this can result in the fatal failure of the power electronic converter. This thesis presents a selective study of the behaviour of Type 3 WECS based on DFIG under symmetrical and asymmetrical voltage dips. As part of the mitigation strategies, a crowbar protection scheme, demagnetizing current control and dual vector control are studied in this thesis.

The main findings are drawn from a MATLAB/Simulink simulation model of a 2 MW, 690 V DFIG. This software platform offers built-in power electronic device models; therefore, the study is mainly focused on the control aspects of the DFIG. The fault ride-through (FRT) capability of the 0.8 kW DFIG test bench is also analyzed in this research. It is deduced that it is possible to control a DFIG WECS during voltage dips that are less than 32 % in depth by solely using the traditional dual vector control technique. Voltage dips greater than 32 % result in the saturation of the power electronic converter and loss of control. As part of the mitigation strategies developing in this study, it was found that the combined control of the demagnetizing current and the injection of a backwards rotating flux produced excellent results.

Keywords: DFIG, control, asymmetrical, symmetrical, FRT, demagnetizing

PUBLICATIONS ARISING

CONSIDERATION OF THE EFFECTS OF SYMMETRICAL AND ASYMMETRICAL
VOLTAGE DIPS IN THE CONTROL AND OPERATION OF A GRID-CONNECTED
DOUBLY-FED INDUCTION GENERATOR

Khanyisani Makhoba
School of Engineering
Master of Science

D. G. Dorrell and K. Makhoba, Detection of inter-turn stator faults in induction motors using short-term averaging of forward and backward rotating stator current phasors for fast prognostics, *IEEE Trans. Magn.*, vol. 53, no. 11, Nov. 2017, Art. no. 1700107.

ACKNOWLEDGMENTS

The author of this thesis would like to acknowledge excellent work which has been done by researchers of the studied pieces of literature as listed in the bibliography. More importantly, the author must acknowledge the Director of the EPPEI Specialization Centre in HVDC at UKZN, Prof David Dorrell, and the team for realizing this study. Also, the School of Engineering at the University of KwaZulu-Natal for the intellectual resources used during the course of this study.

Contents

| | |
|--|-------------|
| Table of Contents | xi |
| List of Figures | xvii |
| List of Tables | xxi |
| 1 Introduction | 1 |
| 1.1 Problem Statement | 1 |
| 1.2 Background | 2 |
| 1.2.1 WECS in South Africa | 2 |
| 1.3 DFIG WECS Overview | 3 |
| 1.3.1 Components of DFIG WECS | 4 |
| 1.4 Objectives and Limitations | 6 |
| 1.4.1 Objectives | 6 |
| 1.4.2 Limitations | 6 |
| 1.5 Preliminary Research | 7 |
| 1.6 Main Research | 7 |

| | | |
|----------|--|----------|
| 1.7 | Outline of Thesis Chapters | 8 |
| 2 | Literature Review | 9 |
| 2.1 | Introduction | 9 |
| 2.2 | Grid Code | 10 |
| 2.2.1 | Background | 10 |
| 2.2.2 | Germany Grid Code | 10 |
| 2.2.3 | South Africa Grid Code | 11 |
| 2.2.4 | FRT Capability | 12 |
| 2.2.5 | Reactive Power Control | 13 |
| 2.3 | WECS Overview | 14 |
| 2.3.1 | Types of Commercial WECS | 15 |
| 2.3.2 | Summary | 17 |
| 2.4 | The BTB Converter | 18 |
| 2.5 | Control Techniques Overview | 19 |
| 2.5.1 | Vector Control | 19 |
| 2.5.2 | Direct Torque Control (DTC) | 20 |
| 2.5.3 | Model Predictive Control (MPC) | 20 |
| 2.6 | Voltage Dips | 21 |
| 2.6.1 | Severity of Voltage Dips | 21 |
| 2.6.2 | Symmetrical Voltage Dips | 22 |
| 2.6.3 | Impact of Asymmetrical Voltage Dip | 24 |

| | | |
|----------|--|-----------|
| 2.6.4 | Summary | 26 |
| 2.7 | Software Solutions | 26 |
| 2.7.1 | Demagnetizing Current Injection | 26 |
| 2.7.2 | Dual Control of Rotor Currents | 27 |
| 2.8 | Consideration of Unbalanced Grid | 28 |
| 2.8.1 | Decomposition of the Reference Frame | 28 |
| 2.8.2 | Symmetrical Components | 31 |
| 2.8.3 | Signal Delay Cancellation Method | 33 |
| 2.9 | Hardware Solutions | 34 |
| 2.9.1 | Crowbar Protection | 35 |
| 2.9.2 | Series Dynamic Resistor | 36 |
| 2.9.3 | Reliability of the Mitigation Strategies | 36 |
| 2.10 | Power Capability of DFIG | 37 |
| 2.10.1 | Modes of operation | 37 |
| 2.10.2 | Limitations of Deliverable Power | 39 |
| 2.11 | Steady State Operation of DFIG | 40 |
| 2.11.1 | Equivalent Circuit | 40 |
| 2.11.2 | Steady-State Power Flow | 42 |
| 2.11.3 | Summary | 44 |
| 3 | Modelling | 47 |
| 3.1 | Dynamic Model | 47 |

| | | |
|----------|--|-----------|
| 3.1.1 | Voltage Equations | 47 |
| 3.2 | Frames of Reference | 50 |
| 3.2.1 | Introduction | 50 |
| 3.2.2 | Natural Reference Frame (abc - axis) | 50 |
| 3.2.3 | Stationary Reference Frame ($\alpha\beta$ - axis) | 51 |
| 3.2.4 | Synchronous Rotating Frame (dq - axis) | 51 |
| 3.2.5 | Transformation of Reference Frames | 52 |
| 3.3 | Vector Control of DFIG | 53 |
| 3.3.1 | Introduction | 53 |
| 3.3.2 | Grid Synchronization | 53 |
| 3.3.3 | Alignment of Reference Frame | 54 |
| 3.4 | Vector Control of the GSC | 55 |
| 3.4.1 | Outer Control Loop | 55 |
| 3.4.2 | Inner Current Control Loop | 58 |
| 3.5 | Control of the RSC | 60 |
| 3.5.1 | Outer Control Loop | 60 |
| 3.5.2 | Inner Current Control Loop | 62 |
| 3.5.3 | GSC Current Reference Under Asymmetrical Dips | 65 |
| 3.5.4 | Demagnetizing Current Control | 67 |
| 3.5.5 | Control Targets for RSC Under Asymmetrical Dips | 68 |
| 4 | Simulation and Simulation Results | 69 |

| | | |
|----------|---|------------|
| 4.1 | Simulation Procedure | 69 |
| 4.1.1 | Equipment and Software | 70 |
| 4.1.2 | Apparatus and Procedure | 70 |
| 4.1.3 | Computer Simulation | 75 |
| 4.1.4 | Concluding Remarks | 77 |
| 4.2 | Simulation Results | 77 |
| 4.3 | Effects of Symmetrical Voltage Dips | 78 |
| 4.4 | Damping of Natural Flux | 79 |
| 4.5 | Effects of Asymmetrical Voltage Dips | 82 |
| 4.5.1 | Mitigation Methods | 82 |
| 4.6 | Laboratory Experimental Results | 92 |
| 4.7 | Discussion | 96 |
| 5 | Conclusion and Recommendations for Further Studies | 99 |
| 5.1 | Conclusion | 99 |
| 5.2 | Recommendations for Further Studies | 100 |
| A | Formulae | 109 |
| A.1 | Constants | 109 |
| A.2 | Control targets for the RSC under unbalanced grid voltage | 110 |
| B | Parameters and Variables | 113 |
| B.1 | DFIG parameters | 113 |

| | |
|--------------------------------|------------|
| C Additional Results | 117 |
| D Diagrams and Circuits | 123 |

List of Figures

| | | |
|------|---|----|
| 1.1 | Type 3 WECS based on DFIG | 4 |
| 2.1 | South African LVRT requirements for the RPPs of category A3, B and C | 12 |
| 2.2 | South African requirements for reactive power support, I_Q , during voltage drops or peaks [14] | 13 |
| 2.3 | Classification of wind energy conversion generators | 14 |
| 2.4 | Full-scale converter WECS based on PMSG | 17 |
| 2.5 | Model of a full-switched back-to-back converter | 18 |
| 2.6 | DFIG flux trajectory under symmetrical voltage dips | 23 |
| 2.7 | Sequence decomposition of the synchronous reference frame [12] | 29 |
| 2.8 | Effect of asymmetrical grid voltage on stator and rotor current and electromagnetic torque | 30 |
| 2.9 | Sequence composition during 60 % single-phase asymmetrical voltage dip | 31 |
| 2.10 | Sequence decomposition of unbalanced three-phase system | 32 |
| 2.11 | Signal delay cancellation block diagram | 34 |
| 2.12 | Signal delay cancellation method output in dq reference frame | 34 |

| | |
|---|----|
| 2.13 Low voltage ride-through protection system, comprising of an SDR and crowbar protection scheme | 35 |
| 2.14 Power flow in DFIG wind energy conversion system | 39 |
| 2.15 The transition between subsynchronous and super-synchronous modes of operation | 39 |
| 2.16 Steady-state equivalent circuit of the DFIG | 40 |
| 2.17 Stator referred per-phase steady-state equivalent circuit of a DFIG | 41 |
| 3.1 Idealized winding model of an induction machine | 48 |
| 3.2 Reference frame transformation | 52 |
| 3.3 SRF PLL diagram | 54 |
| 3.4 Alignment of d-q reference frame with the stator flux space vector | 55 |
| 3.5 Inner current control loops of the grid side converter | 58 |
| 3.6 PI regulator of the inner current loops of the GSC | 59 |
| 3.7 Control block diagram of the Rotor side converter under normal grid conditions . . | 62 |
| 3.8 PI regulator of the inner current loops | 64 |
| 3.9 Combined injection of demagnetizing and negative sequence current | 68 |
| 4.1 Dynamic grid fault simulator of the machine test bench | 72 |
| 4.2 Lucas Nuelle DFIG machine test bench at the Smart grid laboratory | 73 |
| 4.3 PC based Fault Ride-Through Monitor | 74 |
| 4.4 DFIG implementation in MATLAB/Simulink | 76 |
| 4.5 Wind turbine Simulink block | 77 |
| 4.6 Total symmetrical voltage dip without protection | 78 |

| | | |
|------|---|----|
| 4.7 | Partial (60%) symmetrical voltage dip without protection | 79 |
| 4.8 | Crowbar protection under a total (100 %) symmetrical voltage dip. | 80 |
| 4.9 | Crowbar protection under a partial (60 %) symmetrical voltage dip. | 81 |
| 4.10 | DFIG Simulation under 20 % (non-severe) symmetrical voltage dip with traditional vector control | 82 |
| 4.11 | DFIG Simulation under 20 % (non-severe) symmetrical voltage dip with demagnetizing current control | 83 |
| 4.12 | DFIG Simulation under 60 % (severe) symmetrical voltage dip with traditional vector control | 84 |
| 4.13 | DFIG Simulation under 60 % (severe) symmetrical voltage dip with demagnetizing current injection | 85 |
| 4.14 | DFIG LVRT Simulation under 60 % severe symmetrical voltage dip with Crowbar protection and reactive power control | 86 |
| 4.15 | DFIG Simulation under 25 % (non-severe) asymmetrical voltage dip with traditional vector control | 87 |
| 4.16 | DFIG Simulation under 25 % (non-severe) Asymmetrical voltage dip with demagnetizing current control | 88 |
| 4.17 | DFIG Simulation under 65 % (severe) asymmetrical voltage dip with traditional vector control | 89 |
| 4.18 | DFIG Simulation under 45 % severe asymmetrical voltage dip with demagnetizing current control | 90 |
| 4.19 | DFIG Simulation under 45 % (severe) asymmetrical voltage dip with combined crowbar protection and dual vector control | 91 |
| 4.20 | Experimental DFIG under 20 % (non-severe) symmetrical voltage dip | 92 |
| 4.21 | Experimental DFIG LVRT under 60 % (severe) symmetrical voltage dip | 93 |
| 4.22 | Experimental DFIG under 20-60-60 % (non-severe) Asymmetrical voltage dip . . . | 94 |

| | |
|--|-----|
| 4.23 Experimental DFIG LVRT under 40-20-60 % (severe) Asymmetrical voltage dip | 95 |
| C.1 Locus diagrams for different limitations in pu system | 118 |
| C.2 Steady state capability in pu of 2 MW DFIG with $Q_s = 0$ and $i_{dr} = 0$ magnetizing strategies | 119 |
| C.3 Dynamic response under wind speed step change from subsynchronous to super-synchronous mode | 120 |
| C.4 Dynamic response of dq currents under wind speed step change from subsynchronous to super-synchronous mode | 121 |
| D.1 Power flow in DFIG wind energy conversion system | 123 |
| D.2 RSC complete control diagram | 124 |
| D.3 Rotor side circuit diagrams under voltage dips | 125 |
| D.4 South African grid code LVRT requirement for RPPs of category A1 and A2 | 126 |

List of Tables

| | | |
|-----|--|-----|
| 2.1 | Quadrants of GSC operation based on power factor [2] | 44 |
| 3.1 | GSC controller parameters | 58 |
| 3.2 | RSC controller parameters | 64 |
| B.1 | DFIG parameters for MATLAB/Simulink [®] simulation [34] | 114 |
| B.2 | GSC simulation parameters | 114 |
| B.3 | Test bench generator nameplate ratings | 115 |

Acronyms

BTB back-to-back converter. 5, 53, 69

DFIG doubly-fed induction generator. 1, 3, 9

FRT fault ride-through. 16

GSC grid side converter. 55

REIPPPP Renewable Energy Independent Power Producer Procurement Program. 2, 3

RPP renewable power plant. 3

RSC rotor side converter. 19, 25

SAREGC South African Renewable Energy Grid Code. 3

SAWEA South African Wind Energy Association. 2

SDC signal delay cancellation. 75

SDR series dynamic resistor. 36

SFOC stator flux oriented control. 19

SVOC stator voltage oriented control. 19

VSWT variable speed wind turbines. 3

WECS wind energy conversion system. 1, 2, 14

Nomenclature

Subscripts

- 1 Positive sequence
- 2 Negative sequence
- α alpha axis
- β beta axis
- d d axis
- dc DC link variable; can be denoted by *bus*
- g Grid side variable; can be denoted by *gsc*
- q q axis
- r Rotor side variable
- s Stator side variable

Superscripts

- * Controller reference
- + Positive sequence
- Negative sequence

Variables

- ω_m Mechanical speed in (rad/s)
- ω_r Slip frequency

| | |
|-------------|-----------------------|
| ω_s | Synchronous frequency |
| ω_n | Natural frequency |
| ψ | flux |
| ψ_{sn} | Natural flux |
| ζ | Damping ratio |
| i | current |
| i_{rn} | Demagnetizing current |
| L | Inductance |
| R | Resistance |
| v | voltage |

Chapter 1

Introduction

1.1 Problem Statement

Global warming due to the burning of fossil fuel, the ever-rising cost of oil and gas is forcing society to move away from conventional methods of electrical power generation and look closely at cleaner ways of generating electricity. South Africa has experienced a crisis with delays in construction of new power stations, poor maintenance of current power stations, and a rising population, leading to major issues such as load shedding, rising electricity tariffs and environmental concerns [1]. The rapid increase in demand for renewable energy technologies calls for research and development in this area. Many Western countries have invested in renewable source such as wind and solar power and South Africa is now following a similar course.

Amongst renewable energy technologies, the Type 3 wind energy conversion system (WECS) based on doubly-fed induction generator (DFIG) is attractive and popular due to reduced cost,

weight/kW and nacelle space requirements [2]. Grid integration of this type of WECS is, however, a significant challenge since the direct connection of the stator side to the grid makes it susceptible to loss of control during voltage dips [3]. This leads to infringement of grid codes and can result in frequent occurrence of failures in wind farms. Under such conditions the performance of the nationally integrated power system is compromised, this then needs more attention.

1.2 Background

1.2.1 WECS in South Africa

South Africa's geographical location, topography and size affords the development of multiple renewable energy resources, including wind energy. Approximately 3000 km of coastline with warm tropical climate provides suitable conditions for wind power generation throughout the country [4]. Government, with the aid of agencies across the globe, have provided technical studies and empirical evidence concerning the quality and quantity of renewable energy resources. The establishment of the Renewable Energy Independent Power Producer Procurement Program (REIPPPP) has resulted in a significant increase in renewable energy projects in South Africa [1].

South Africa is currently sourcing its electrical energy from Eskom, 85.8 % of which is derived from coal-powered generation stations [1]. Renewable energy technologies only account for 4.5 % of the installed capacity. However, the government has endorsed the exploration of renewable energy sources through the REIPPPP [5]. According to the report released by the South African Wind Energy Association (SAWEA) South Africa is sitting at 22 fully operational wind farms (2020 MW installed capacity) with 11 wind farms in construction (1391.8 MW) as of March 2019

[4].

The REIPPPP is a South Africa tender process aimed at supporting grid-connected renewable energy by procuring clean electrical energy from the Independent Power Producers (IPPs). The REIPPPP is facilitated with the South African Renewable Energy Grid Code (SAREGC) to ensure that renewable power plant (RPP) connected to South African transmission or distribution system comply with the coupling point technical requirements. This is to ensure grid stability and consumer power quality [2] [5] [6].

1.3 DFIG WECS Overview

Amongst the forms of renewable energy wind energy is considered to be the most reliable source due to its high availability in nature [7]. However, the challenge comes with the fact that wind is very variable both geographically and temporally. The variability occurs over a vast range of scales, both in space and time and the variations not do not always correspond with the consumption [8]. In order to overcome this challenge wind energy is harnessed utilizing variable speed wind turbines (VSWT) which are based on DFIG. The DFIG shown in Figure 1.1 is designed for optimum power production under considerable wind fluctuations [9].

Harnessing of wind energy is still sophisticated and contains weaknesses that retard its operation. The harnessing involves the need for extensive suitable land, which might in some cases require the expropriation of land from communities, the ratio between technology size and its power output as well as the production and availability of spare parts worldwide for maintenance. Other drawbacks of wind energy technologies are outlined in [10]. It is therefore imperative for all engineering fields

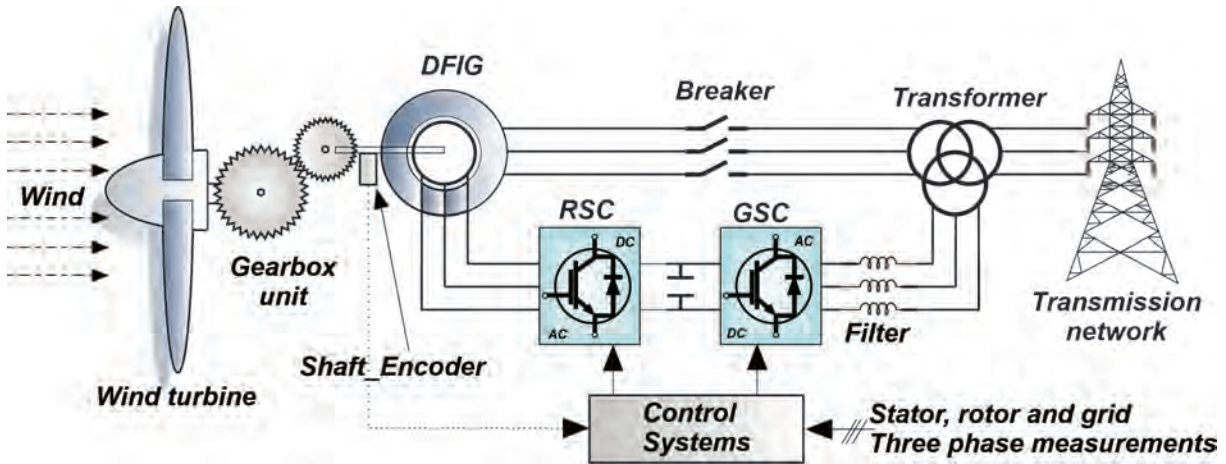


Figure 1.1 Type 3 WECS based on DFIG

at an industrial and academic level to provide adequate material and design of compact components in order to improve the technology [10].

1.3.1 Components of DFIG WECS

Induction generator

The DFIG WECS system studied in this work is shown in Figure 1.1 incorporates a wound rotor induction machine which operates as a generator by applying negative torque to the main shaft. The stator terminals are connected to the grid via a transformer while the rotor terminals are connected to a back-to-back bidirectional converter through slip rings [9], [11], [12].

Back-to-back converter

DFIG rotor terminals exchange power with the grid via a four-quadrant power electronic converter (DC-AC converter and a rectifier connected back-to-back). The dc bus acts as intermediate energy storage to smooth the power flow between the converter. The most popular topology used for a medium size DFIG is a 2-level BTB that incorporates the IGBTs [2].

Transformer

The step-up transformer is necessary to boost the low-voltage side levels (typically 575 and 690 V) to the voltages of the wind farm collection point (typically 33 kV).

Mechanical system

The rotor speed of the wind turbine must be step up to the speed ranges of the generator, and the gearbox unit realizes this. The gearbox ratio is influenced by several factors such as nominal wind speed and the number of pole-pairs of the generator [13].

Excessive wind can damage the wind turbine mechanical system and cause undesirable transients to the electrical system. The pitch is therefore necessary for curtailment of excessive power production during gusts of wind. It is also used for power extraction optimization from a wind turbine. Here all blades are pitched simultaneously or independently in order to provide more degrees of freedom to the system [9].

1.4 Objectives and Limitations

1.4.1 Objectives

The main objective of this study is to deal with the impact of voltage dips on the control system of a DFIG to protect the power electronic converter and help mitigate the infringement of the grid connection code.

1. To investigate the performance challenges of DFIG under voltage dips and identify the causes and solutions to those challenges.
2. To implement an effective computational model of DFIG control system that mitigates the impact of both symmetrical and asymmetrical voltage dips based software and hardware solutions.

1.4.2 Limitations

1. The DFIG's power circuit and its control systems are implemented in the simulation environment, and numerous assumptions are made in order for the computational analysis to be feasible.
2. Under asymmetrical voltage dips, only single-phase to ground fault is considered.
3. The converter models, modulation techniques and aerodynamics of the wind turbine are not in the scope of the objectives as mentioned earlier and are therefore not studied in this research thesis.

-
4. The machine parameters used in the computational model are from the literature. It was not possible, in as far as reasonably practicable, to acquire the exact parameters of the start-of-the-art DFIG system due to its compact design.

1.5 Preliminary Research

The preliminary research pertains to the ordinary aspects of DFIG grid integration; this includes the control analysis of the BTB and implementation of closed-loop control in the absence of voltage dips. This acts as a foundation from which the software and hardware mitigation methods are built upon. The power flow analysis at steady-state is also carried out in a preliminary fashion in order to study and comprehend the limitations of deliverable power in a DFIG WECS. This gives an insight into the behaviour of the DFIG under varying slip ratio, and the influence of grid voltage dips.

1.6 Main Research

The main research looks closely at the negative impacts of grid voltage dips on the operation of the DFIG and studies how the mitigation strategies impact operation in order to comply with the grid connection code. Here the fault ride-through capability and reactive power control during the voltage dips as demanded by the grid connection code are studied and simulated.

The asymmetrical voltage dip of type "Single-phase to ground" has been chosen for the simulation, and it is alone sufficient to cover the scope of this study.

1.7 Outline of Thesis Chapters

Chapter 1 introduces the main research questions. It gives the background of renewable energy generation and Wind Energy Conversion Systems (WECS), and importance and relevance of the topic to contemporary power generation industry. Here the scope of the research is stated in terms of aims, objectives and limitations.

Chapter 2 provides the literature background on the grid connection code; overview of wind energy conversion systems; a brief overview of control techniques; the effects of voltage dips on the operation of DFIG WECS and countermeasures to those effects.

Chapter 3 is the preliminary part of this research. The dynamic modelling, control and analysis of DFIG WECS under normal grid conditions is covered in this chapter.

Chapter 4 forms the basis of this study. The countermeasures discussed in Chapter 2 are implemented in the simulation environment, and the main results are graphically presented and discussed.

Chapter 5 gives some concluding remarks on the main findings and the overall success of the study. The recommendations for future research are given at the end of this chapter.

Chapter 2

Literature Review

2.1 Introduction

The preliminary chapter of [2] provides more details on the historical background and evolution of the configurations in wind energy conversion systems. It further gives classification and a comparative study of these types based on cost-benefit analysis acquired according to speed range and power electronic converter capacity. Mathematical modeling and control of the doubly-fed induction generator (DFIG) converter is covered in [3] while [12] gives more guidance in terms of controller design and stability. The grid connection code for renewable power plants connected to the electricity transmission or the distribution system in South Africa in [14] provides the standards under which transmission system operators (TSO) and distribution system operators (DSO) should operate.

2.2 Grid Code

2.2.1 Background

Grid codes have been developed and enforced in many countries for many years. They ensure the application of uniform standards for power systems in order to meet various technical requirements that include system stability, consumer power quality and economical operation of the power system. They are updated regularly by TSO and DSO since they are usually based on experience acquired through operation [15].

Many countries have updated grid codes to address the issues concerning renewable energy power generation. According to the grid codes, wind plants must operate in a similar way to a conventional power generation plant. They dictate that a wind plant shall remain in operation under abnormal grid conditions by giving tolerance to variation of grid voltage and frequency within prescribed boundaries [2] [15].

2.2.2 Germany Grid Code

Germany's grid connection code concerning the operation of wind turbines is discussed in [16]. The literature was published in 2005, during which Germany had experienced a continuously increasing feed-in of wind power to the transmission networks. This was not compatible with the utility of the time and, therefore, TSOs had to engage in intensive research on necessary network measures and operational requirements to tackle challenges of the future.

In 2010, another paper concerning the dynamic response of wind turbines in relation to Germany's grid code was published [17]. Here the voltage support and timing requirements of the grid code were assessed, and a new voltage control method was proposed to meet new needs.

2.2.3 South Africa Grid Code

The connection to the South African national grid is regulated by SAGC whose primary objective is to specify the minimum technical requirements for RPPs connected or seeking connection to the South African transmission system or distribution system. The grid code is applied to various RPP technologies, and this paper only focuses on wind energy technology [15].

The grid connection code for renewable power plants stipulates that the compliance to the grid code shall be applicable to RPPs depending on its rated power and, where indicated, the nominal voltage at POC (Point of Connection). The RPPs are, therefore, grouped into three main categories:

- (a) Category A: 0 to 1 MVA This category includes RPPs with a rated power of less than 1 MVA and connected to a LV voltage. It is further divided into three sub-categories:
 - (i) Category A1; 0 to 13.8 kVA
 - (ii) Category A2; 13.8 kVA to 100 kVA
 - (iii) Category A3; 100 kVA to 1 MVA
- (b) Category B: 1 MVA to 20 MVA
- (c) Category C: 20 MVA and higher

For the purpose of this work, a category A3 wind farm model is used. The voltage ride-through requirements for Categories A3, B and C is shown in Figure 2.1 [14].

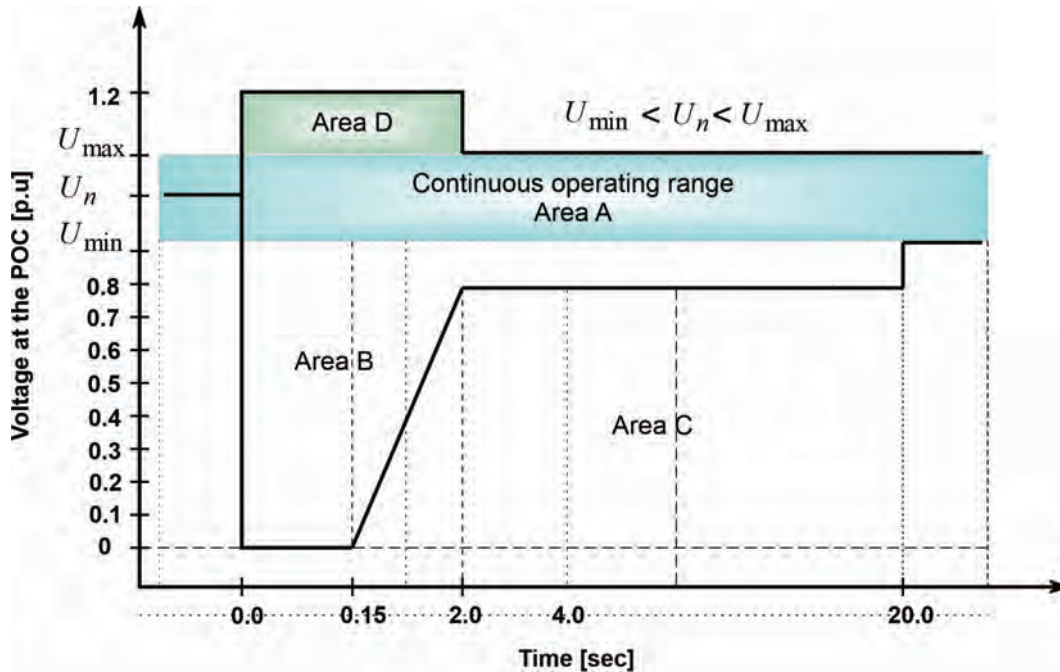


Figure 2.1 South African LVRT requirements for the RPPs of category A3, B and C [14]

2.2.4 FRT Capability

Disconnection of large-scale wind power generation units due to grid disturbances such as voltage dips and swells is inevitable. The sudden disconnection of generation units stimulates the instability of the utility network. The fault duration depends on the protection device response to discriminate and clear the fault, and this is usually in the range of milliseconds. The fault ride-through philosophy is that during a grid fault, a generating unit must remain connected and only disconnect if the fault is sustained longer than the specific period as graphically presented in Figure 2.1 [2]-[15].

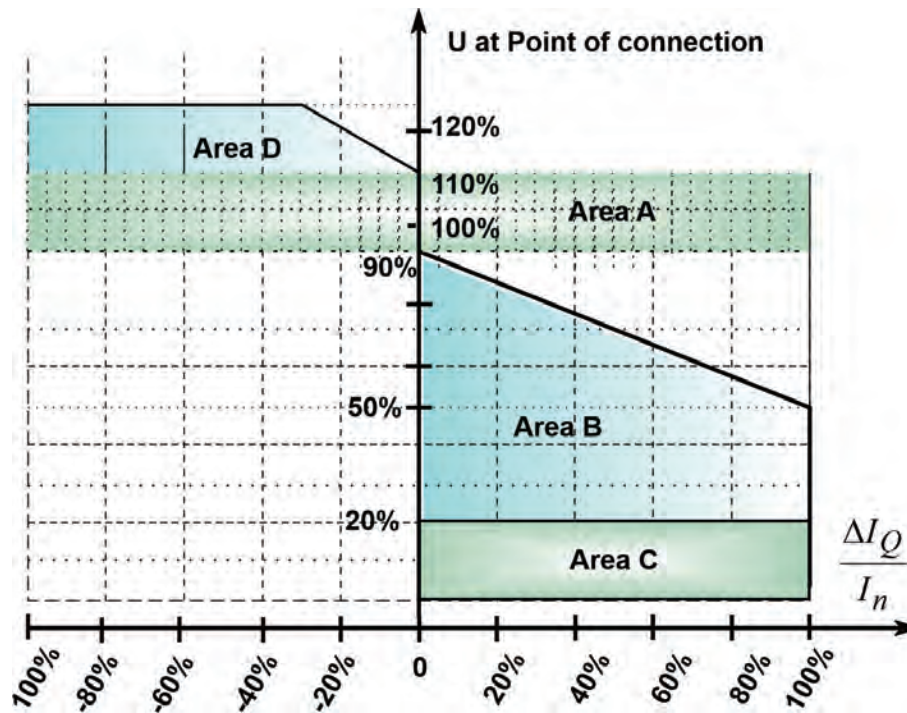


Figure 2.2 South African requirements for reactive power support, I_Q , during voltage drops or peaks [14]

During the fault period, an excessive amount of energy remains trapped within the DFIG system resulting in over-current in the induction generator circuits and over-voltage in the DC link of the power electronic converter. To improve the low voltage ride-through (LVRT) of the DFIG, methods have been studied as reported in the literature [18] [19].

2.2.5 Reactive Power Control

Like any other conventional power plant, a wind farm must be capable of providing reactive power control to the grid during both steady-state and transient conditions [20]. Reactive power control helps to continually compensate for inductive components of the grid such as cables and trans-

formers, and inductive loads, and to maintain the voltage stability. Wind energy conversion systems (WECS) must also provide reactive power during grid faults in order to support grid voltage recovery, the grid code related to this is shown in figure 2.2.

2.3 WECS Overview

There is a wide variety of commercial wind energy generation systems, which are characterised using the design and configuration of a wind turbine, gearbox, generator and power electronic converter. The use of partial scale and full-scale converters presents distinct variability over other commercial WECS. It further shows the popularity of each WECS configuration in the wind energy industry, where DFIG is found to have the highest market share than other WECS configuration [2].

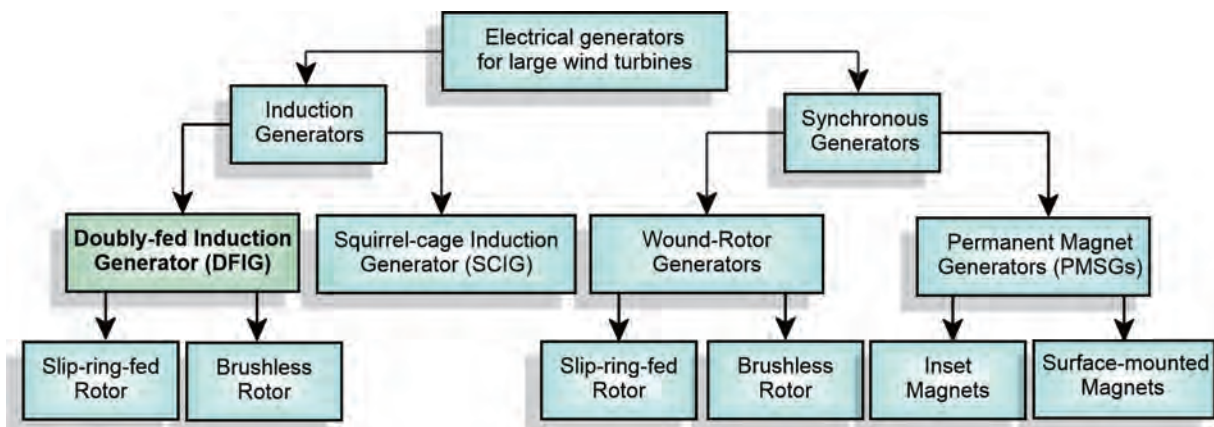


Figure 2.3 Classification of wind energy conversion generators [15]

2.3.1 Types of Commercial WECS

Type 1 WECS configuration

A squirrel cage induction generator (SCIG) is connected to the grid via a soft starter and a step-up transformer. This very first wind technology known as "Danish" concept was developed around the 1980s. It has 1 % speed range, therefore lower wind energy conversion efficiency. The fault ride through is only possible by employing external hardware. With this type of configuration, the transients in the electrical side directly translate to mechanical stresses on the parts of the wind turbine. The rapid changes in wind speeds cause grid frequency stability issues. Despite the drawbacks as mentioned earlier, this simple configuration is viable in terms of initial and maintenance cost due to the use of inexpensive soft starter [2].

Type 2 WECS Configuration

This type seeks to overcome some drawbacks of Type 1 WECS configuration utilizing the semi-variable speed wind turbine based on a wound rotor induction generator (WRIG). This configuration has been on the market since the 1990s, and it incorporates a partially rated power electronic converter to allow for 10 % speed variation. A converter-controlled external resistor regulated the speed/torque characteristic. As a result, it has a lower impact on grid frequency and mechanical stress. Although a higher conversion efficiency is attained, these systems still have not yet eliminated the use of a soft starter. Also, it presents a high initial cost for the converter and operational cost related to the maintenance of slip rings and brushes for WRIG [2].

Type 3 WECS Configuration

The doubly-fed induction generator (DFIG) is a Type 3 WECS configuration. With a market share of about 50 % DFIG is one of the dominating technologies in modern wind energy conversion. This research covers the operational concepts of this type of WECS [2].

Type 4 WECS Configuration

To achieve variable speed operation for the entire speed range Type 4 WECS configuration was established in the 1990s. Unlike type 3 configuration, type 4 power electronic converter is connected directly between the stator terminals and the grid, allowing the utility to process 100 % of stator power output. This fully isolates the generator from the grid. Independent power factor control leads to guaranteed FRT compliance [2].

The system uses various generators: PMSG, SCIG, WRSG, and HTS-SG for electro-mechanical conversion with the PMSG being the most popular. Although the deployment of full-scale power electronic converter realizes full-variable speed operation (0 % to 100 %), the increase in nacelle space requirements, initial cost, the complexity of digital control and higher converter power losses makes this less economical than Type 3 [2]. A typical full-scale converter WECS is shown in Figure 2.4 .

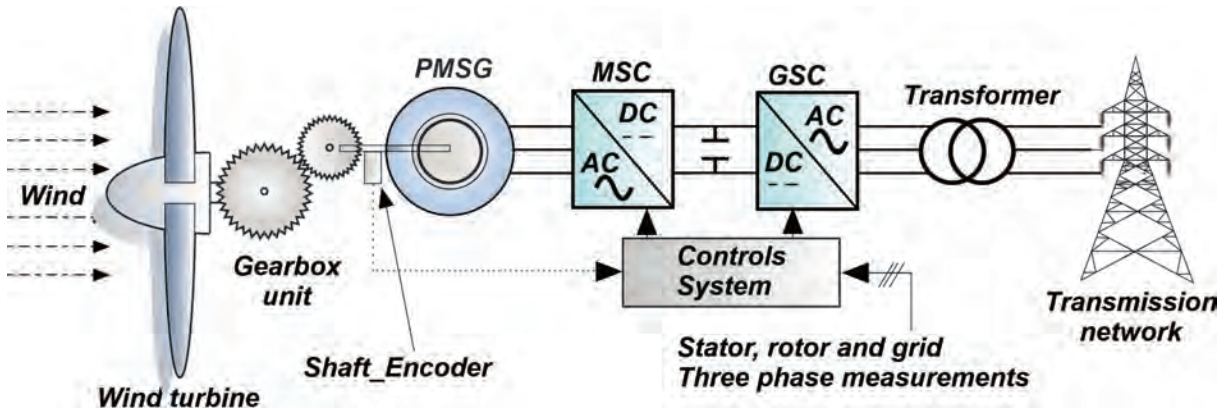


Figure 2.4 Full-scale converter WECS based on PMSG [2]

2.3.2 Summary

The utilization of a partial scale converter leads to the reduction of costs, specific weight (kg/W) and nacelle space requirements. With a variable speed operation, a DFIG can harvest more energy from the wind than a fixed-speed wind generator of the same capacity. The system is capable of supplying active and reactive power to the grid without the addition of external devices. Since the converter power losses are relatively small the overall efficiency of the system is improved. This makes the DFIG the most preferred WECS choice in the market [15].

Although this type of configuration is viable in terms of speed variation, when directly coupled to the grid its performance deteriorates under low power quality grid voltage, and this might result to infringement of grid code if not appropriately controlled [21] - [22].

2.4 The BTB Converter

In order to facilitate the super-synchronous and sub-synchronous generating modes, a back-to-back converter is connected between the rotor circuit. The DFIG is shown in Figure 2.5. According to the steady-state analysis, bidirectional power flow in the rotor circuit is key to achieving generation both in sub-synchronous and super-synchronous speeds.

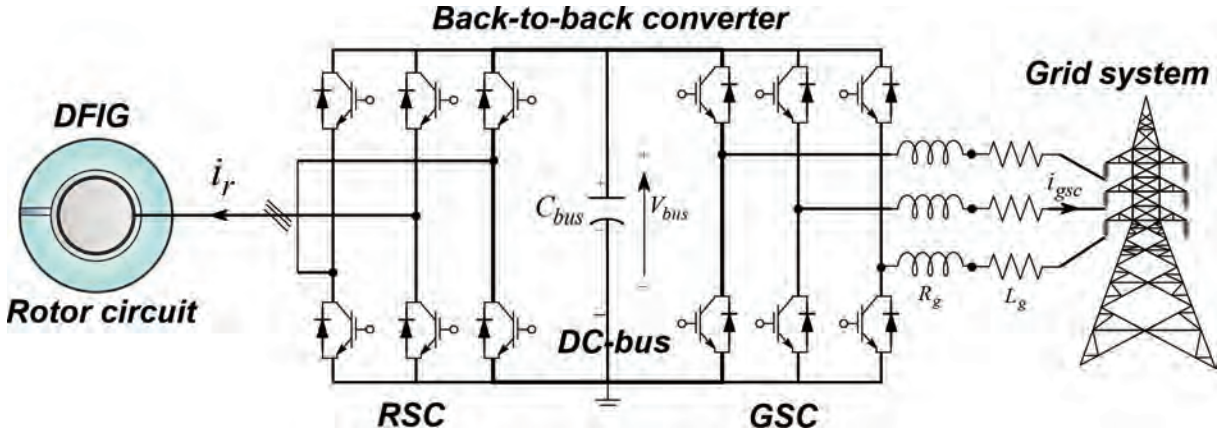


Figure 2.5 Model of a full-switched back-to-back converter

The pulse width modulation (PWM) switching strategy is commonly employed in the control of voltage source converters due to its simplicity and effectiveness. By comparing the reference signal with a triangular waveform, the switching commands can be obtained and applied to the converter in order to generate the desired output voltage. The output voltage that can be generated is given by [9]:

$$S_j = \begin{cases} 1 & \text{if } v_j^* > v_{tri} \\ 0 & \text{if } v_j^* \leq v_{tri} \end{cases} \quad (2.1)$$

-
- j - denotes three-phase quantities a, b, c
 v_a^*, v_b^*, v_c^* - three-phase reference voltages
 v_{tri} - triangular signal

2.5 Control Techniques Overview

The rotor side converter (RSC) control system is responsible for the control of active and reactive power flow of the stator while the grid-side converter controls the reactive power and maintains the DC bus voltage [9]. These are controlled in the outer control loops of the DFIG controllers. The effectiveness of the control system is improved by controlling the currents of both the rotor side and the grid side, and this introduces another control loop known as the inner current loop or level I current control strategy [2].

2.5.1 Vector Control

The vector control technique is mostly encountered in digital control of electrical machines and drives as it can be easily understood and implemented. In the control of DFIGs, with the aid of a dq reference frame transformation, the stator voltage oriented control SVOC, and stator flux oriented control SFOC methods can be used. The multi-loop system which consists of many PI controller results in a low dynamic response which is a drawback in the case of voltage dips [15]-[13].

2.5.2 Direct Torque Control (DTC)

The direct torque control is also a vector-based control method, and it is based on space vector modulation of possible RSC output voltages. Here two variables of DFIG are directly controlled, namely: torque and rotor flux amplitude. The electromagnetic torque equation is

$$T_{em} = \frac{3}{2} p \frac{L_m}{\sigma L_s L_r} |\bar{\psi}_r| \cdot |\bar{\psi}_s| \sin \delta \quad (2.2)$$

where δ is the angle between the stator and rotor flux.

It can be noted for Equation 2.2 than the electromagnetic torque depends on the magnitudes of stator and rotor flux and the angle between their space vectors [9].

Since the DFIG is directly connected to the grid, it can be deduced that the constant stator voltage produces a stator flux of constant amplitude and speed. Therefore a desirable value of electromagnetic torque is achievable by controlling the rotor flux amplitude and position. This means the machine can be controlled by matching the rotor flux speed with the stator flux speed [9].

Some of the benefits of DTC are the fast dynamic response, reduced tuning efforts of PI controllers and excellent perturbation rejection. The main drawback of this method is non-constant switching of controlled switches which can result in nonuniform semiconductor losses [9].

2.5.3 Model Predictive Control (MPC)

The vector control techniques discussed in the previous sections are passive; they only react to events when they occur rather than before the occurrence. The finite control set for MPC (FCS-MPC) is studied in depth in [2]. It is a proactive method in the sense that it can predict future

events and take control actions based on function minimization. It offers an excellent dynamic performance in all three frames of reference (abc , $\alpha\beta$ and dq) [2].

2.6 Voltage Dips

A voltage dip can be described as a short-duration drop of voltage in one or more phases. In the case where all phase voltages are reduced uniformly, such voltage dips are classified as balanced or symmetrical. Whereas unbalanced voltage dips are referred to as asymmetrical. The voltage dips are usually attributed from short-duration over-currents, transformer energizing, inrush currents due to motor group start-ups or three-phase to ground short-circuits [12], [3], [9].

2.6.1 Severity of Voltage Dips

Voltage dips can be mainly categorised according to their severity, namely, small (non-severe) and severe voltage dips. In [9] voltage dips are further classified as partial and total voltage dips. During a partial voltage dip the rotor is regarded as being open-circuited, here the voltage level falls below the rated value but above zero. In a total voltage dip, the voltage falls by 100 % of its rated value [9].

A severe voltage dip induces emfs that exceed the maximum voltage of the rotor converter, as a result the reference frame is affected and the saturation of the converter occurs, hence the control of rotor current is lost. Whereas a voltage dip can be small or moderate such that it does not result in saturation. Although there is no saturation the presence of natural and negative fluxes,

they will still cause some oscillations in currents and electromagnetic torque, but the converter can independently control rotor current [9], [12].

The general operation of the DFIG machine under small voltage dips can be viewed as superimposed behaviours of positive, negative (in the case of asymmetrical voltage dip) and natural machines.

- In the positive sequence machine the stator voltage equates to the positive sequence component of the grid voltage.
- The natural machine represents a machine with a zero stator voltage but magnetized due to the presence of natural flux.
- In the case of asymmetrical voltage dip the contribution of the negative sequence component of the stator voltage is separately represented by the negative machine.

2.6.2 Symmetrical Voltage Dips

Symmetrical voltage dips usually result in balanced voltage dips at the terminals of a DFIG. It can be deduced from the study of symmetrical components that the negative and zero sequence components are not present during a balanced voltage dip [23]. Therefore the control during the symmetrical voltage dip can only focus on the decay of the natural flux.

Saturation of the RSC during a voltage dip occurs when the RSC reaches its maximum output voltage and this can result in the loss of rotor current control. The maximum output voltage of the

RSC $V_{r,max}$ can be obtained using:

$$V_{r,max} = \frac{V_{bus}}{\sqrt{3}} D_{max} \quad (2.3)$$

where V_{bus} is the DC bus voltage and D_{max} is the maximum duty cycle (around 97 % and 99 %).

When a sudden voltage drop occurs at $t = 0$ the voltage space vector \vec{v}_s is promptly reduced to its steady-state value. However, by conservation of flux principle, the stator flux $\vec{\psi}_s$ cannot decay as rapidly as the stator voltage; hence, it is sustained in the stator windings. Each phase of the stator flux is a function of a sinusoidal component (permanent flux or stator-forced flux) ψ_{sf} and the exponential DC component (natural flux) ψ_{sn} which produced by the voltage dip occurrence and decays with the time constant L_s/R_s . It can be seen from

$$\frac{d\vec{\psi}_s}{dt} = \vec{v}_{s,fault} - \frac{R_s}{L_s} \vec{\psi}_s + R_s \frac{L_m}{L_s} \vec{i}_r \quad (2.4)$$

that the rotor current term can be utilized to force the rapid decay of stator flux. The RSC can easily control the rotor current if the control has not been lost due to the fault [9] [13].

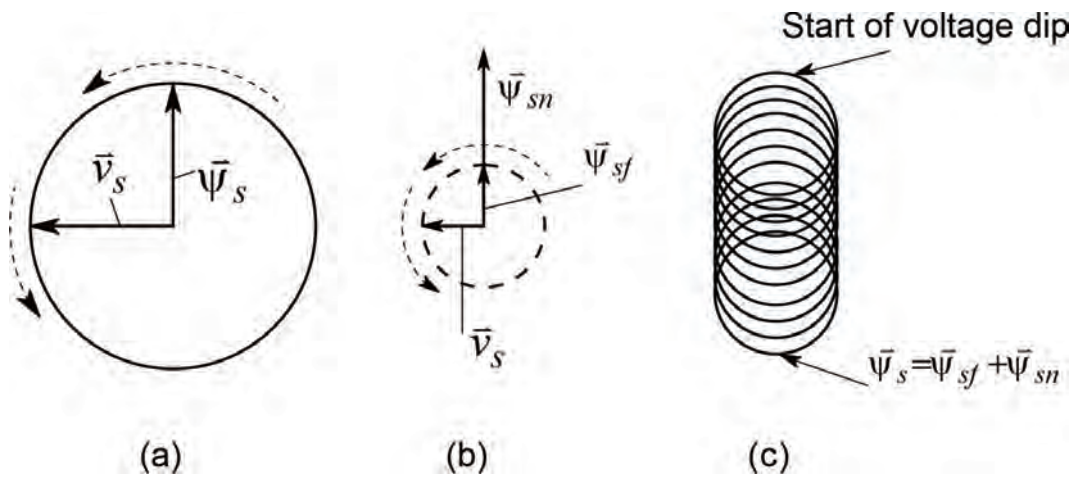


Figure 2.6 DFIG flux trajectory under symmetrical voltage dips [12]

Under symmetrical voltage dips, the superposition principle allows of dual representation of the DFIG dynamic model, namely, the natural machine and the forced machine, and additionally the negative machine as shown in Figure D.3. The forced machine is equivalent to the normal DFIG dynamic model. The stator natural flux $\vec{\psi}_{sn}$ as a function of rotor natural current \vec{i}_{rn} can be expressed as:

$$\frac{d\vec{\psi}_{sn}}{dt} = -\frac{R_s}{L_s}\vec{\psi}_{sn} + R_s\frac{L_m}{L_s}\vec{i}_{rn} \quad (2.5)$$

2.6.3 Impact of Asymmetrical Voltage Dip

An asymmetrical voltage dip occurs when the three phases undergo an unbalanced fall of voltage. This may be due to phase-to-phase faults in the power system, quick unbalanced three-phase loading of the networks due to group start of single-phase motors, or open circuit faults in large three-phase motors which results to single-phasing. In practice, asymmetrical faults are encountered more frequently than symmetrical faults [9].

The asymmetrical faults are encountered, for instance, in weak grids where nonlinear loads present unbalance grid voltage. This fault also happens for some periods where grid faults present unbalanced voltage as seen by the DFIG. In all cases, unbalanced voltage degrades the performance of the DFIG through torque oscillations and unbalanced exchange of stator currents [3]. The effect of the 40% asymmetrical voltage dip can be observed from Figure 2.8 in Chapter 4. The grid voltage unbalances are commonly caused by:

- Malfunction of the power factor compensation equipment.
- Unevenly distributed single-phase loads operating on the same power system.

-
- Unidentified single-line to ground fault.
 - An open circuit on some part of the distribution system.

An unbalanced grid will trigger the negative-sequence components in the grid voltage. Because the negative-sequence impedance of the DFIG is very low, even a small magnitude of negative-sequence voltage can result in a fairly large negative-sequence current. Consequently, this will cause fluctuations in the machine's electromagnetic torque and DC-bus voltage of the power electronic converter. This presents the following negative impacts [12] [9]:

1. Large negative-sequence current will reduce efficiency due to the increase in winding loss.
2. The second-order fluctuation of the DFIG electromagnetic torque will present fatigue in mechanical components of the wind turbine.
3. Large second-order harmonic current flowing through the DC-bus capacitor will reduce its lifetime.
4. Harmonic distortion of the RSC output current due to the second-order harmonic component in the DC-bus voltage.

The problem of unbalanced grid voltage can be addressed through the study of symmetrical components where it can be divided into positive-sequence, negative-sequence and zero-sequence components. The stator flux behaviour during an asymmetrical voltage dip can be derived by considering the sequence component decomposition, i.e.:

$$\vec{v}_{s,fault} = \vec{v}_s^+ + \vec{v}_s^- \quad (2.6)$$

and neglecting the contribution of the rotor current [12] so that

$$\vec{\psi}_s(t) = \vec{\psi}_{sn}(0)e^{-(R_s/L_s)t} + \frac{\vec{v}_s^+}{j\omega_s}e^{j\omega_s t} - \frac{\vec{v}_s^-}{j\omega_s}e^{-j\omega_s t} \quad (2.7)$$

The problems associated with unbalanced grid voltage can be overcome by introducing a precise amount of negative sequence into the rotor references. It is imperative to control each sequence independently in order to guarantee that both sequences are well regulated. This control philosophy is named the dual-vector control technique; this technique for unbalanced grid voltage control is widely covered in the literature [3].

2.6.4 Summary

Small voltage dips do not cause converter saturation while severe voltage dips do cause converter saturation. Since the stator is directly connected to the grid, the frequency of the stator, once synchronized, remains locked with the frequency of the grid [15]. On the other hand, the direct connection of the stator to the grid results in poor control during and after grid faults [24].

2.7 Software Solutions

2.7.1 Demagnetizing Current Injection

The impact of the stator natural flux ψ_{sn} has been discussed. In order to enhance a quick decay of this flux component, a corresponding demagnetizing current \vec{i}_{rn} can be injected into the normal

current references [25],[24], this is

$$\vec{i}_{rn} = -\frac{L_m}{L_s L_r'} k_d \vec{\Psi}_{sn} \quad (2.8)$$

where k_d is a demagnetizing constant responsible for natural flux clearance time (demagnetization time). The larger the k_d the faster the natural flux clearance time; however, it was argued in the literature that faster natural flux clearance translates into larger oscillations in electromagnetic torque and reactive power [25], [26].

It was proposed in the literature [26] that the demagnetizing coefficient K_d required to cancel the rotor voltage can be calculated from

$$K_d = \frac{L_m}{L_s} \frac{1}{\sigma L_r'} \quad (2.9)$$

where $\sigma = 1 - L_m^2 / (L_s L_r')$

2.7.2 Dual Control of Rotor Currents

During a non-severe voltage dip where the rotor currents are still controllable, the current references of inner control loops can be calculated to meet specific control targets. In an asymmetrical voltage dip, the negative sequence control loop is added to the inner control loop in order to cancel the effect of unbalance grid voltage [24].

2.8 Consideration of Unbalanced Grid

In an unbalanced three-phase system, the variables can be decomposed to symmetrical components. In an induction generator with a wye winding connection and internal neutral point the zero sequence components of the grid voltage does not influence current, and it is therefore neglected, this leaves only the positive and negative sequence components [23].

2.8.1 Decomposition of the Reference Frame

When the effect of asymmetrical voltage dip is considered the dq axis can be split into positive (dq^+) and negative (dq^-) axis as shown in Figure 2.7. The negative dq axis rotates at the grid frequency but in the opposite direction resulting in the relative frequency which is twice the grid frequency [27]. The stator voltage in dq axis can be decomposed into positive and negative sequence components as expressed by [12]:

$$v_{dqs} = v_{dqs}^+ + v_{dqs}^- e^{-j2\omega_s t} \quad (2.10)$$

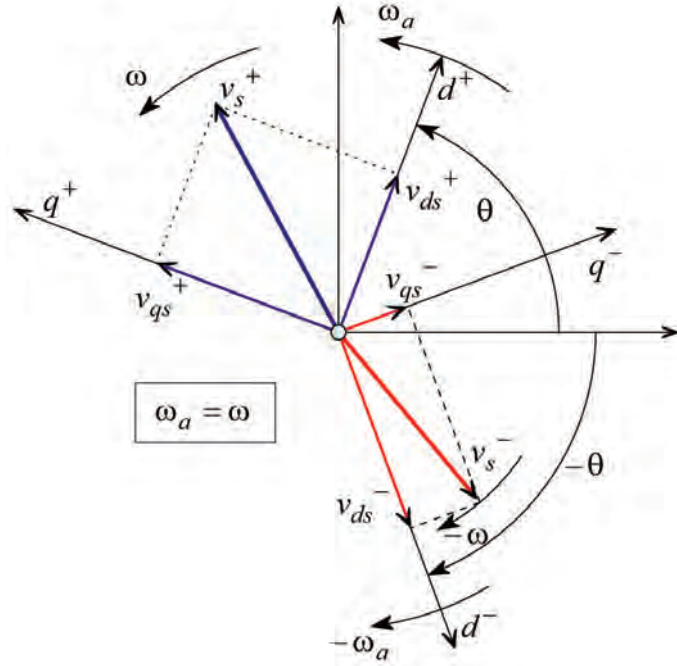


Figure 2.7 Sequence decomposition of the synchronous reference frame [12]

The derivation of the stator and rotor current under influence of grid voltage dip is studied in depth in the book [12]. The decomposed forms of i_{dqs} and i_{dqr} are:

$$i_{dqs} = i_{dqs}^+ + \frac{v_{dq_s}^-}{X_{vis}(-j\omega_s)} e^{-j2\omega_s t} \quad (2.11)$$

$$i_{dqr} = i_{dqr}^+ + \frac{L_m}{L_s} \frac{v_{dq_s}^-}{X_{vir}(-j\omega_s)} e^{-j2\omega_s t} \quad (2.12)$$

where $X_{vis}(-j\omega_s) = -j\omega_s \sigma L_s$ is the negative sequence impedance of the grid voltage to the stator current, and $X_{vir}(-j\omega_s) = -j\omega_s \sigma L_r$ is the negative sequence impedance of the grid voltage to the rotor current [12]. The effects of a 40% asymmetrical voltage dip on the stator and rotor currents were simulated using MATLAB/Simulink and can be observed in Figure 2.8.

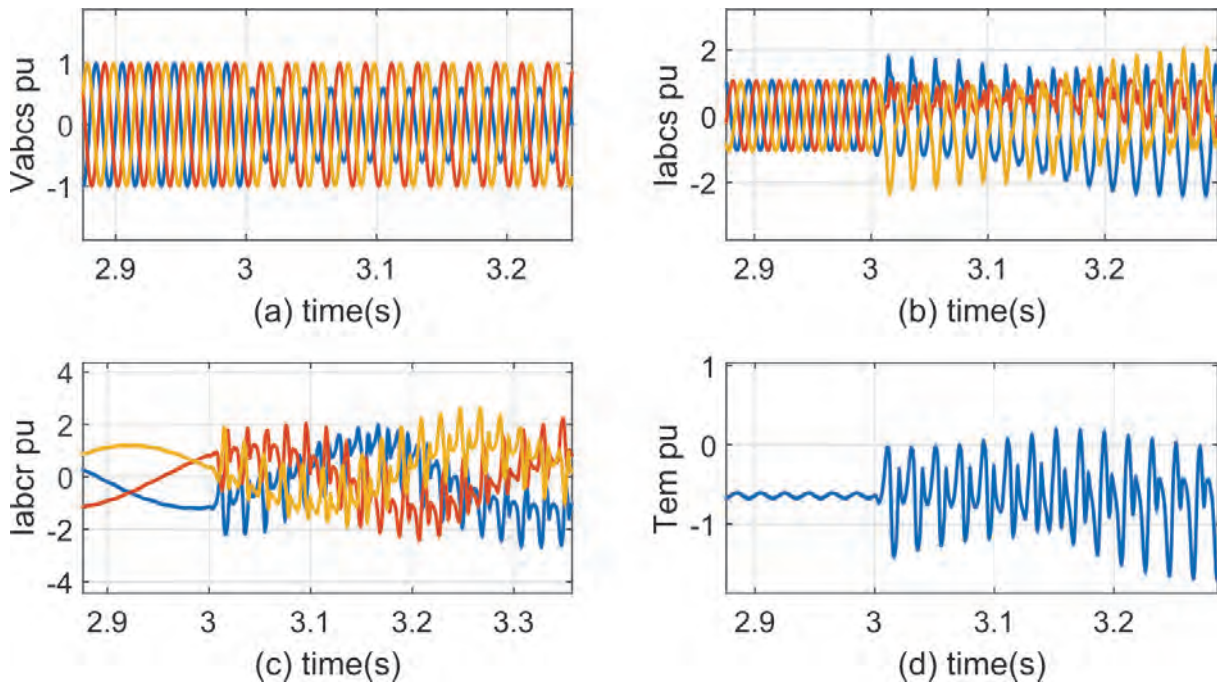


Figure 2.8 Effect of asymmetrical grid voltage on stator and rotor current and electromagnetic torque

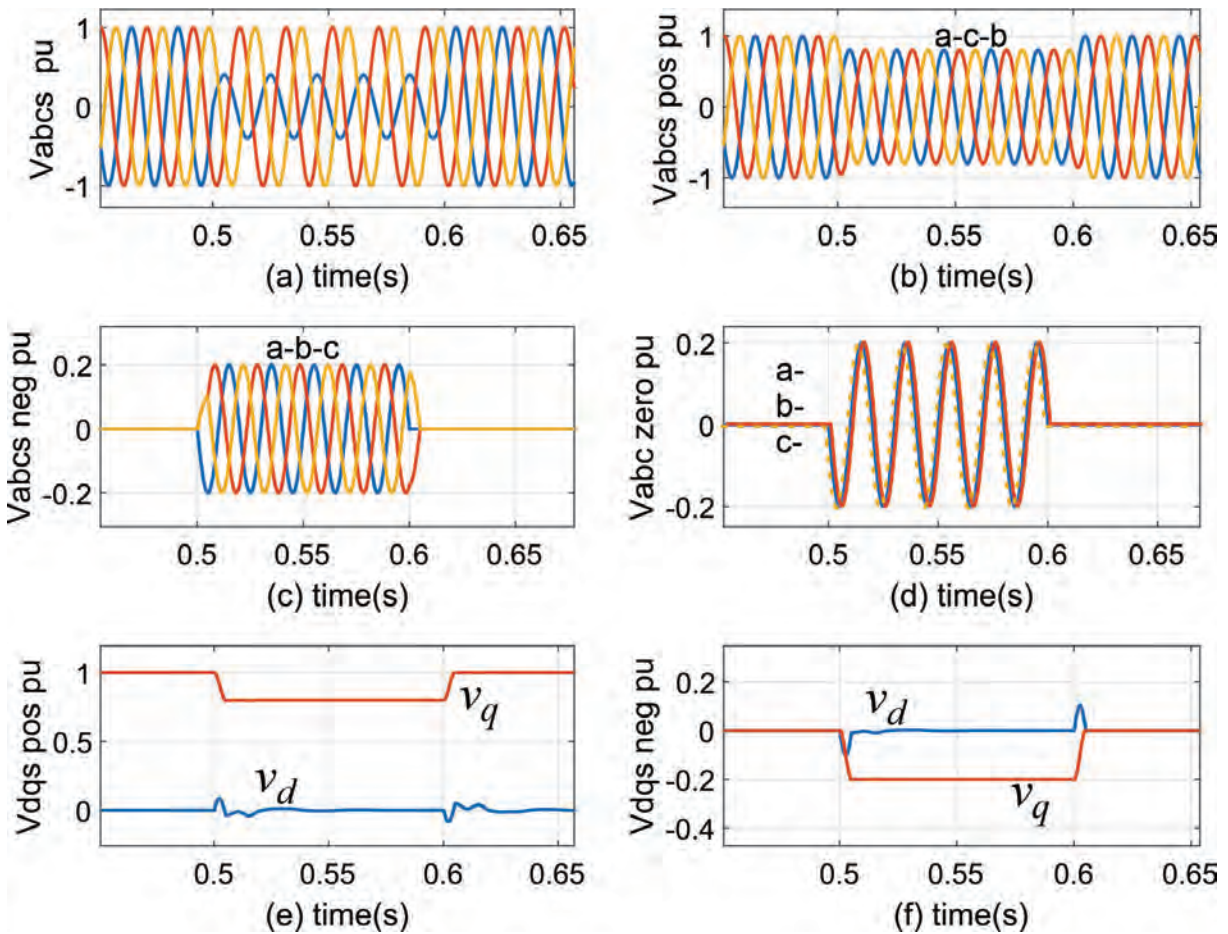


Figure 2.9 Sequence composition during 60% single-phase asymmetrical voltage dip (a) Three-phase total grid voltage (b) Positive sequence voltage (c) Negative sequence voltage (d) Zero sequence voltage (e) Positive sequence in dq reference frame (f) Negative sequence in dq reference frame

2.8.2 Symmetrical Components

In the previous section the DFIG variables are derived by introducing the negative sequence reference frame. A 60 % asymmetrical dip is shown in Figure 2.9 and this gives the positive, negative and zero sequence voltages. It has been discussed that the asymmetrical three-phase variables can be decomposed to balanced, symmetrical components, which are the positive, negative and zero

sequences [23]. The transformation for this is

$$\begin{bmatrix} f^p \\ f^n \\ f_0 \end{bmatrix} = \frac{1}{3} \begin{bmatrix} 1 & a & a^2 \\ 1 & a^2 & a \\ 1 & 1 & 1 \end{bmatrix} \begin{bmatrix} f_a \\ f_b \\ f_c \end{bmatrix} \quad (2.13)$$

where f denotes any three-phase variables and $a = e^{j2\pi/3}$. Subscripts p,n,0 denote positive, negative, and zero sequences, respectively. The phasor representations of the positive, negative and zero order phasors are shown in Figure 2.10. This is studied in depth in the literature [28]. In the induction machine, the stator windings are wye connected with an internal neutral point the zero sequence currents are not present. Therefore from this principle voltages and currents can be expressed as the phasor sum of positive sequence and negative sequence components in dq reference frame. That is:

$$\begin{aligned} \bar{v} &= (v_{d1} + v_{d2}) + j(v_{q1} + v_{q2}) \\ \bar{i} &= (i_{d1} + i_{d2}) + j(i_{q1} + i_{q2}) \end{aligned} \quad (2.14)$$

where subscripts 1 and 2 denote positive and negative sequences respectively.

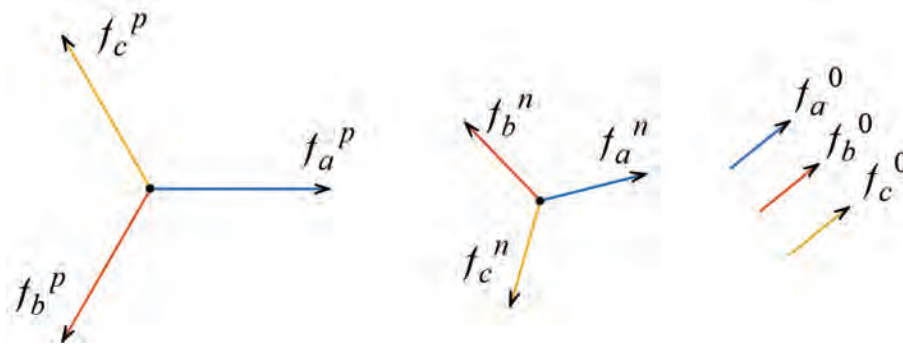


Figure 2.10 Sequence decomposition of unbalanced three-phase system

2.8.3 Signal Delay Cancellation Method

The delay cancellation method proposed in the literature [22] is used to find the positive and negative sequence components of grid voltage in $\alpha\beta$ -axis . Here an abc signal is first transformed into $\alpha\beta$ reference by Clark's transform and delayed for $T/4$, at 50 Hz this is equivalent to $\omega t = 90^\circ$. The sequence decomposition is then realized through taking the linkage matrix of the real-time signals and the delayed signals as given by

$$\begin{bmatrix} v_{\alpha}^{+}(t) \\ v_{\beta}^{+}(t) \\ v_{\alpha}^{-}(t) \\ v_{\beta}^{-}(t) \end{bmatrix} = \frac{1}{2} \begin{bmatrix} 1 & 0 & 0 & -1 \\ 0 & 1 & 1 & 0 \\ 1 & 0 & 0 & 1 \\ 0 & 1 & -1 & 0 \end{bmatrix} \begin{bmatrix} v_{\alpha}(t) \\ v_{\beta}(t) \\ v_{\alpha}(t - T/4) \\ v_{\beta}(t - T/4) \end{bmatrix} \quad (2.15)$$

These signals are further transformed to dq reference frame as shown in the implementation block diagram in Figure 2.11.

An asymmetrical voltage dip was applied by dropping the voltage of phase by 30% between $t = 0.05$ s and $t = 0.15$ s. It can be observed from Figure 2.12 that when the fault occurs, there is a sudden rise in the negative sequence component of the voltage on the q-axis while the d-axis voltage remains unchanged. It can be noted that the signal delay has a negligible effect on the dq variables since it occurs for a quarter of a cycle at the start of the simulation.

The signal cancellation can be implemented as shown in Figure 2.11; where M_{ag} is the orthogonal matrix in Equation 2.15.

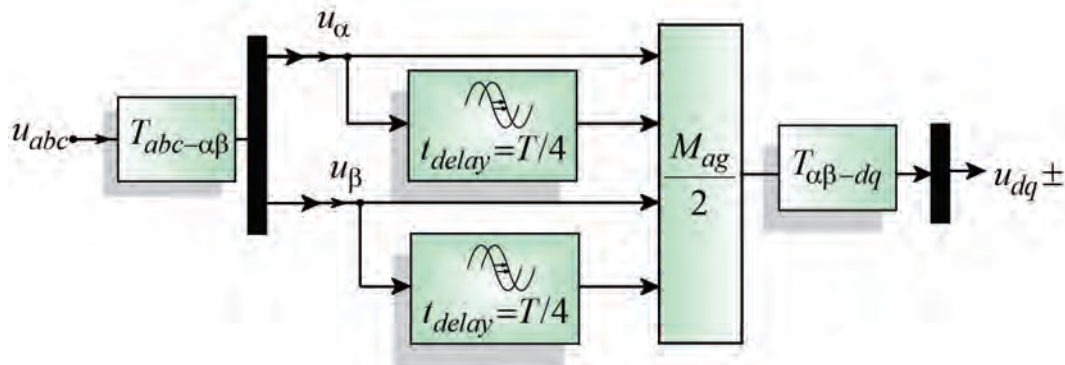


Figure 2.11 Signal delay cancellation block diagram [22]

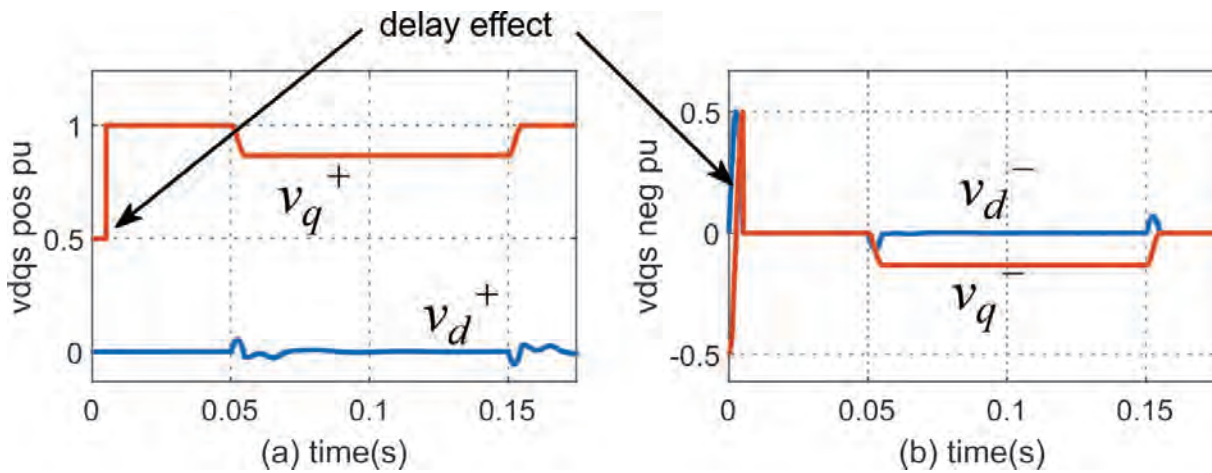


Figure 2.12 Signal delay cancellation method in dq reference frame (a) Positive sequence voltage (b) Negative sequence voltage[22]

2.9 Hardware Solutions

During small voltage dips, software-based fault ride-through strategies can effectively reduce the transients of some targeted parameters. However, under severe voltage dip, this is not possible due to the saturation of the power electronic converter. In this case, hardware solutions of FRT are necessary [9].

2.9.1 Crowbar Protection

Crowbar protection is commonly used as a DFIG protection system to ride-through transients at severe voltage dips. A crowbar system consists of a shunt resistor that is connected at the terminals of the rotor circuit through a DC rectifier. A switch operates the system, such that when the fault occurs the crowbar is activated while the RSC is deactivated (open-circuited), therefore all the transient current can be taken by the crowbar, in that way sparing the BTB converter, [12] to [24].

The crowbar protection system can be easily activated and deactivated by fault discrimination based on the magnitudes of rotor current (I_r), dc-link voltage (V_{dc}) or rotor voltage (V_r). When one of the magnitudes is greater than the threshold, the crowbar protection scheme is enabled. In order to avoid frequent triggering and re-triggering of the crowbar, some hysteresis can be added to the switching time of the relaying system, [12] to [24].

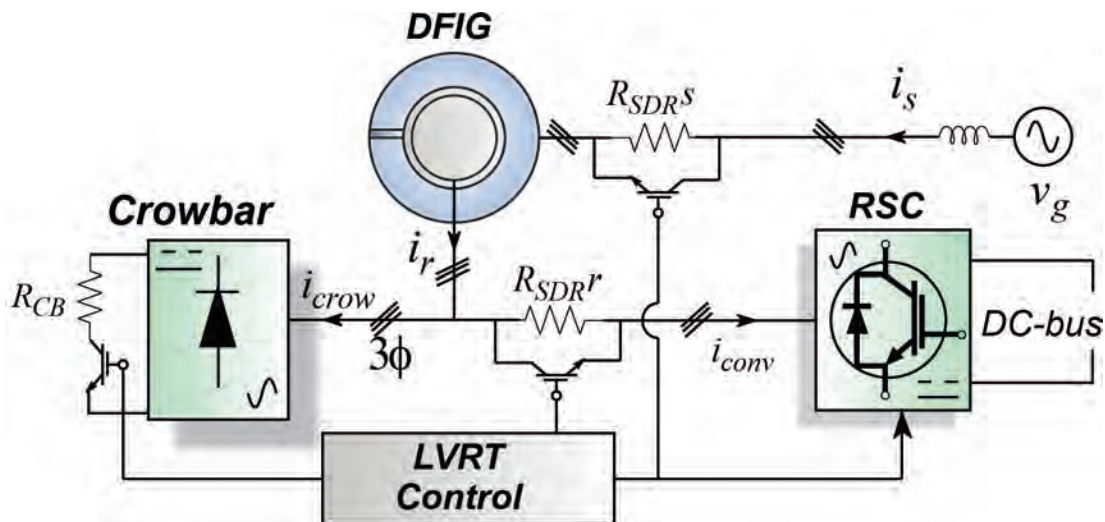


Figure 2.13 Low voltage ride-through protection system, comprising of an SDR and crowbar protection scheme

2.9.2 Series Dynamic Resistor

The other method of limiting transient currents is to connect a three-phase resistor in series with the rotor terminals or with the stator terminals. Unlike in the crowbar protection scheme, with the increase in rotor or stator resistance this method can limit transient currents and dump natural flux while at the same time allowing the RSC control of reactive power as demanded by the grid connection code. Furthermore, the voltage drop across the SDR reduces the RSC output voltage demand [24], which is advantageous.

Crowbar resistance and activation time are sensitive aspects in the crowbar protection. Choosing a very low value of a crowbar resistance might result in very high currents in the crowbar circuit, demanding an oversized crowbar switch. On the other hand, a very high resistance will slow down the evolution of natural flux, sustaining the voltage dip-induced emf in the rotor circuit [9], [24]. Consequently, the combined resistance of series dynamic resistor (SDR) and the rotor side and crowbar shall not exceed the critical resistance. This resistance is derived by considering the worst case scenario of 1 pu symmetrical voltage. It can be calculated using

$$\tau_r = \frac{\sigma L_r}{R_r + R_{protection}} \quad (2.16)$$

as proposed by J. Yang *et al* [29].

2.9.3 Reliability of the Mitigation Strategies

With active crowbar protection, the rotor circuit is short-circuited with a low resistance while the RSC is disabled. Therefore the transient over-currents flow through the crowbar, hence offering protection to the RSC [9]. However, while an active crowbar is enabled the DFIG behaves like a

squirrel cage induction machine and the RSC cannot control reactive power. As a result, the grid delivers reactive power to the DFIG. This is an infringement of the grid code [14],[24].

The control of demagnetizing current reduces stator flux transients during the sudden change of grid voltage, and it is good in terms of transient response. On the other hand, the injection of demagnetizing current can result in large electromagnetic torque transient oscillations. However, they last for a very short period of time. Torque oscillations are not good in the electrical operation of a machine as they translate to mechanical torsional stresses to the wind turbine [9], [30].

Dual vector control techniques enhance the behaviour during unbalanced grid voltage. It is possible to achieve balanced stator and rotor currents. Typical software strategies only depend on the availability of the RSC to control rotor currents; in the case of saturation, the safety and LVRT capability is compromised. Consequently, they cannot be trusted in terms of the safety of the whole wind farm. In that way, some other hardware techniques are required to dump the negative and natural fluxes.

2.10 Power Capability of DFIG

2.10.1 Modes of operation

The induction machine produces power when its rotor is turned faster than synchronous speed, below synchronous speed the machine operates in a motoring mode, hence it instead appears as a load to the power system network to which it is connected [31]. However, this scenario is not true for a DFIG. Below synchronous speed, power can be injected into the rotor via the converter,

which is amplified across the airgap, so that the power coming out of the stator is greater than the rotor input power. This requires a generating torque. In the wind energy conversion system, the main shaft or prime mover is not guaranteed to turn at or above synchronous speed due to the variable nature of wind and a DFIG can cope with this. Grid-connected DFIGs seek to maintain a steady power flow from the stator to the network whatever the speed is[32].

For the entire operation of a DFIG the stator output power P_s flows from the generator to the grid while rotor active power P_r changes direction according to the mode of operation. Figure 2.14 gives the illustration of this power exchange. In sub-synchronous mode, when the mechanical speed of the rotor is below the synchronous speed, and the slip is positive, the rotor windings absorb the active power from the grid, and hence the direction of power flow is from the grid to the DFIG. Above the synchronous speed, in super-synchronous mode, when the slip is negative, both the stator and rotor windings deliver power to the grid. This can be deduced from [2] [15]:

$$|P_s| = \begin{cases} |P_m| + |P_r| & \text{for Sub-synchronous} \\ |P_m| - |P_r| & \text{for Super-synchronous} \end{cases} \quad (2.17)$$

The change in the phase relationship of the three-phase rotor current during the subsynchronous to super-synchronous transition in Figure 2.15 supports this theory. It can be observed that at sub-synchronous mode the phase relationship of rotor current is $i_{ar} - i_{br} - i_{cr}$, but in super synchronous mode it reverses to $i_{ar} - i_{cr} - i_{br}$. When approaching the synchronous speed that all three-phase currents tend to be of DC nature [15].

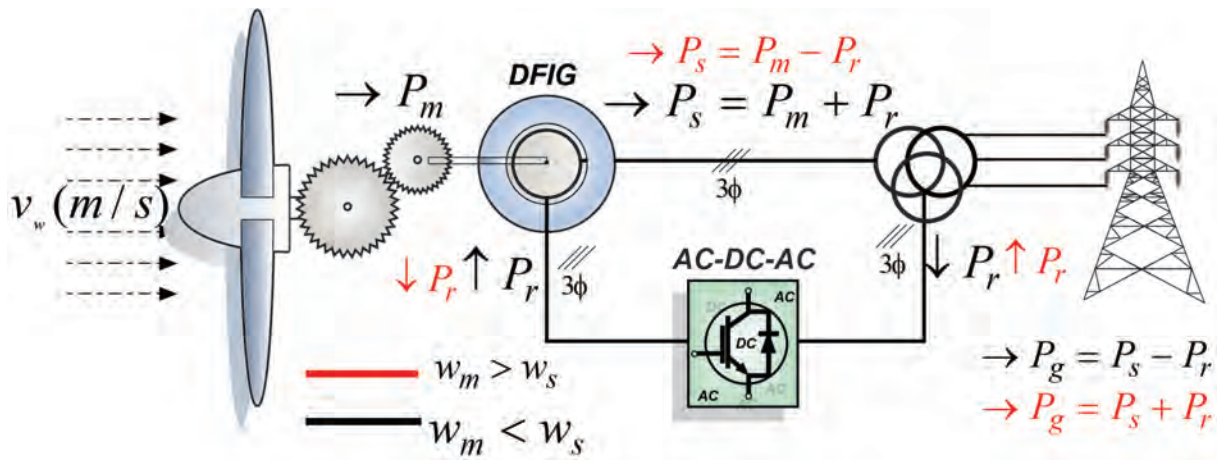


Figure 2.14 Power flow in DFIG wind energy conversion system, (a)Sub-synchronous mode of operation, (b)Super-synchronous mode of operation

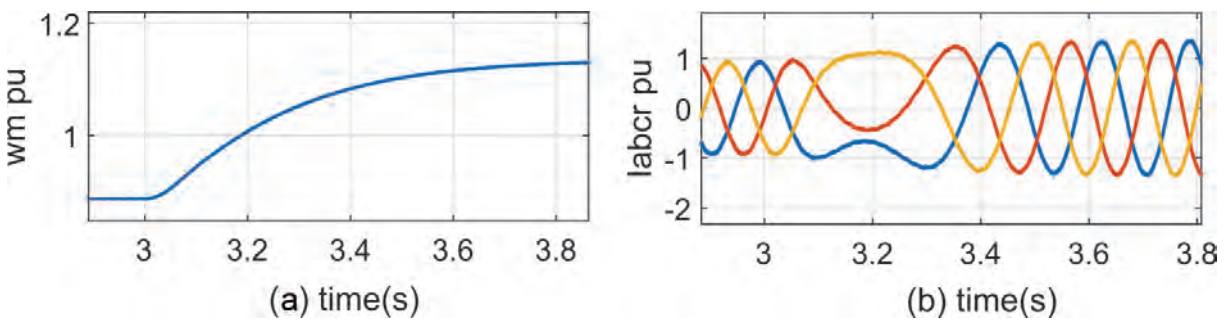


Figure 2.15 The transition between subsynchronous and supersynchronous modes of operation

2.10.2 Limitations of Deliverable Power

Any electrical machine should operate within its nameplate ratings since exceeding these nominal values can result in overheating of cables and reduce efficiency due to saturation and increased I^2R losses in the windings. With the modern electrical protection technology, any machine operating above the limits can be quickly and precisely isolated from the network. Therefore the consideration of the machine power capability when designing its control system is important.

2.11 Steady State Operation of DFIG

2.11.1 Equivalent Circuit

The steady-state equivalent circuit shown in Figure 2.16 represents one phase of the stator and rotor windings. The model assumes linear magnetization and structural symmetry, and therefore the other two remaining phases are similarly modelled. For a grid-connected DFIG, the stator is directly connected to the grid while the grid supplies the rotor voltage through a back-to-back electronic converter. In order to simplify the analysis, the circuit is modified to the 'stator reduced' equivalent circuit as shown in Figure 2.17 by referring all rotor quantities to the stator [3]. This is the general circuit for the DFIG; for an induction motor, the rotor is shorted so that $\bar{V}_r' = 0$. From this we obtain the equations

$$\begin{aligned}\bar{V}_s &= \bar{E}_s + (R_s + j\omega_s L_{ls})\bar{I}_s \\ \bar{V}_r' &= \bar{E}_r' + (R_r' + j\omega_{sl} L_{lr}')\bar{I}_r'\end{aligned}\quad (2.18)$$

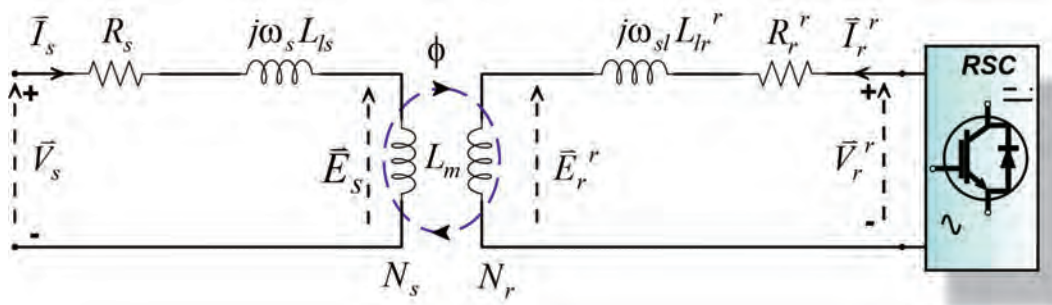


Figure 2.16 Steady-state equivalent circuit of the DFIG. [12]

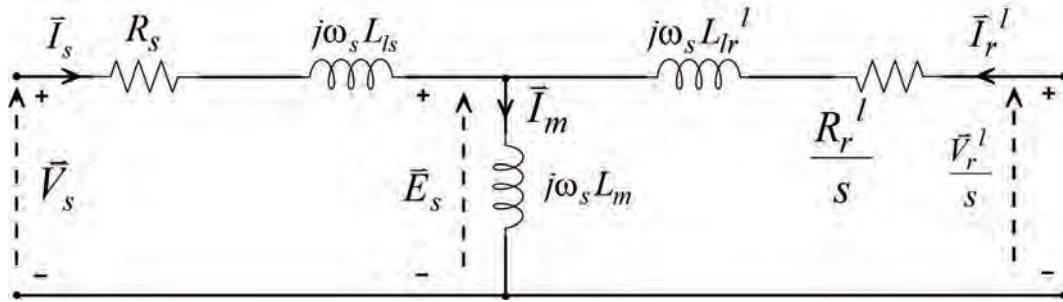


Figure 2.17 Stator referred per-phase steady-state equivalent circuit of a DFIG.

The DFIG is directly connected to the grid; therefore, the stator angular frequency is $\omega_s = 2\pi f_s$ where f_s is the synchronous grid frequency. Furthermore, the induced EMF in the rotor circuit depends on the slip angular frequency ($\omega_{sl} = \omega_s - \omega_m$), where ω_m is the electrical rotational angular frequency of the rotor. The conversion between mechanical and electrical speeds is expressed in Equation 3.1 in the next chapter [12].

For simplicity it is necessary to refer all rotor variables to the stator, this can be done by using the applying the principle of mutual flux ϕ as presented in Figure 2.16. The induced EMF on the stator windings can be calculated from

$$\bar{E}_s = j\omega_s k_s N_s \phi \quad (2.19)$$

where N_s is the number of turns of the stator winding per phase, k_s is the stator winding factor. The

induced EMF on the rotor windings can be calculated in a similar way:

$$\bar{E}_r^l = j\omega_{sl} k_r N_r \phi \quad (2.20)$$

where N_r is the number of turns of the rotor winding per phase, k_r is the rotor winding factor. Now

by approximating k_s/k_r to be equal to 1, the relationship between E_s and E_r^l can be derived from

Equations 2.19 and 2.20 so that

$$\frac{\bar{E}_r}{\bar{E}_s} = \frac{j\omega_{sl}k_r N_r}{j\omega_s k_s N_s} \approx \frac{s}{n_{sr}} \quad (2.21)$$

where $s = \omega_{sl}/\omega_s$ is the slip ratio, n_{sr} is the stator to rotor turns ratio. By applying the transformer action principle, the variables of the rotor side can be easily be referred to the stator side. Therefore rotor voltage equation can be rewritten by substituting Equation 2.21 into Equation 2.18, which gives

$$\frac{n_{sr}}{s}\bar{V}_r^r = \bar{E}_s + \left(\frac{n_{sr}^2}{s}R_r^r + j\omega_s n_{sr}^2 L_{lr}^r \right) \frac{\bar{I}_r^r}{n_{sr}} \quad (2.22)$$

In order to reduce the complexity of the equations, the variables of Equation 2.22 can be redefined:

$$\begin{aligned} \bar{V}_r^l &= n_{sr}\bar{V}_r^r & \text{and} & & \bar{I}_r^l &= \frac{\bar{I}_r^r}{n_{sr}} \\ R_r^l &= n_{sr}^2 R_r^r & \text{and} & & L_{lr}^l &= n_{sr}^2 L_{lr}^r \end{aligned} \quad (2.23)$$

where subscripts r and l represent variables referred to the rotor and stator respectively, then by using Equation 2.23, Equation 2.18 is modified as shown in

$$\begin{aligned} \bar{V}_s &= \bar{E}_s + (R_s + j\omega_s L_{ls})\bar{I}_s \\ \frac{\bar{V}_r}{s} &= \bar{E}_s + \left(\frac{R_r}{s} + j\omega_s L_{lr} \right) \bar{I}_r \end{aligned} \quad (2.24)$$

Furthermore, the stator referred equivalent circuit is derived as shown in Figure 2.17. It is essential to note that the frequency of the stator side is ω_s , which is different from the frequency of the rotor side, which is the slip frequency ω_{sl} .

2.11.2 Steady-State Power Flow

The magnetizing current can be easily obtained by applying KCL on the equivalent circuit in Figure 2.17 and the flow of the magnetizing current I_m in the induction machine is due to the

stator-induced EMF \bar{E}_s :

$$\bar{I}_m = \bar{I}_s + \bar{I}_r \quad (2.25)$$

$$\bar{E}_s = j\omega_s L_m \bar{I}_m \quad (2.26)$$

The stator and rotor active and reactive powers can be expressed as:

$$\begin{aligned} P_s &= \text{Re}(\bar{V}_s \bar{I}_s^*) \quad \text{and} \quad Q_s = \text{Im}(\bar{V}_s \bar{I}_s^*) \\ P_r &= \text{Re}(\bar{V}_r \bar{I}_r^*) \quad \text{and} \quad Q_r = \text{Im}(\bar{V}_r \bar{I}_r^*) \end{aligned} \quad (2.27)$$

By using Equations 2.25, 2.26, 2.27 and 2.24 the relationship between the rotor and stator powers can be derived from:

$$\begin{aligned} P_r &= R_r I_r^2 + s R_s I_s^2 - s P_s \\ P_r &= P_{rcu} + s(P_{scu} - P_s) \end{aligned} \quad (2.28)$$

where P_{rcu} and P_{scu} are rotor and stator copper losses respectively. If it is assumed that the copper losses are much smaller than active powers P_s and P_r , Equation 2.28 reduces to:

$$P_r = -s P_s \quad (2.29)$$

Considering the fact that a DFIG operates at $\pm 30\%$ slip ratio range it can be shown using Equation 2.29 that the rotor active power flow P_r is limited to $\pm 30\%$ of the stator active power P_s . This supports the fact that the DFIG is a partial scale converter WECS.

From Figure D.1 it can be deduced that the input power to the is the sum of mechanical power and power from the RSC. Therefore if both the mechanical and electrical losses are ignored the power invariant equation can be derived:

$$P_m + P_r = P_{em} = -P_s \quad (2.30)$$

where P_m and P_{em} are the input mechanical power and developed electromagnetic power respectively. By combining Equations 2.29 and 2.30 and by considering that the total power to the grid is $P_g = P_s + P_r$, P_g can be expressed as a function of the stator power and slip ratio:

$$P_g = (1 - s)P_s \quad (2.31)$$

Table 2.1 Quadrants of GSC operation based on power factor [2]

| Quadrant | Power factor | Operation |
|----------|-------------------------------------|---------------------------|
| (I) | $0^\circ \leq \phi_g < 90^\circ$ | Inverter with lagging PF |
| (II) | $270^\circ \leq \phi_g < 360^\circ$ | Inverter with leading PF |
| (III) | $90^\circ \leq \phi_g < 180^\circ$ | Rectifier with lagging PF |
| (IV) | $180^\circ \leq \phi_g < 270^\circ$ | Rectifier with leading PF |

It can be deduced from the power relationships (2.29) to (2.31), that depend on the slip and sign of the power exchange, that the DFIG can operate in four possible quadrants of torque and speed as tabulated in Table 2.1 (where ϕ_g is the power factor angle). It is illustrated in Figure 2.14 that the GSC can operate both as a rectifier and an inverter. The power factor is a contributing factor to the direction of power flow in the GSC. The GSC can operate in four quadrants, as shown in Appendix D.1 [2].

2.11.3 Summary

The circuit of the induction machine can be reduced to stator-referred per phase equivalent circuit using the principle of an ideal transformer. According to the equations derived from the equivalent

circuit, the power flow in the rotor circuit is a fraction of the stator power and is proportional to the slip ratio.

From these equations it can be deduced that during the subsynchronous operation when the slip is positive, the stator delivers power to the grid while the rotor side absorbs power from the grid. At synchronous speed, the slip is zero. Hence the rotor is DC-excited; therefore, only the stator delivers power. In the super-synchronous mode, both the rotor and stator deliver power to the grid.

Chapter 3

Modelling

3.1 Dynamic Model

3.1.1 Voltage Equations

The simplified winding model induction machine is shown in Figure 3.1 from which the three-phase windings of both the stator and rotor are spatially displaced by 120° from one another, this also applies to the rotor. In this representation, multiple groups of coils are replaced with a single coil for each phase. The rotor is mechanically coupled to the main shaft of the wind turbine system which acts as a prime mover to the electrical system [15].

The rotor electrical variables rotate at a slip angular frequency ω_r relative to the stator variables and θ_r is the angular displacement between the stator MMF and rotor MMF. The slip angular frequency can be obtained by subtracting the mechanical rotational speed (in electrical rad/s) from

the synchronous frequency (in rad/s) of the grid ω_s [2], so that

$$\begin{aligned}\omega_r &= \omega_s - \omega_m \quad \text{and} \quad \omega_m = p\Omega_m \\ \theta_r &= \theta_s - \theta_m \quad \text{and} \quad \theta_m = p\theta_{rm}\end{aligned}\tag{3.1}$$

where ω_m and θ_m are the mechanical angular speed and position in electrical rads/s and electrical rads respectively. This is illustrated in Figure 3.1.

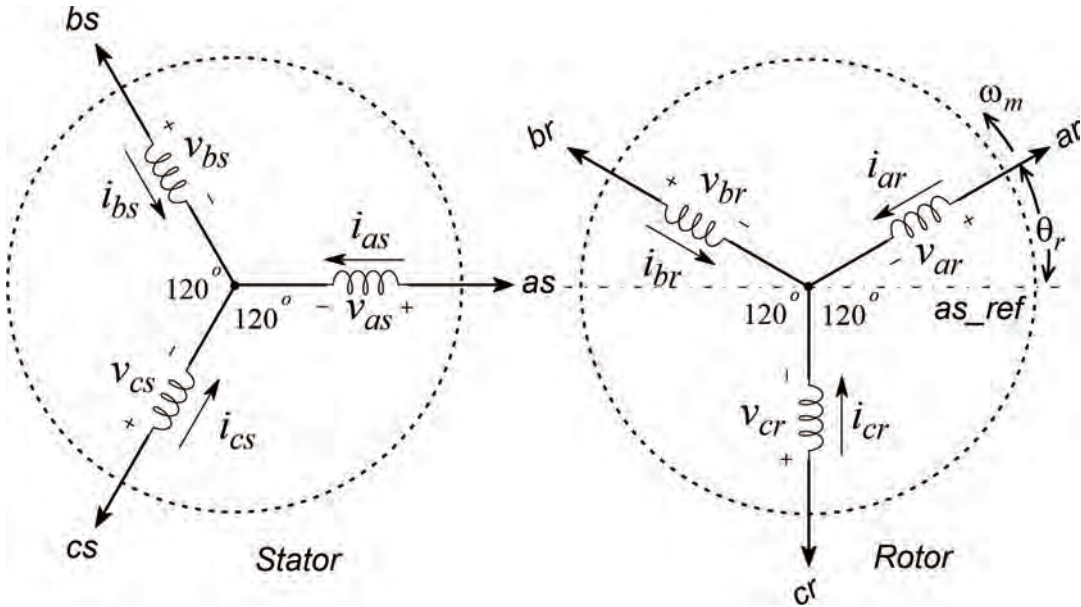


Figure 3.1 Idealized winding model of an induction machine

When developing the space vector model, the assumption is made that the generator is spatially symmetrical in structure, that the three-phases are balanced, and the magnetic core is linear with the core losses are negligible. The space vector is composed of three sets of equations the voltage equations, flux linkage equations and mechanical equations of motion. The voltage-flux relation in abc natural reference frame is then [15], [30]:

$$\begin{aligned}\vec{v}_s &= R_s \vec{i}_s + \rho \vec{\psi}_s + j\omega \vec{\psi}_s \\ \vec{v}_r &= R_r \vec{i}_r + \rho \vec{\psi}_r + j(\omega - \omega_r) \vec{\psi}_r\end{aligned}\tag{3.2}$$

where:

\vec{v}_s, \vec{v}_r - Three-phase stator and rotor voltages (V)

\vec{i}_s, \vec{i}_r - Three-phase stator and rotor currents (A)

$\vec{\psi}_s, \vec{\psi}_r$ - Stator and rotor flux (Wb)

R_s, R_r - Stator and rotor winding resistances (Ω)

ω - rotating speed of the arbitrary reference frame (rad/s)

ω_r - rotor electrical angular speed (rad/s)

ρ - derivative operator ($\rho = d/dt$)

On the right-hand side of Equation 3.2 the terms $j\omega\vec{\lambda}_s$ and $j(\omega - \omega_r)\vec{\lambda}_r$ are termed 'speed voltages', which means they are induced by the rotation of the reference frame at the speed of ω .

The stator and rotor flux linkage appearing in equation 3.2 are the functions of stator and rotor currents, as shown in:

$$\begin{aligned}\vec{\psi}_s &= L_s \vec{i}_s + L_m \vec{i}_r \\ \vec{\psi}_r &= L_m \vec{i}_s + L_r \vec{i}_r\end{aligned}\tag{3.3}$$

where:

$L_s = L_{l_s} + L_m$ - Stator self-inductance (H)

$L_r = L_{l_r} + L_m$ - Rotor self-inductance (H)

L_{l_s}, L_{l_r} - Stator and rotor leakage inductance (H)

L_m - Magnetizing inductance (H)

3.2 Frames of Reference

3.2.1 Introduction

Frames of reference have been studied for many years to study the movement of bodies. The reference frame theory plays a crucial role in the modelling, simulation and analysis of three-phase systems. It is widely used in advanced control methods to help reduce the sophistication of design and complexity of algorithms. There are three significant kinds of reference frame used in three-phase electrical systems, namely, the natural, stationary and synchronous reference frame. Each of these frames is applied to certain parts of design and analysis, and with some degree of complexity. They cannot be used interchangeably. For example, PI controllers solely require the variables of a DC nature [2].

3.2.2 Natural Reference Frame (*abc* - axis)

This is an unaltered three-phase stationary reference which has a speed (ω) of zero with respect to space. Three-phase quantities have a phase difference of 120° or $2\pi/3$; each oscillating sinusoidally at the angular frequency of the supply/source (ω_s) with respect to time. In AC rotary machines this is known as the synchronous frequency. It represents a true correlation between the mathematical model and the architecture of the practical machine/power converter. Therefore the switching pulses of the power electronic converter are modulated in this frame [2], [15].

3.2.3 Stationary Reference Frame ($\alpha\beta$ - axis)

The $\alpha\beta$ reference frame exhibits a similar oscillatory nature to the previous abc reference frame but only representing two-phase quantities which are displaced by 90° with respect to angular displacement. This reduction in the number of phases reduces the complexity of control and analysis [2], [12]. Direct torque control (DTC) and space vector modulation (SVM) can be performed in this frame of reference. In synchronization of the balanced and harmonic-free grid, the time position θ_g can be easily obtained by taking the inverse tangent of the ratio v_β/v_α [9]. This frame is also useful in the detecting of sequence decomposition of unbalanced grid voltage by DSOGI.

3.2.4 Synchronous Rotating Frame (dq - axis)

The three-phase variables in the abc natural reference frame can be reduced down to two synchronously rotating vectors defined by d (direct) and q (quadrature) axes [15]. All variables in this frame are expressed in time-invariant DC nature which makes it a viable frame in the design of control systems, especially in the tuning of PI regulators. A dq -frame is widely used in vector control techniques, mainly in stator-orientated control (SVOC) and field-orientated control SFOC. The dq transformation is given by

$$\begin{bmatrix} f_d \\ f_q \end{bmatrix} = \frac{2}{3} \begin{bmatrix} \cos(\theta) & \cos(\theta - \frac{2\pi}{3}) & \cos(\theta + \frac{2\pi}{3}) \\ -\sin(\theta) & -\sin(\theta - \frac{2\pi}{3}) & -\sin(\theta + \frac{2\pi}{3}) \end{bmatrix} \begin{bmatrix} f_a \\ f_b \\ f_c \end{bmatrix} \quad (3.4)$$

with f_a , f_b , and f_c representing any three-phase quantities (voltages, currents and fluxes) in the natural reference frame [11].

3.2.5 Transformation of Reference Frames

By substituting $\omega = \omega_s$, the arbitrary reference frame model is transformed to synchronous (dq) reference frame. The components are shown in Figure 3.2.

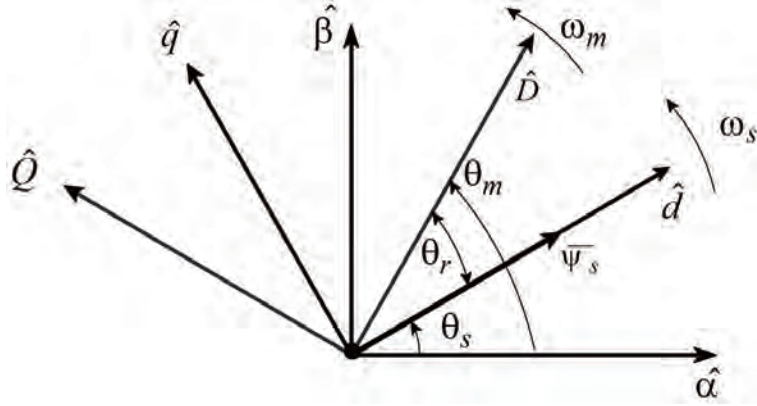


Figure 3.2 Reference frame transformation

The dq frame quantities can be transformed back to abc frame by taking an inverse of the matrix of Equation 3.4 [15] where

$$\begin{bmatrix} f_a \\ f_b \\ f_c \end{bmatrix} = \begin{bmatrix} \cos(\theta) & -\sin(\theta) \\ \cos(\theta - \frac{2\pi}{3}) & -\sin(\theta - \frac{2\pi}{3}) \\ \cos(\theta + \frac{2\pi}{3}) & -\sin(\theta + \frac{2\pi}{3}) \end{bmatrix} \begin{bmatrix} f_d \\ f_q \end{bmatrix} \quad (3.5)$$

The mechanical behaviour of the induction machine is determined by the speed and torque relationships given by

$$T_{em} = \frac{3P}{4} (\psi_{ds} i_{qs} - \psi_{qs} i_{ds}) \quad (3.6)$$

$$J \frac{d\omega_{rm}}{dt} = T_{em} - T_m - D\omega_{rm} \quad (3.7)$$

3.3 Vector Control of DFIG

3.3.1 Introduction

The RSC converter is at the core of the DFIG control system as it responsible for speed-torque/power control and reactive power generated by the stator side of the DFIG. This is achievable by adjusting the rotor voltage and current in the synchronous reference frame. The torque/power outer control loop computes the rotor current references i_{dqr}^* to be tracked by the inner control loop. Inner current loop regulates rotor current i_{dqr} to keep track of of i_{dqr}^* in order to calculate rotor voltage reference v_{dqr}^* to be fed to a PWM [12].

The GSC is responsible for maintaining the DC bus voltage and control the reactive power of the grid side converter. The control is analogous to the RSC. The outer loop regulates the DC bus voltage V_{bus} to keep track of its reference V_{bus}^* and outputs the grid reference current i_{dgg}^* while the inner current loop regulates the grid current. Both control blocks need to keep track of the stator voltage position θ_s in order to maintain the synchronization of the dq reference frame with the grid voltage [33], [13].

3.3.2 Grid Synchronization

Any phase difference between the back-to-back converter (BTB) converter and the grid can potentially cause undesirable surge current. Therefore the control of BTB converter has to keep track of θ_s . The position of the stator flux vector can be estimated simply taking the inverse tan of α and β

components of the stator voltage as shown in

$$\theta_s = \arctan \left(\frac{v_{\beta s}}{v_{\alpha s}} \right) \quad (3.8)$$

However, this method is not effective in the case of distorted and unbalanced grid voltages due to non-linear loads present in the grid. The phase-locked loop (PLL) proves to be a better solution to this problem as it incorporates a voltage-controlled oscillator block to synchronize a distorted voltage signal [12], [13].

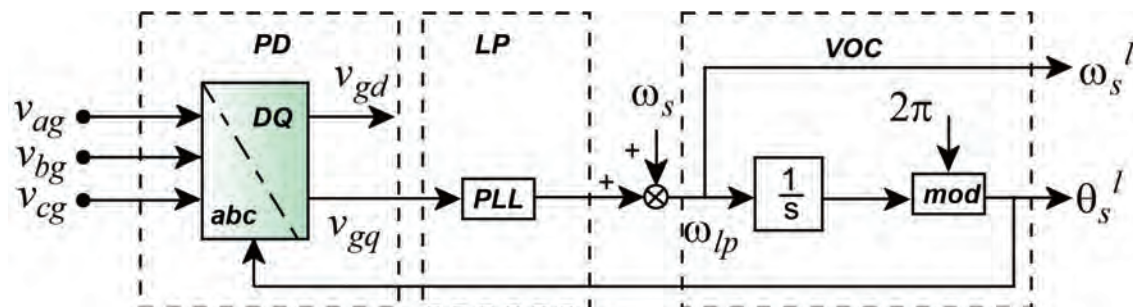


Figure 3.3 SRF PLL diagram [12]

3.3.3 Alignment of Reference Frame

In the SFOC, the d-axis is aligned with the stator flux vector as illustrated in Figure 3.4. With this alignment, the component of the stator flux in q -axis is equal to zero ($\psi_{qs} = 0$). As a result of this alignment, the stator active power becomes proportional to the rotor current in q -axis while the stator reactive power is proportional to the rotor current in d-axis [9] [3].

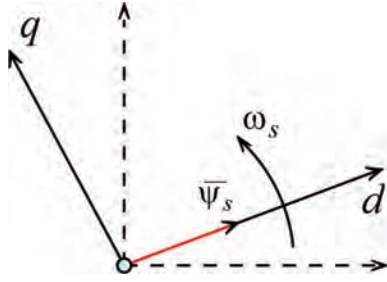


Figure 3.4 Alignment of d-q reference frame with the stator flux space vector

3.4 Vector Control of the GSC

3.4.1 Outer Control Loop

The control system of the grid side converter (GSC) must maintain the dc bus voltage v_{dc} in order to tolerate fluctuations and transients during dynamic operation. In addition the dc-bus voltage should be higher than the peak line-to-line grid voltage $V_{g,ll}$ [2]. The PWM scheme used with the GSC has a modulation index m_a . A modulation index value of 0.8 is selected in order to allow 20 % adjustment margin during transients [2]. The DC-bus voltage reference is determined by the modulation index and the grid rated line-to-line voltage as shown in

$$v_{dc}^* = \frac{\sqrt{2}V_{g,ll}}{m_a} \quad (3.9)$$

where $0 < m_a \leq 1$

The active and reactive power flow of the grid side converter can be expressed in terms of the grid

voltage V_g and the grid side filter current I_g in dq reference frame:

$$P_g = \frac{3}{2}(v_{dg}i_{dg} + v_{qg}i_{qg}) \quad (3.10)$$

$$Q_g = \frac{3}{2}(v_{qg}i_{dg} - v_{dg}i_{qg})$$

The GSC manages the dc-bus voltage level v_{dc} and reactive power flow between the BTB and the grid. Using the circuit model shown in Figure 2.5 the dq reference frame equations can be derived. By applying the stator voltage-orientated control principle to the active and reactive powers in Equation 3.10, they can be simplified to

$$P_g = \frac{3}{2}v_{dg}i_{dg} \quad (3.11)$$

$$Q_g = -\frac{3}{2}v_{dg}i_{qg}$$

It can be observed that the active power and reactive powers of the grid side converter P_g and Q_g are proportional to i_{dq} and i_{qg} respectively [12], [13]. The energy stored in the dc bus capacitor of the BTB converter is given by

$$W = \frac{1}{2}C_{bus}V_{bus}^2 \quad (3.12)$$

where C_{bus} is the dc bus capacitance and V_{bus} is the voltage of the dc bus. By taking the derivative of Equation 3.12 the expression for power flow between the RSC and GSC can be derived so that

$$\frac{dW}{dt} = \frac{1}{2}C_{bus}\frac{V_{bus}^2}{dt} = -P_{gsc} - P_r \quad (3.13)$$

where P_{gsc} is the power absorbed or delivered by the grid side converter and P_r is the delivered or consumed or delivered by the rotor circuit. P_r can be expressed in terms of stator referred rotor

voltages and currents in the dq reference frame as described in

$$P_r = \frac{3}{2}(v_{dr}i_{dr} + v_{qr}i_{qr}) \quad (3.14)$$

$$Q_r = \frac{3}{2}(v_{qr}i_{dr} - v_{dr}i_{qr})$$

The active power transfer of the rotor side converter P_r can be considered as a disturbance and excluded from the design of the V_{bus} regulator. This means the open-loop transfer function of the dc bus voltage PI controller can be written as:

$$\frac{V_{bus}^2(s)}{I_{dg}(s)} = P_{dc}(s) = -\frac{3v_{dg}}{sC_{bus}} \quad (3.15)$$

The transfer function $P_{dc}(s)$ has a single pole, hence it is susceptible to disturbances. The improved disturbance rejection can be achieved by using an additional control loop that can speed up the natural response of the plant. A negative feedback loop proposed in the literature adds an artificial pole with a value of $3v_dG_{dc}$ [13] so that

$$\frac{V_{bus}^2(s)}{I_{dg}(s)} = \frac{P_{dc}(s)}{1 + P_{dc}(s)G_{dc}} = -\frac{3v_{dg}}{sC_{bus} + 3v_{dg}} = M_{dc}(s) \quad (3.16)$$

where G_{dc} is the inner feedback loop gain, G_{dc} is directly proportional to the desired speed response of the plant, which means choosing a larger value of G_{dc} is advantageous. The compensation transfer function to facilitate the zero-pole cancellation can be defined as:

$$K_{dc}(s) = \frac{sK_p^v + K_i^v}{s} = \frac{K_p^v}{s} \left(s + \frac{K_i^v}{K_p^v} \right) \quad (3.17)$$

where K_p^v and K_i^v are the proportional and integral gains of the dc bus voltage regulator which are tabulated in Table 3.1. The system is shown in Figure 3.5. Therefore, by choosing $K_i^v/k - p^v = 3v_dG_{dc}/C_{bus}$ and $3K_p^v v - d/C_{bus} = 1/\tau_{dc}$, the closed loop controller gain can be derived:

$$Y_{dc}(s) = \frac{1}{s\tau_{dc} + 1} \quad (3.18)$$

| Parameter | Value | Units | Description |
|------------|---------|---------|--|
| k_{pg}^v | -1000 | pu | V_{bus} controller proportional gain |
| k_{ig}^v | -6000 | pu | V_{bus} controller integral gain |
| k_{pg}^i | 0.1508 | pu | GSC current controller proportional gain |
| k_{ig}^i | 28.4245 | pu | GSC current controller integral gain |
| T_{gsc} | 250 | μ s | GSC controller sampling time |

Table 3.1 GSC controller parameters

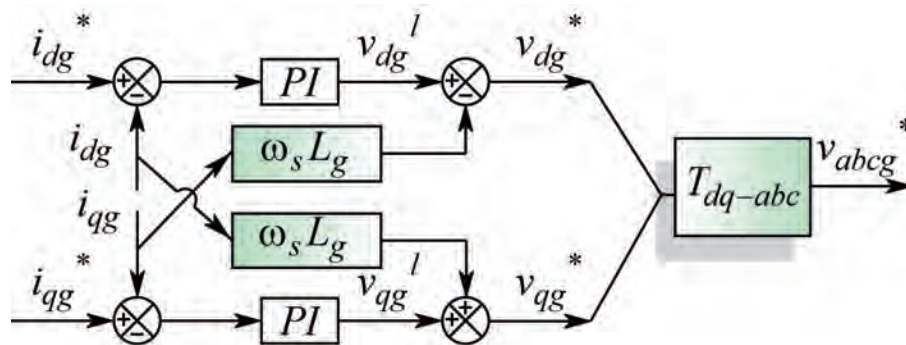


Figure 3.5 Control loops of the grid side converter [13]

3.4.2 Inner Current Control Loop

The dynamic behaviour of the GSC currents in the dq reference frame can be modelled as follows:

$$v_{dg} = -L_g \frac{di_{dg}}{dt} - R_g i_{dg} + \omega_s L_g i_{qg} + v_d \quad (3.19)$$

$$v_{qg} = -L_g \frac{di_{qg}}{dt} - R_g i_{qg} - \omega_s L_g i_{dg} + v_q$$

where R_g and L_g are the grid side filter resistance and inductance respectively, v_{dg} and v_{qg} are

the dq components of the grid side converter voltage. The reactive power absorbed or delivered

is expressed by Equation 3.11. Therefore if in Equation 3.19 the coupling terms $\omega_s L_g i_{dqg}$ are considered as disturbance the open loop transfer function can be defined as

$$G(s) = \frac{i_{dq}(s)}{v_{dq}(s)} = \frac{1}{sL_g + R_g} \quad (3.20)$$

The compensation transfer function is expressed in terms of:

$$B(s) = k_{pg}^i + \frac{k_{ig}^i}{s} \quad (3.21)$$

A closed-loop transfer function is expressed in terms of $G(s)$ and $B(s)$, hence:

$$M(s) = \frac{G(s)B(s)}{1 + G(s)B(s)} \quad (3.22)$$

By comparing the zeros in Equation 3.21, the PI controller proportional and integral gains can be obtained. These can later be tuned for optimum stability of the system. By equating the closed

loop transfer function $M(s)$ to the generalized second order transfer function:

$$M(s) = \frac{sk_{pg} + k_{ig}}{s^2L_g + (k_{pg} + R_g)s + k_{ig}} = \frac{K\omega_n^2}{s^2 + 2\zeta\omega_n s + \omega_n^2} \quad (3.23)$$

and using the 2 MW DFIG parameters in Table B.2, the PI controller gains can be calculated:

$$\begin{aligned} k_{pg} &= 2\zeta\omega_n L_g - R_g \\ k_{ig} &= \omega_n^2 L_g \end{aligned} \quad (3.24)$$

They are tabulated in Table 3.1. The system is shown in Figure 3.6.

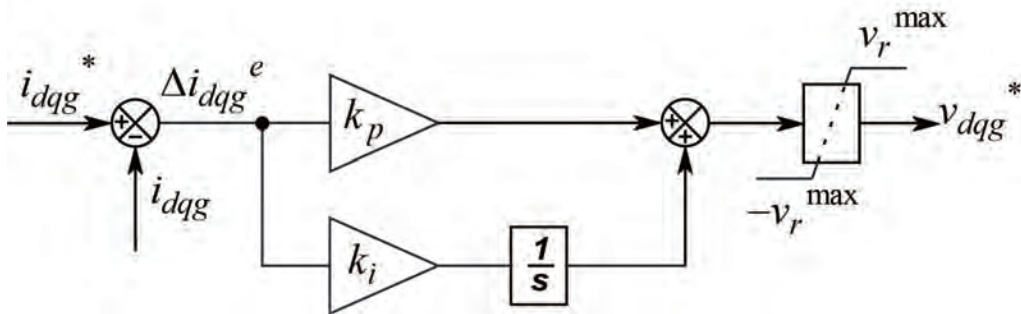


Figure 3.6 PI regulator of the inner current loops of the GSC

3.5 Control of the RSC

3.5.1 Outer Control Loop

The active and reactive power control is central to the control of the DFIG. The control of these variables is realized by controlling the currents circulating between rotor winding and RSC in the direct and quadrature reference frame (i.e. i_{dr} and i_{qr}). Maximum power point tracking is achieved by controlling electromagnetic torque T_{em} , while the power factor is adjusted by controlling the stator reactive power Q_s . These control objectives can be realized by regulation of rotor currents through the RSC.

The active power can be expressed in terms of stator voltage and current components in the dq reference frame as:

$$P_s = \frac{3}{2}(v_{ds}i_{ds} + v_{qs}i_{qs}) \quad (3.25)$$

$$Q_s = \frac{3}{2}(v_{qs}i_{ds} - v_{ds}i_{qs})$$

The dynamic stator voltage equations can be written in the dq reference frame:

$$\begin{aligned} v_{ds} &= R_s i_{ds} + \frac{d\psi_{ds}}{dt} - \omega_s \psi_{qs} \\ v_{qs} &= R_s i_{qs} + \frac{d\psi_{qs}}{dt} + \omega_s \psi_{ds} \end{aligned} \quad (3.26)$$

where ψ_{ds} and ψ_{qs} are the dq components of the stator flux. In Equation 3.26 the voltage drop across the stator resistance can be neglected. Also, the derivative terms can be eliminated by the assumption that at the steady-state the stator flux in the dq reference frame is constant with respect

to time (i.e. $\frac{d\psi_{ds}}{dt} = 0$ and $\frac{d\psi_{qs}}{dt} = 0$). Therefore Equation 3.26 is reduced to Equation 3.27

$$\begin{aligned} v_{ds} &= -\omega_s \psi_{qs} \\ v_{qs} &= +\omega_s \psi_{ds} \end{aligned} \quad (3.27)$$

The stator flux dq components can be written as a function of stator and rotor currents:

$$\begin{aligned} \psi_{ds} &= L_s i_{ds} + L_m i_{dr} \\ \psi_{qs} &= L_s i_{qs} + L_m i_{qr} \end{aligned} \quad (3.28)$$

where $L_s = L_{ls} + L_m$ and $L_r = L_{lr} + L_m$. By orienting the dq reference frame with the stator flux vector $\bar{\psi}_s$ the q component of the stator flux becomes zero. It can be then deduced from Equation 3.27 that the d axis component of the stator voltage also equates to zero. This means

$$\begin{aligned} \psi_{ds} &= \psi_s \quad \text{and} \quad \psi_{qs} = 0 \\ v_{ds} &= 0 \quad \text{and} \quad v_{qs} = V_s \end{aligned} \quad (3.29)$$

By substituting the Equations 3.27, 3.29 and 3.28 to 3.25 the relationship between the stator active and reactive power references and rotor current references can be expressed as shown in

$$\begin{aligned} i_{dr}^* &= \frac{2L_s}{3L_m v_{qs}} Q_s^* - \frac{1}{\omega_s L_m} v_{qs} \\ i_{qr}^* &= \frac{-2L_s}{3L_m v_{qs}} P_s^* \end{aligned} \quad (3.30)$$

The relationship between the electromagnetic torque and the stator power is simple $P_s = T_{em} \omega_s / p$,

therefore the equation for the rotor q – axis current can be re-written as:

$$i_{qr}^* = \frac{-2L_s}{3pL_m v_{qs}} \omega_s T_{em}^* \quad (3.31)$$

For this research, the active and reactive power references are not tracked with the actual variables.

However, they are the inputs to the calculation of references in the dual control of asymmetrical voltage dips.

3.5.2 Inner Current Control Loop

The RSC only adjust the three-phase voltage at the terminals of the rotor circuit. In order to improve the robustness and ensure the reliability of the RSC control system, it is necessary to regulate and keep track of the rotor currents as well. The dynamic expression of the rotor voltages in dq reference frame can be written as:

$$\begin{aligned} v_{dr} &= R_r i_{dr} + \frac{d\psi_{dr}}{dt} - \omega_r \psi_{qr} \\ v_{qr} &= R_r i_{qr} + \frac{d\psi_{qr}}{dt} + \omega_r \psi_{dr} \end{aligned} \quad (3.32)$$

The stator power is controlled through the rotor side. This is shown in Figure 3.7. Therefore it is not possible to ignore the dynamics of the rotor resistance and rotor flux as they form the basis of the inner control loop. The dq reference frame components of the rotor flux can be expressed in terms of stator and rotor currents, as shown by:

$$\begin{aligned} \psi_{dr} &= L_r i_{dr} + L_m i_{ds} \\ \psi_{qr} &= L_r i_{qr} + L_m i_{qs} \end{aligned} \quad (3.33)$$

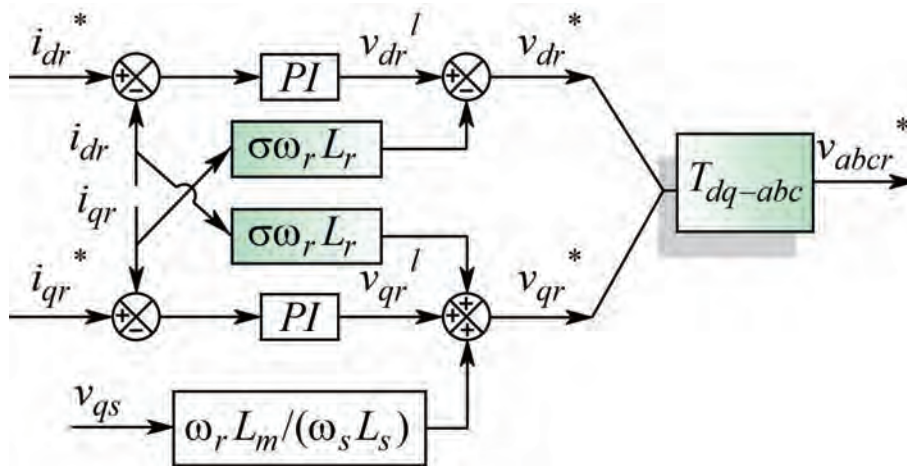


Figure 3.7 Control block diagram of the Rotor side converter under normal grid conditions

In order to derive the open loop controller transfer function dq rotor voltages must be the function of rotor currents and constants. This can be achieved by substituting Equations 3.28 into 3.33 and then 3.33 into 3.32 which results in

$$\begin{aligned} v_{dr} &= R_r i_{dr} + \sigma L_r \frac{di_{dr}}{dt} - \omega_r \sigma L_r i_{qr} \\ v_{qr} &= R_r i_{qr} + \sigma L_r \frac{di_{qr}}{dt} + \omega_r \sigma L_r i_{dr} + \omega_r \frac{L_m}{\omega_s L_s} v_{qs} \end{aligned} \quad (3.34)$$

where $\sigma = 1 - L_m^2 / (L_s L_r)$. The coupling terms $\omega_r \sigma L_r i_{dqr}$ and flux perturbation term $\omega_r L_m v_{qs} / (\omega_s L_s)$ are seen as a disturbance in the controller, however they can be compensated for by the closed-loop controller. These terms can be ignored in the PI controller design and then be cancelled at the output of the controller to improve transient stability. Therefore the open-loop gain of the inner current loops in s domain can be expressed as

$$G(s) = \frac{I_{dr}(s)}{V_{dr}(s)} = \frac{1}{R_r + s\sigma L_r} \quad (3.35)$$

The compensation transfer function is expressed as

$$C(s) = k_p + \frac{k_i}{s} \quad (3.36)$$

A closed-loop transfer function is expressed in terms of $G(s)$ and $C(s)$ so that

$$H(s) = \frac{G(s)C(s)}{1 + G(s)C(s)} \quad (3.37)$$

By comparing the zeros in

$$H(s) = \frac{sk_p + k_i}{s^2 \sigma L_r + (k_p + R_r)s + k_i} = \frac{K \omega_n^2}{s^2 + 2\zeta \omega_n s + \omega_n^2} \quad (3.38)$$

the PI controller proportional and integral gains can be obtained. These can later be tuned for optimum stability of the system. By equating the closed-loop transfer function $H(s)$ to the gener-

alized second order transfer function, and by using the 2 MW DFIG parameters in Table B.1 the PI controller gains can be calculated using

$$\begin{aligned} k_p &= 2\zeta\omega_n\sigma L_r - R_r \\ k_i &= \omega_n^2\sigma L_r \end{aligned} \quad (3.39)$$

and they are tabulated in Table 3.2. The PI controller of the inner current loops for the RSC is shown in Figure 3.8 where the output signal of the PI controller must be bound to the maximum rotor voltage $V_{r,max}$ in order to avoid converter saturation.

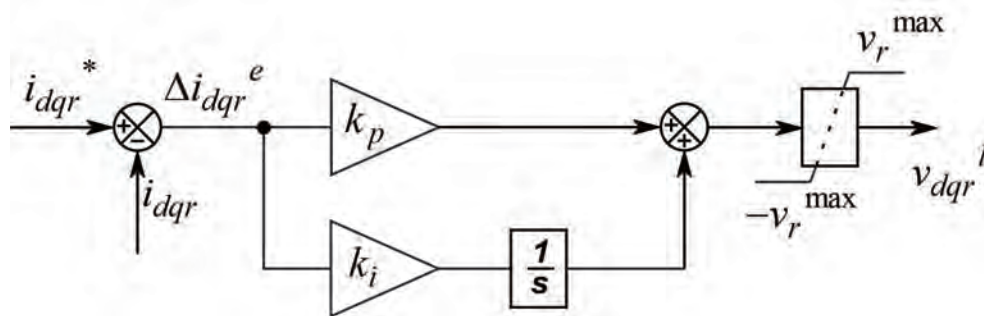


Figure 3.8 PI regulator of the inner current loops

| Parameter | Value | Unit | Description |
|-----------|----------|---------|--|
| k_p^n | 2032 | pu | Speed controller proportional gain (k_{pd}^n and k_{pq}^n) |
| k_i^n | 81280 | pu | Speed controller integral gain (k_{id}^n and k_{iq}^n) |
| k_p^i | 0.5771 | pu | RSC current controller proportional gain |
| k_i^i | 491.5995 | pu | RSC current controller integral gain |
| T_{rsc} | 250 | μ s | RSC controller sampling time |

Table 3.2 RSC controller parameters

The causes and impacts of voltage dips on the operation of the DFIG have been discussed in Chapter 2. In Chapter 3 the modelling and control are performed under the assumption that the

DFIG WECS operates under stable grid voltage conditions. Under such conditions, it is assumed that the stator flux has a constant amplitude and lags the grid voltage by 90° . This is only true in steady-state and not in the case of a voltage transient. The presence of natural flux due to a voltage dip induces a high terminal voltage in the rotor circuit, and this can saturate the RSC and cause a loss of control.

The asymmetrical voltage dips induces a backwards rotating flux in the stator windings. This introduces the oscillations in stator current and electromagnetic torque at twice the grid frequency. Since the traditional vector control strategy only acknowledges the forward rotating flux, the loss of control may occur during these voltage dips.

3.5.3 GSC Current Reference Under Asymmetrical Dips

In the occurrence of asymmetrical voltage dips, the GSC must be controlled to help reduce the second-order oscillation of grid active power. The active and reactive power flow between the grid and the BTB can be expressed as:

$$P_g = \frac{3}{2} \text{Re} [\bar{v}_g \bar{i}_g^*] \quad (3.40)$$

$$Q_g = \frac{3}{2} \text{Im} [\bar{v}_g \bar{i}_g^*]$$

where v_g and i_g are the space vectors of the converter current and grid voltage, respectively. By applying Equation 2.14 the grid voltage and current can be further decomposed into positive and negative sequence phasors:

$$\begin{aligned} \bar{v}_g &= V_1 e^{j\omega_g t} + V_2 e^{-j\omega_g t} = (v_{d1} + jv_{q1})e^{j\omega_g t} + (v_{d2} + jv_{q2})e^{-j\omega_g t} \\ \bar{i}_g &= I_1 e^{j\omega_g t} + I_2 e^{-j\omega_g t} = (i_{d1} + ji_{q1})e^{j\omega_g t} + (i_{d2} + ji_{q2})e^{-j\omega_g t} \end{aligned} \quad (3.41)$$

where the subscripts 1 and 2 denote positive and negative sequence variable respectively, and ω_g refers to the grid angular frequency. By solving Equations 3.40 and 3.41 the active and reactive powers are found to be the algebraic sum of fundamental and oscillatory components as presented by

$$\begin{aligned} P &= P_0 + P_{cos} \cos(2\omega_g t) + P_{sin} \sin(2\omega_g t) \\ Q &= Q_0 + Q_{cos} \cos(2\omega_g t) + Q_{sin} \sin(2\omega_g t) \end{aligned} \quad (3.42)$$

Under balanced grid or particularly in the case of symmetrical voltage dip the negative sequence components are zero, i.e $v_{d2} = 0$, $v_{q2} = 0$, $i_{d2} = 0$ and $i_{q2} = 0$. Consequently, as it may be observed using

$$\begin{bmatrix} P_0 \\ Q_0 \\ P_{cos} \\ P_{sin} \\ Q_{cos} \\ Q_{sin} \end{bmatrix} = \frac{3}{2} \begin{bmatrix} v_{d1} & v_{q1} & v_{d2} & v_{q2} \\ v_{q1} & -v_{d1} & v_{q2} & -v_{d2} \\ v_{d2} & v_{q2} & v_{d1} & v_{q1} \\ v_{q2} & -v_{d2} & -v_{q1} & v_{d1} \\ v_{q2} & -v_{q2} & -v_{q1} & -v_{d1} \\ -v_{d2} & -v_{q2} & v_{d1} & v_{q1} \end{bmatrix} \begin{bmatrix} i_{d1} \\ i_{q1} \\ i_{d2} \\ i_{q2} \end{bmatrix} \quad (3.43)$$

the oscillatory components of the powers (P_{cos} , Q_{cos} , P_{sin} , Q_{sin}) will not appear in the powers. The terms Q_{sin} and Q_{cos} present the fluctuations of reactive power, and since such variations do not affect the DC bus voltage, the terms can be eliminated in the matrix so that

$$\begin{bmatrix} P_0 \\ Q_0 \\ P_{cos} \\ P_{sin} \end{bmatrix} = \frac{3}{2} \begin{bmatrix} v_{d1} & v_{q1} & v_{d2} & v_{q2} \\ v_{q1} & -v_{d1} & v_{q2} & -v_{d2} \\ v_{d2} & v_{q2} & v_{d1} & v_{q1} \\ v_{q2} & -v_{d2} & -v_{q1} & v_{d1} \end{bmatrix} \begin{bmatrix} i_{d1} \\ i_{q1} \\ i_{d2} \\ i_{q2} \end{bmatrix} \quad (3.44)$$

The transferred grid active power P_g is proportional to the level of the DC bus voltage. In this way,

the fluctuation of P_g translates to the fluctuation of the DC bus voltage. Therefore P_{sin} and P_{cos} must be set to zero in order to achieve a constant DC bus voltage. By obtaining the inverse matrix of Equation 3.44 the grid reference currents are calculated according to

$$\begin{bmatrix} i_{d1} \\ i_{q1} \\ i_{d2} \\ i_{q2} \end{bmatrix} = \frac{2P_0}{3D} \begin{bmatrix} v_{d1} \\ v_{q1} \\ -v_{d2} \\ -v_{q2} \end{bmatrix} + \frac{2Q_0}{3R} \begin{bmatrix} v_{q1} \\ -v_{d1} \\ v_{q2} \\ -v_{d2} \end{bmatrix} \quad (3.45)$$

where:

$$\begin{aligned} D &= (v_{d1}^2 + v_{q1}^2) - (v_{d2}^2 + v_{q2}^2) \\ R &= (v_{d1}^2 + v_{q1}^2) + (v_{d2}^2 + v_{q2}^2) \end{aligned} \quad (3.46)$$

3.5.4 Demagnetizing Current Control

The idea of natural flux evolution has been deeply discussed in Chapter 2. The rotor current control references can be modified in order to accelerate the decay of natural flux where the demagnetizing current is injected as shown in Figure 3.9. The combined injection also adds the the injection of negative sequence current in order to oppose the backwards rotating stator flux induced by an asymmetrical voltage dip [9], [24].

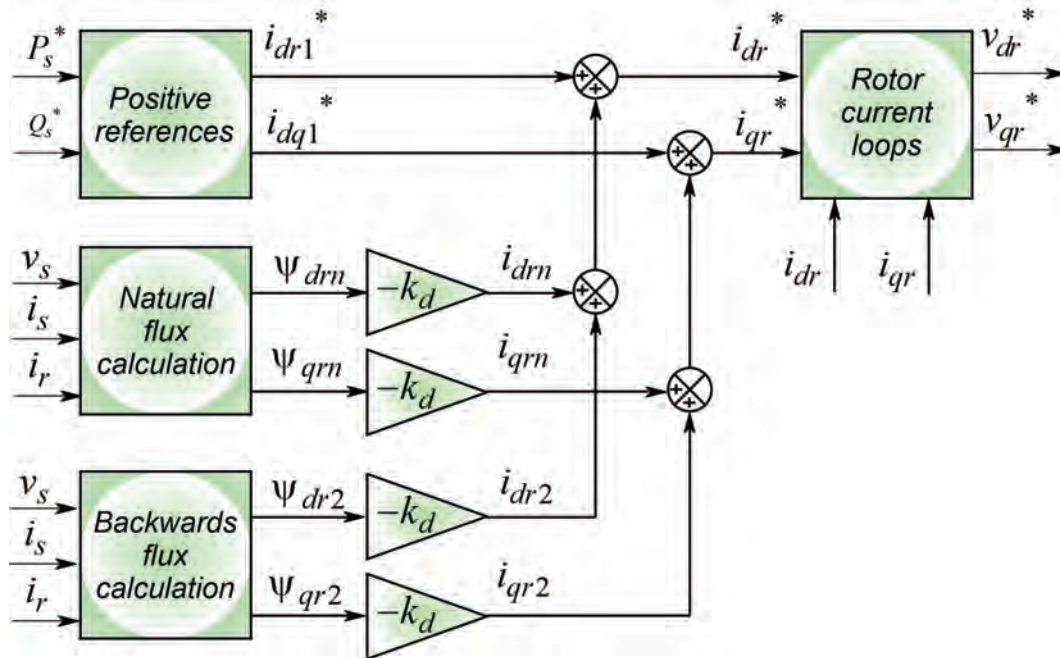


Figure 3.9 Combined injection of demagnetizing and negative sequence current

3.5.5 Control Targets for RSC Under Asymmetrical Dips

The issue of loss of control during an unbalanced grid voltage can be addressed through dual control rotor currents. The dual control demands the sequence decomposition of measured voltages and currents and the calculation of positive and negative current references. There is a variety of sequence decomposition methods proposed in literature rated according to their ability to reject second-order fluctuations of variables.

The rotor current references are calculated according to specific target; this includes minimizing the: Stator power oscillations, stator current, torque ripple, rotor current and rotor voltage. The rotor current references to achieve these control targets are calculated according to the equations shown in Appendix A.2 which have been derived in the literature [9].

Chapter 4

Simulation and Simulation Results

4.1 Simulation Procedure

The control of the back-to-back converter (BTB) converter is alone a wide-ranging topic that includes numerous methods, it was therefore, necessary to make choices that will focus most of the study on the primary goal, and hence eliminating the research burden. This section briefly reports on the choices made by the author and discusses why those choices were made. Outcomes and conclusions of this research are realized mainly by quantitative analysis based on MATLAB/Simulink[®] as a computational tool.

4.1.1 Equipment and Software

Machine Test Bench

The experimental part of the research is based on the laboratory scale 0.8 kW 400 V wind power turbine generator at the UKZN. The test bench incorporates a DFIG control unit and a Servo machine test stand, both of which can be connected to a PC via a USB link. The test equipment compatibility with Labsoft[®] control interface software offers a robust and more convenient method of data acquisition and control.

The machine test bench as shown in Figure 4.2 is a piece of state-of-the-art laboratory-scale simulation equipment designed by Lucas Nuelle; which incorporates protection systems against faults and grid code infringement. It is impossible, in as far as reasonably practicable, to bypass these protection systems in order to investigate the effects of voltage dips without protection. It is, therefore, necessary to implement a computer simulation model in order to analyze performance without these protection systems.

4.1.2 Apparatus and Procedure

It is necessary to provide clarity as to how the data was collected and analyzed. Below is a comprehensive description of the apparatus and procedure employed by the author in the machine test bench; where the numbers in brackets are the labels as shown in Figure 4.2:

- **Induction machine (1)** - the slip ring wound rotor induction machine acts as a generator

in the DFIG test bench. The machine nameplate ratings were recorded and are shown in Table B.3. All six stator winding ends are accessible, which allows the stator side to be connected as star or delta while the rotor is internal-star. The machine parameters of the induction machine were obtained using offline tests namely: DC tests for stator and rotor resistances; locked rotor test and a running light test (no load test), it was however not feasible to use these parameters in the MATLAB/Simulink simulation due to the lack of means to estimate the parameters for grid filter and the controller. Consequently, a convenient decision was taken to use DFIG parameters from the literature [34].

- **Grid fault simulator (5)** - the unit is used to experimentally study the three-phase voltage dips for this research. It is designed to simulate voltage dips of various types (three-phase, single-phase to ground and two-phase to ground), magnitudes and duration. This helps to create voltage dips in way that does not infringes the grid connection code The type of voltage dip of is set using 'MODE' function. Various levels of voltage dips for each phase can be set on the panel as shown in Figure 4.1.
- The voltage sags settings of L1, L2, L3 and fault duration (labelled as 'TIME' in Figure 4.1) are the critical components in the simulation of voltage dips since they are regulated by the grid code of South Africa as presented in Figure 2.1. Voltage sags can be independently set for each phase at a discrete levels of 0 %, 20 %, 40 %, 60 % and 100 %. Figure 4.1 is an example of a 40-40-20 asymmetrical voltage dip, this means L1 and L2 voltage amplitudes are reduced by 40 % while L2 is reduced by 20 % of the nominal grid voltage. Once all settings are in place the operator must press a 'START' button to initiate the preset on the grid side.
- **DFIG control unit (2)** - this is a core of the DFIG test bench, the power circuit and control unit of the BTB converter is inside this unit. It can be connected to the PC via a USB



Figure 4.1 A zoom-in of a dynamic grid fault simulator labelled as (5) in Figure 4.2

link, the data is acquired using the virtual instruments. The unit receives speed and torque measurements from the incremental encoder which is connected at the end of the main shaft. If PC mode is activated the unit can be controlled using virtual instruments in the PC. Virtual instruments offer useful features such as automatic grid synchronisation, power control and FRT monitor.

- **Servo machine test bench (8 and 4)** - In order to provide input mechanical power to the induction machine (1) the motor(4) is used. The servo machine test bench (8) is used in a speed control mode to run the generator up to speed. It can also emulate the aerodynamics of wind and turbine characteristics. For this research all the simulations were carried out at a speed of 1360 rpm.
- **Isolating transformer (6)** - The isolating transformer is employed on the grid side to step down the grid voltage to the nominal voltage of the DFIG control unit and the induction machine. The circuit breaker which is connected on the primary side plays a crucial role in the over-current protection of the grid side.
- **Power supply (3)** - 400 V power supply to provide a three-phase power to the DFIG control

unit. This also emulates a point of connection to the grid.

- **FRT Monitor (9)** - the behaviour of DFIG during the fault can be observed in pu system using the FRT monitor. The acquired data can be exported and saved as values in an excel sheet.

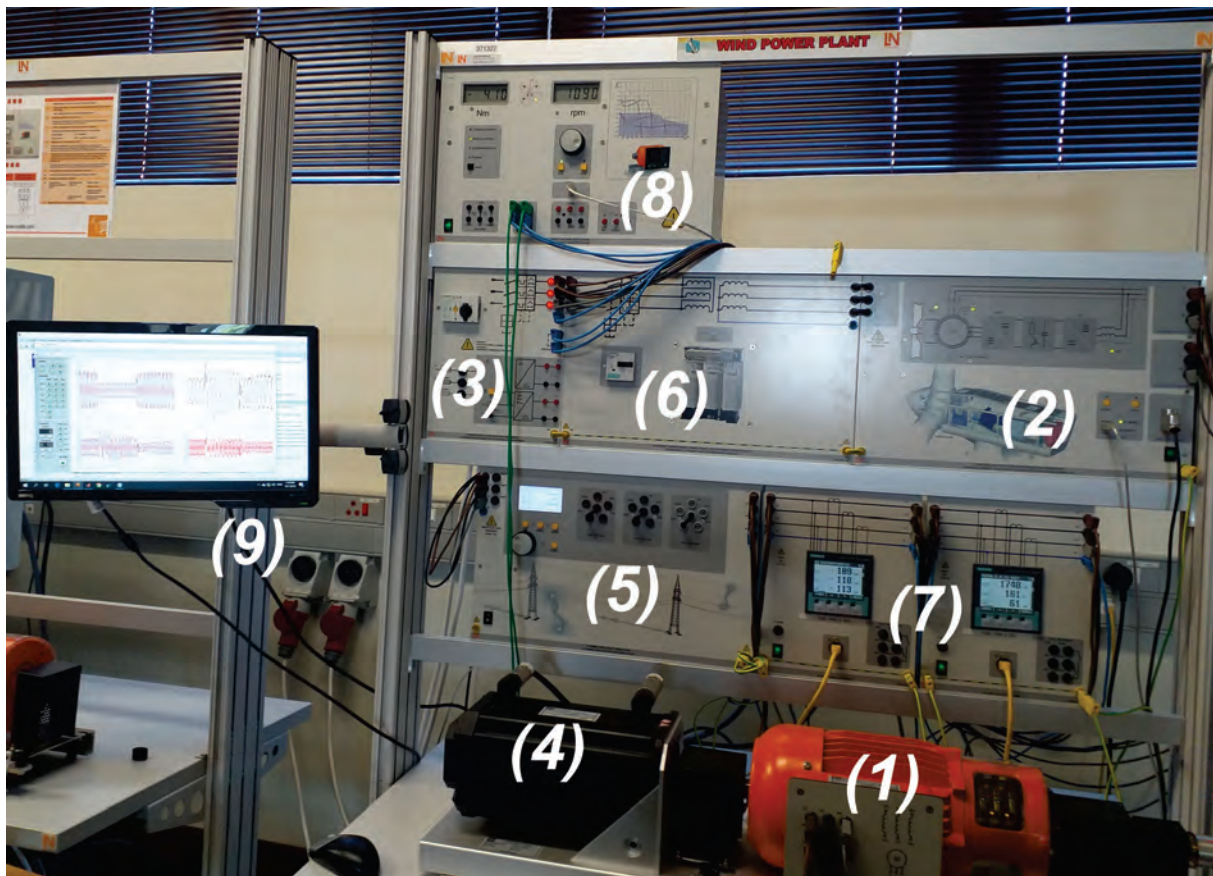


Figure 4.2 Lucas Nuelle DFIG machine test bench at the Smart grid laboratory

Data Acquisition

The grid simulator (5) works in synchronism with the FRT Monitor in Figure 4.3 to collect data. When the operator actuates the 'START' button the 'RECORD' button in (C) must be actuated as

well. This allows the operator to acquire data from the DFIG control unit which can be viewed on the monitor in Figure 4.2 (9) and can be later exported as a '.cls' file by selecting 'Values as Text' in (A) of Figure 4.3. The 'DEADBAND' allows the operator to step back in time, some few seconds before the fault occurrence in order to include healthy/previous conditions in the acquired data. For this research the DEADBAND was set at 0.10 seconds.

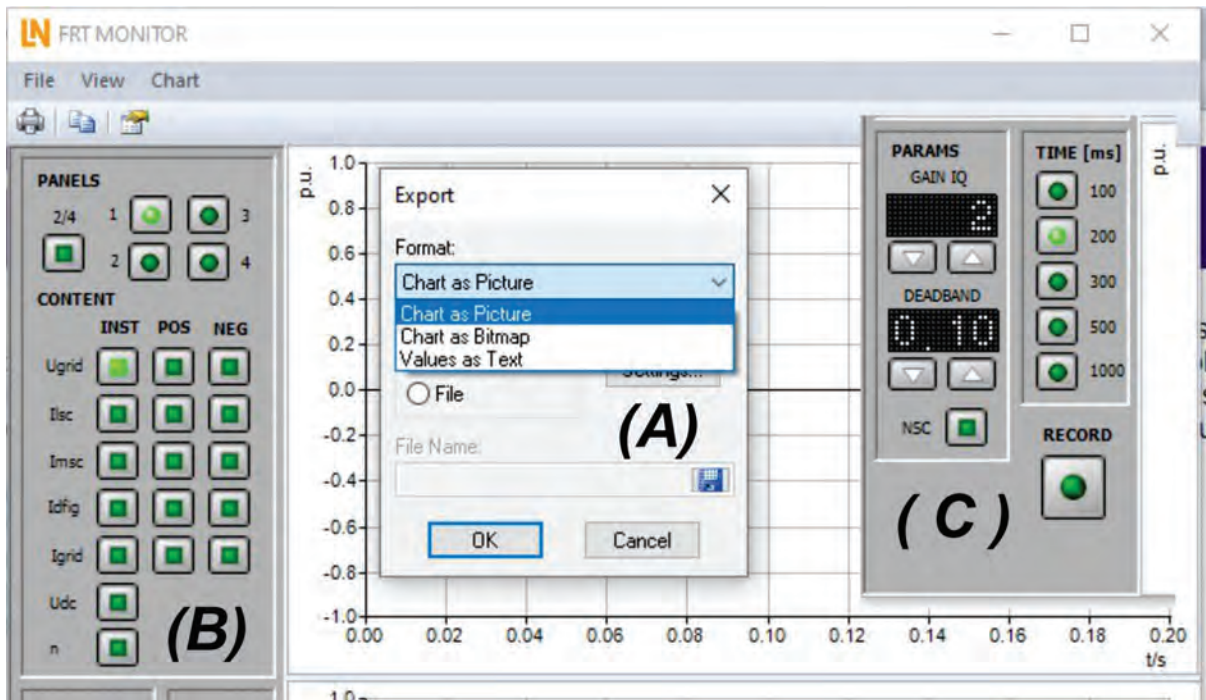


Figure 4.3 PC based Fault Ride-Through Monitor

The '.cls' files obtained from the FRT Monitor are then imported to MATLAB and converted to graphs for analysis. The FRT Monitor also allows the operator to include positive sequence 'POS' and negative sequence 'NEG' components in the output file as shown in label (B) of Figure 4.3.

4.1.3 Computer Simulation

The computational modelling in this research is based on MATLAB/Simulink[®]; the design of the control system is derived from mathematical models discussed in Chapter 3. Built-in power systems and power electronics libraries offered by MATLAB/Simulink[®] under Simscape power systems library are in synchronism with contemporary renewable energy technologies. This helps to achieve the simulation objectives more efficiently and reliably. The implementation of a DFIG is shown in Figure 4.4. The power circuit is easily achieved by a 'transformer' for stator to rotor normalization, series branches for DC capacitor and grid side filter and 2-L VSCs ('RSC' and 'GSC') which are connected back-to-back to form a BTB converter.

The challenging and fundamental part of the control under asymmetrical voltage dips is the calculation of rotor current references which requires sequence decomposition and filtering methods. Various techniques were proposed in the literature. However, due to the complexity of these techniques the author preferred the signal delay cancellation method (SDC) proposed in Figure 2.11 in Chapter 4. This can achieve the same goals with lesser computational work. The SRF-PLL plays an essential role in grid synchronisation, particularly under grid disturbances. In the simulation, the author used a complete PLL block found in MATLAB/Simulink.

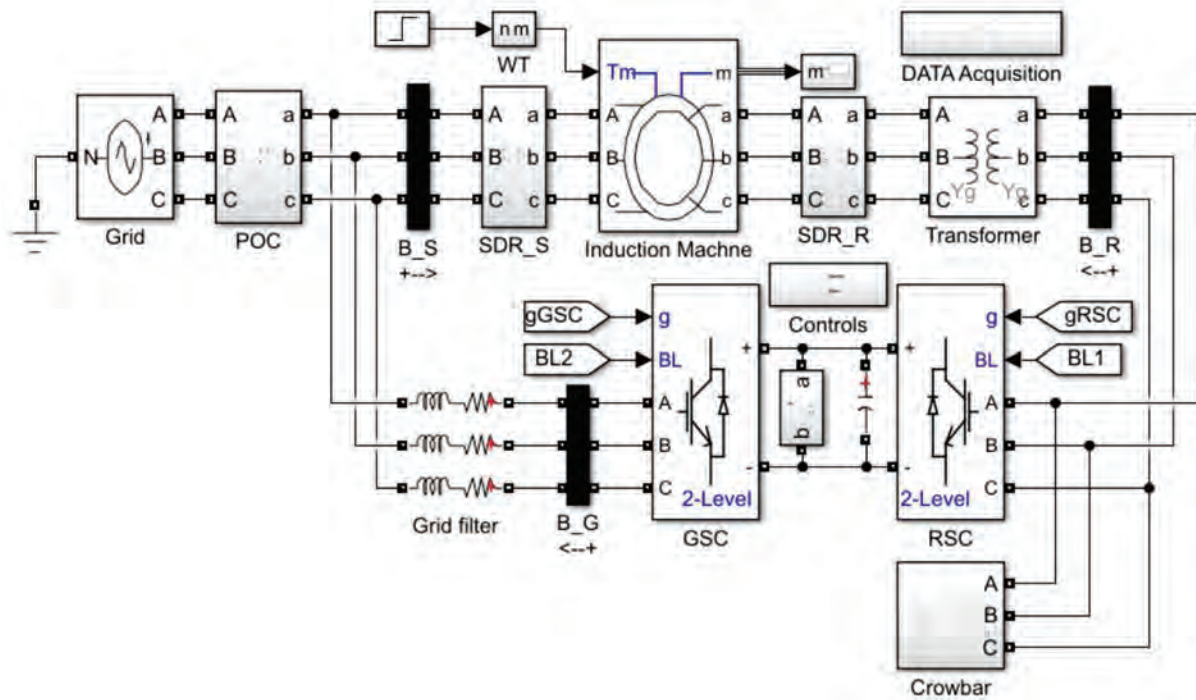


Figure 4.4 DFIG implementation in MATLAB/Simulink

Considering that the aerodynamics have been excluded from the study, it is therefore essential to acknowledge the source of mechanical torque for the simulated DFIG. The input mechanical torque to the induction machine is derived from a built-in wind turbine model shown in Figure 4.5, which can be found in the Simcape library under renewable energy in MATLAB/Simulink. It takes the pitch angle, generator speed and wind speed as inputs and generates torque with a maximum power point tracking (MPPT) algorithm. In this research, the pitch control is not analysed. Therefore the pitch angle is set to '0' (fully-pitched) for the entire operation.

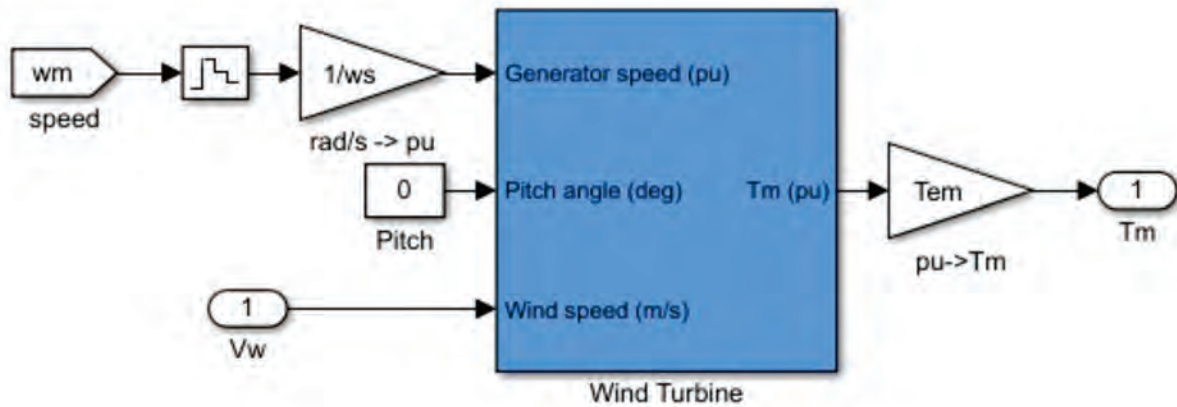


Figure 4.5 Wind turbine Simulink block, 'WT' in Figure 4.4

4.1.4 Concluding Remarks

The findings of this research are mainly realized by MATLAB/Simulink. In order to support the findings, the additional data is obtained through experimental work in the machine test bench. Although the actual values may not correlate, the observed behaviours under similar scenarios must converge to one relevant theory. The vector control method has been chosen over other control methods for this study.

4.2 Simulation Results

The proposed BTB converter protection strategies are verified by MATLAB/Simulink simulations using the 2 MW 690V DFIG unit whose parameters are presented in Table B.1. The outcomes of control during symmetrical and asymmetrical voltage dips are graphically presented and analyzed in this section. The additional LVRT results were obtained from the DFIG machine test bench at the

smart grid laboratory. In order to understand the power flow during the voltage dips, the negative and positive power shall mean the power delivered and absorbed by the DFIG, respectively.

4.3 Effects of Symmetrical Voltage Dips

The effect of a 100 % three-phase voltage dip on the stator flux is presented in Figure 4.6. It appears that under the total voltage dip the overall stator flux is equal to the natural flux. Here both positive and negative sequence components of the stator voltage are not present (i.e., $\vec{v}_s^+ = 0$ and $\vec{v}_s^- = 0$), and therefore the remaining component is the natural flux that decays with the time constant $\tau_s = R_s/L_s$. This is supported by the Equation 2.7 in Chapter 2.

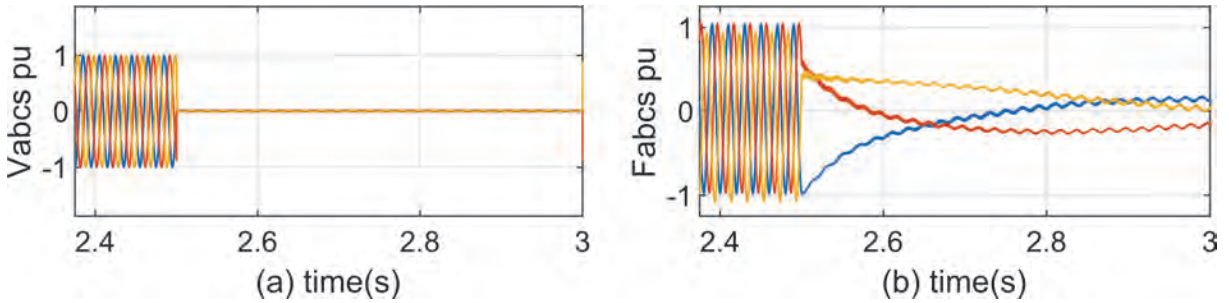


Figure 4.6 Total symmetrical voltage dip without protection. (a) Stator voltage (b) Total stator flux

The effect of a 60 % three-phase voltage dip on the stator flux is presented in Figure 4.7. It appears that the partial voltage dip induces stator flux that is a sum of a sinusoidal and exponential terms. In this case the positive sequence component of the stator voltage is present while the negative sequence is not present (i.e., $\vec{v}_s^+ \neq 0$ and $\vec{v}_s^- = 0$), and therefore the overall flux is the sum of the natural flux which decays with the time constant $\tau_s = R_s/L_s$, and the forced flux due to the

remaining voltage level, which oscillates at the frequency ω_s . This is supported by Equation 2.7 in Chapter 2.

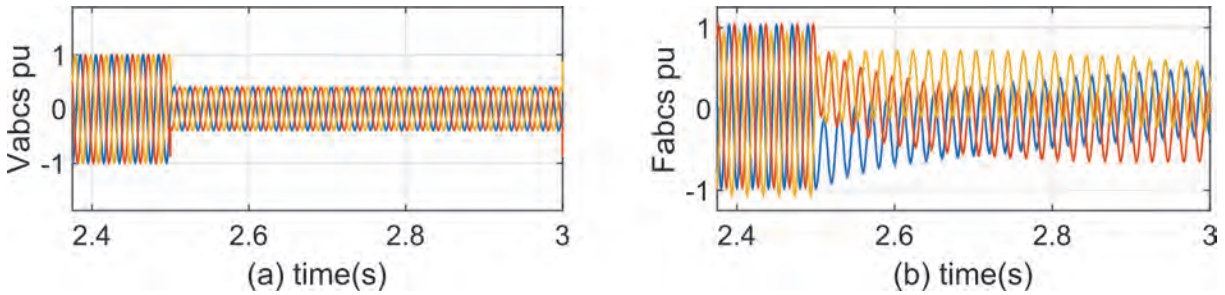


Figure 4.7 Partial (60%) symmetrical voltage dip without protection. (a) Stator voltage
(b) Total stator flux

4.4 Damping of Natural Flux

The effect of a total voltage dip in Figure 4.6 can be mitigated using a crowbar protection scheme proposed in Chapter 2. It can be deduced from Figure 4.8 (b) and (d) that as the crowbar resistance takes all the transient over-current the natural flux decays quickly to its steady-state. This is supported by Equation 2.5.

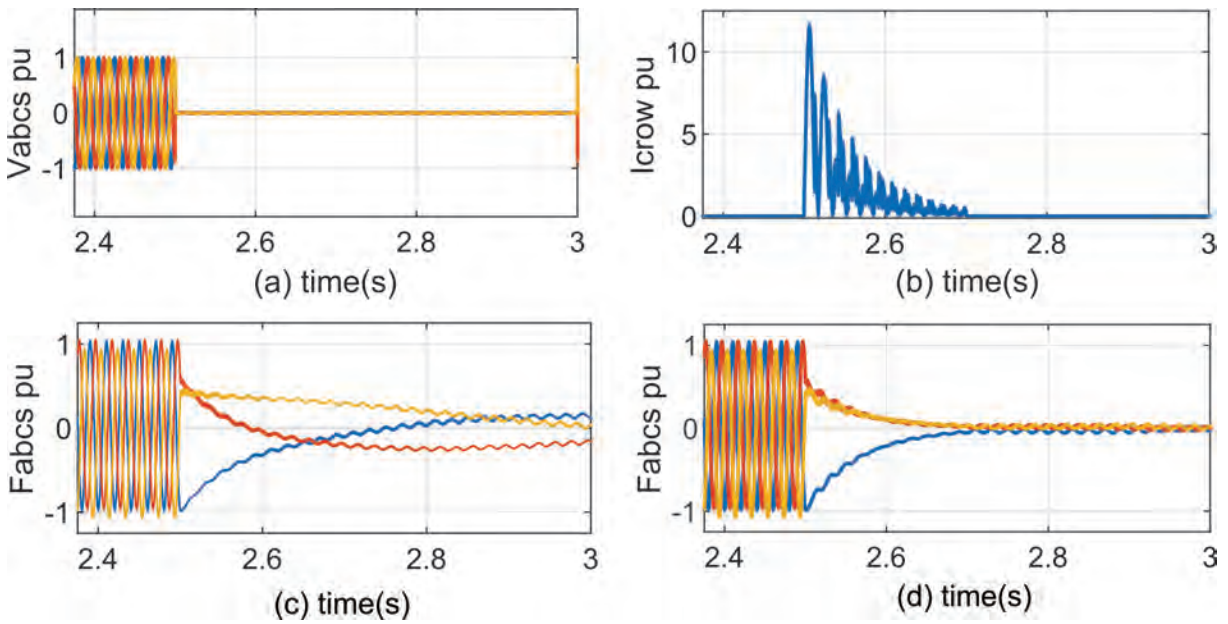


Figure 4.8 Crowbar protection under a total (100 %) symmetrical voltage dip. (a) Stator voltage (b) Crowbar current (c) Total stator flux without protection (d) Total stator flux with crowbar protection

In the case of the partial voltage dip in Figure 4.7 the crowbar protection behaves in a similar way as in Figure 4.8.

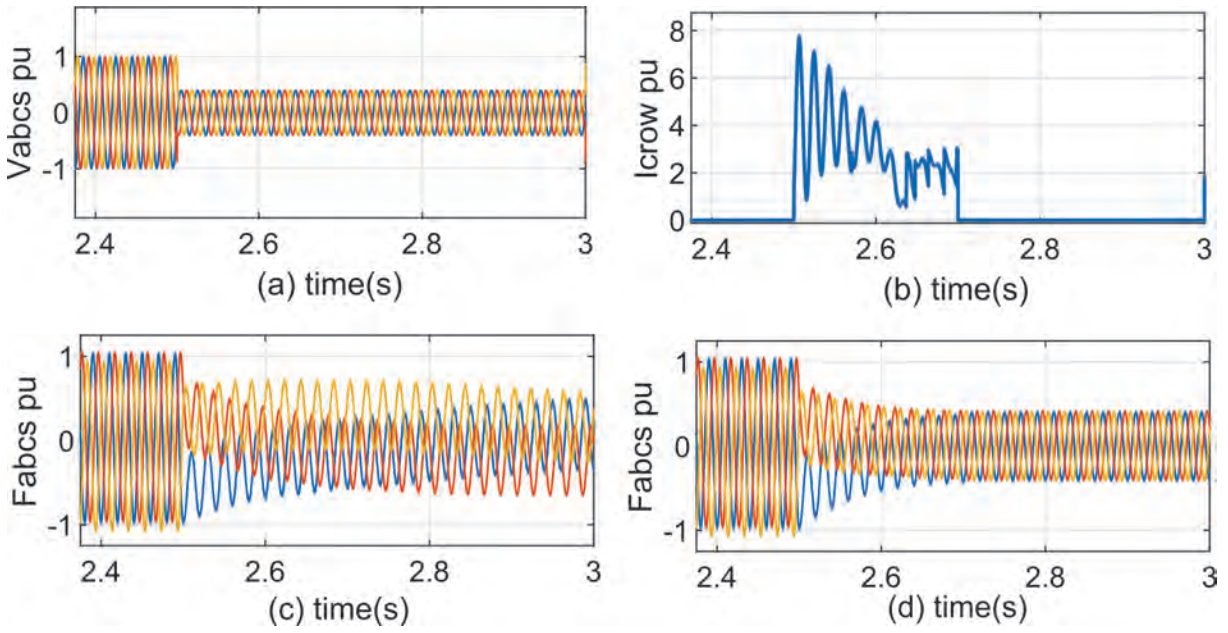


Figure 4.9 Crowbar protection under a partial (60 %) symmetrical voltage dip. (a) Stator voltage (b) Crowbar current (c) Total stator flux without protection (d) Total stator flux with crowbar protection

4.5 Effects of Asymmetrical Voltage Dips

4.5.1 Mitigation Methods

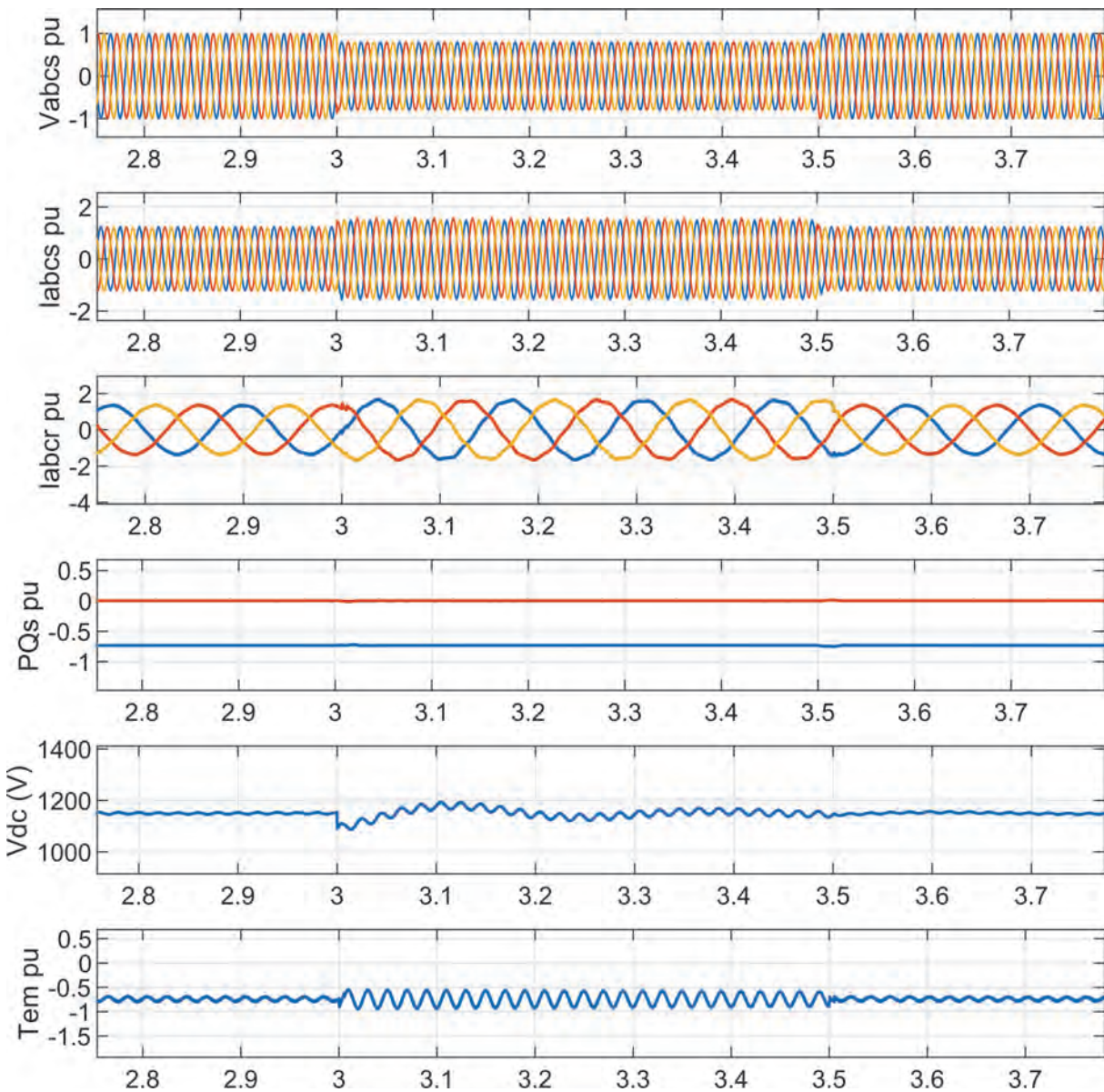


Figure 4.10 DFIG Simulation under 20 % (non-severe) symmetrical voltage dip with traditional vector control

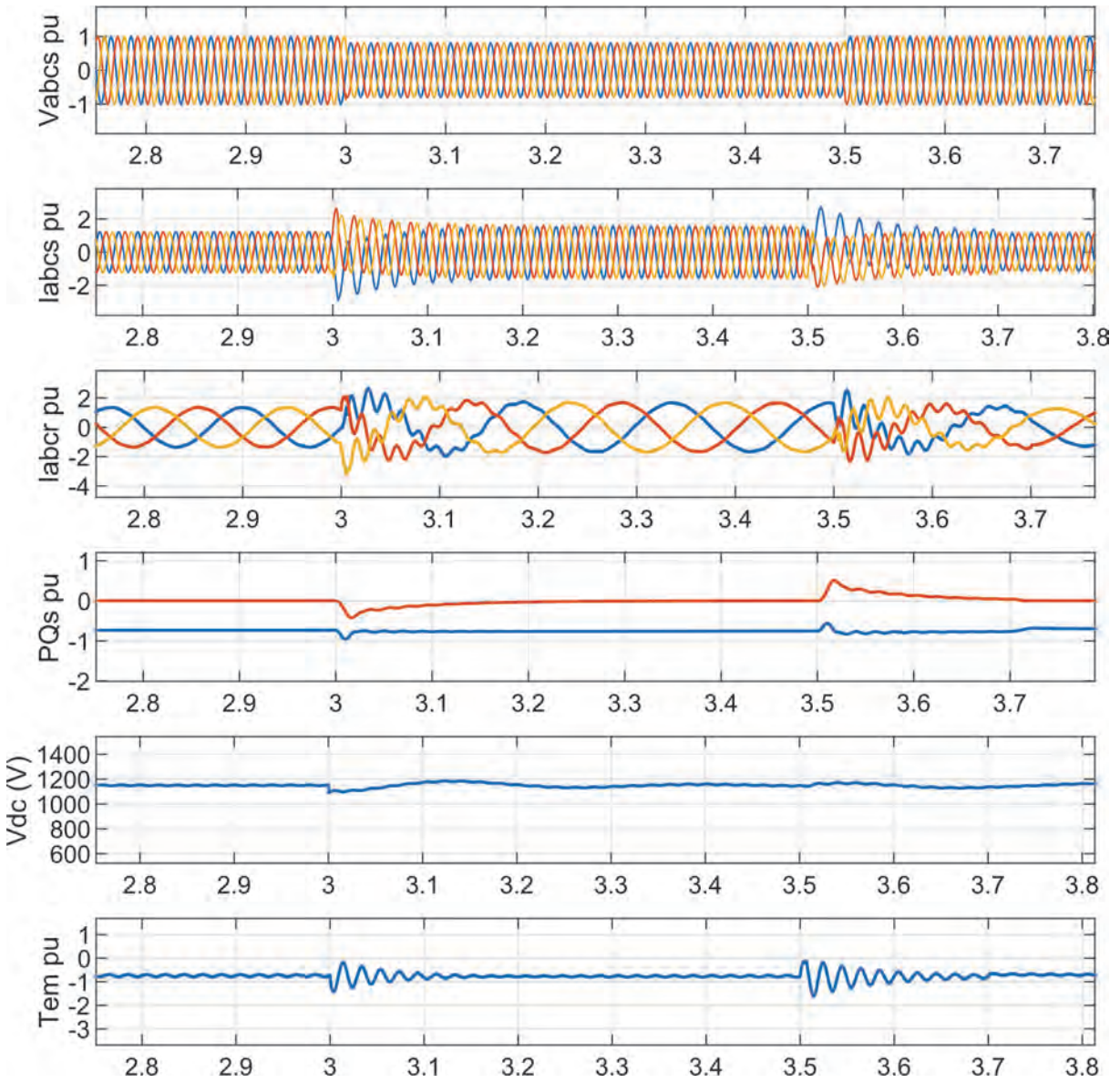


Figure 4.11 DFIG Simulation under 20 % (non-severe) symmetrical voltage dip with demagnetizing current control

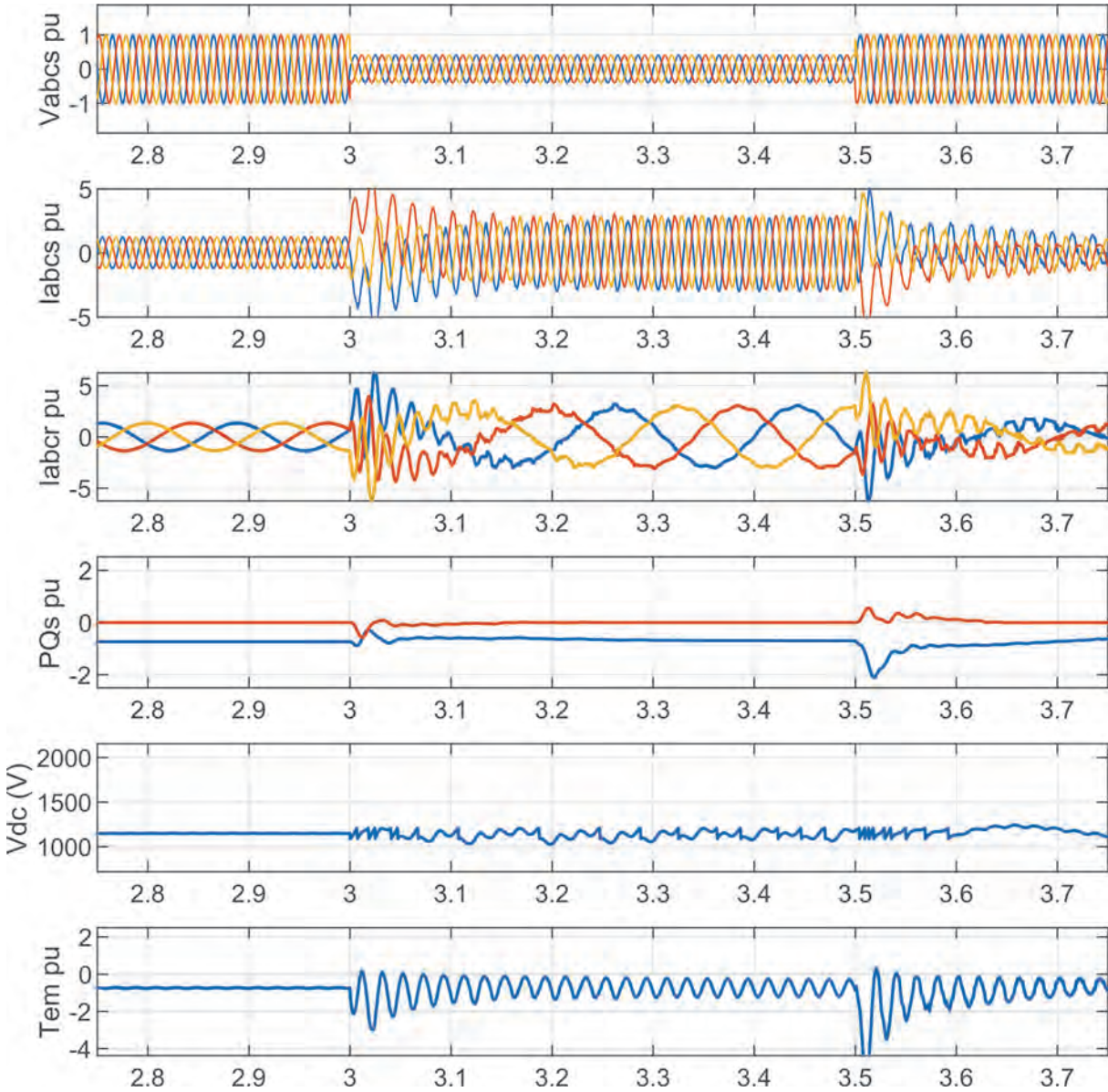


Figure 4.12 DFIG Simulation under 60 % (severe) symmetrical voltage dip with traditional vector control

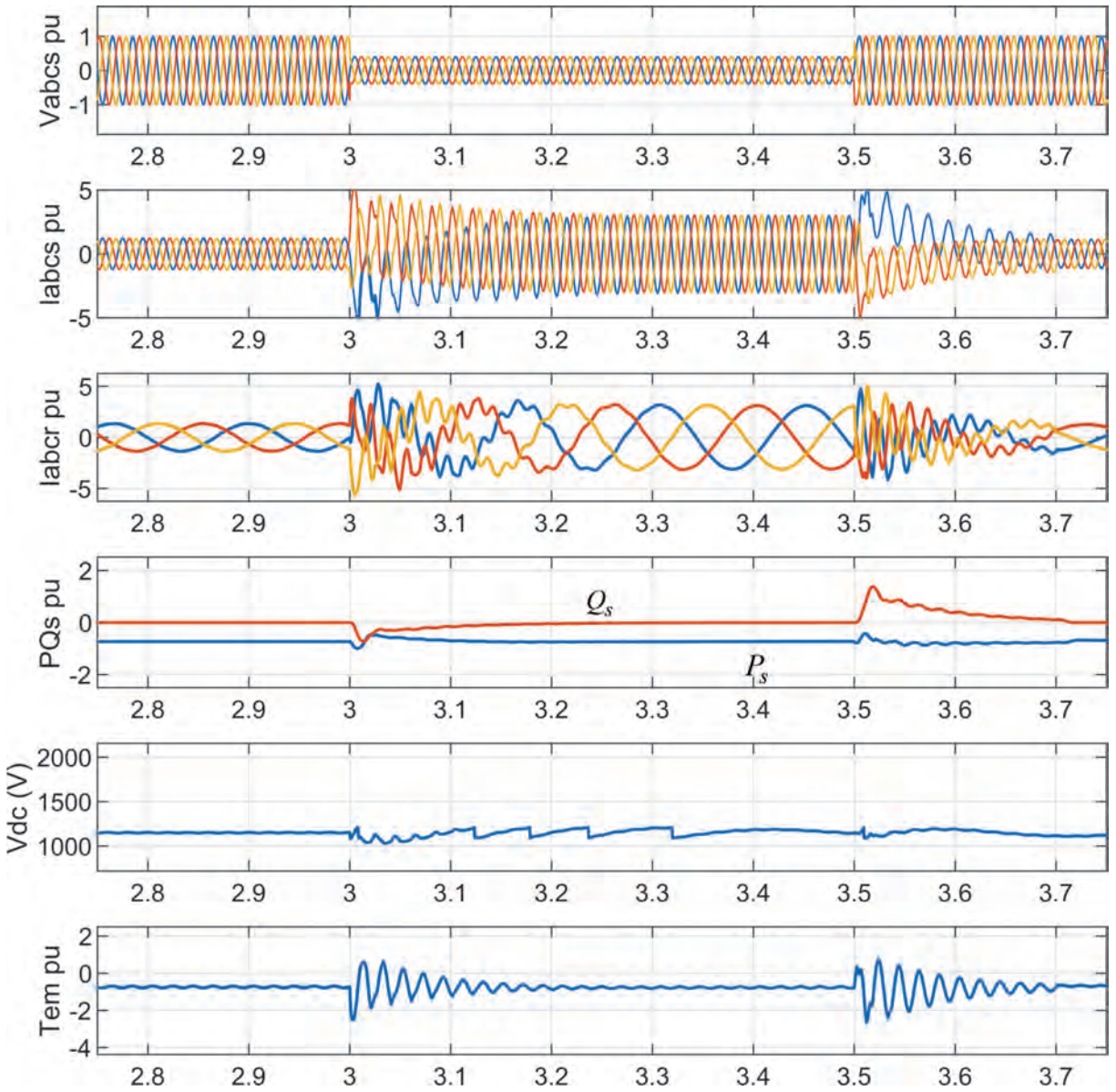


Figure 4.13 DFIG Simulation under 60 % (severe) symmetrical voltage dip with demagnetizing current injection

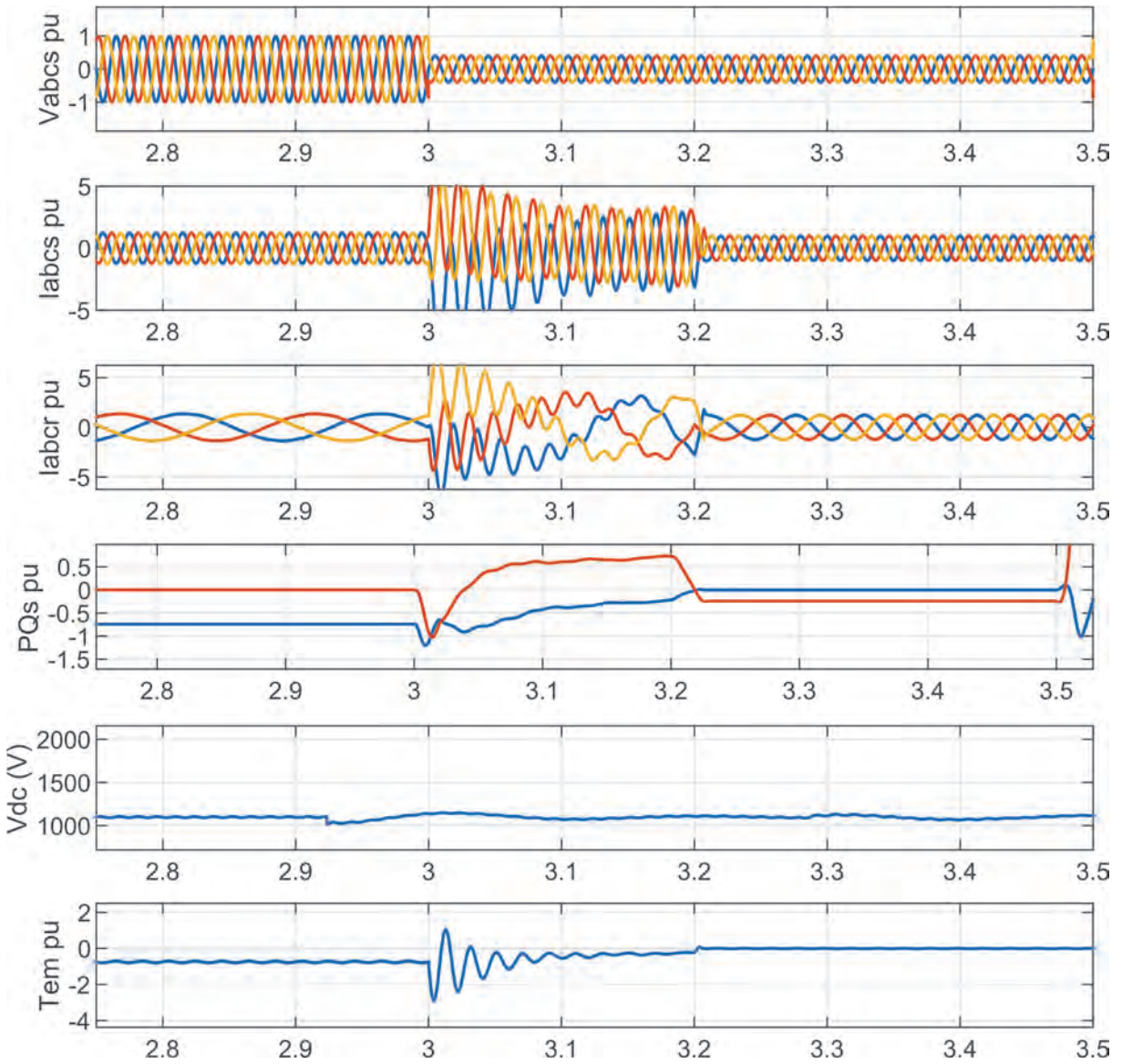


Figure 4.14 DFIG LVRT Simulation under 60 % severe symmetrical voltage dip with Crowbar protection and reactive power control

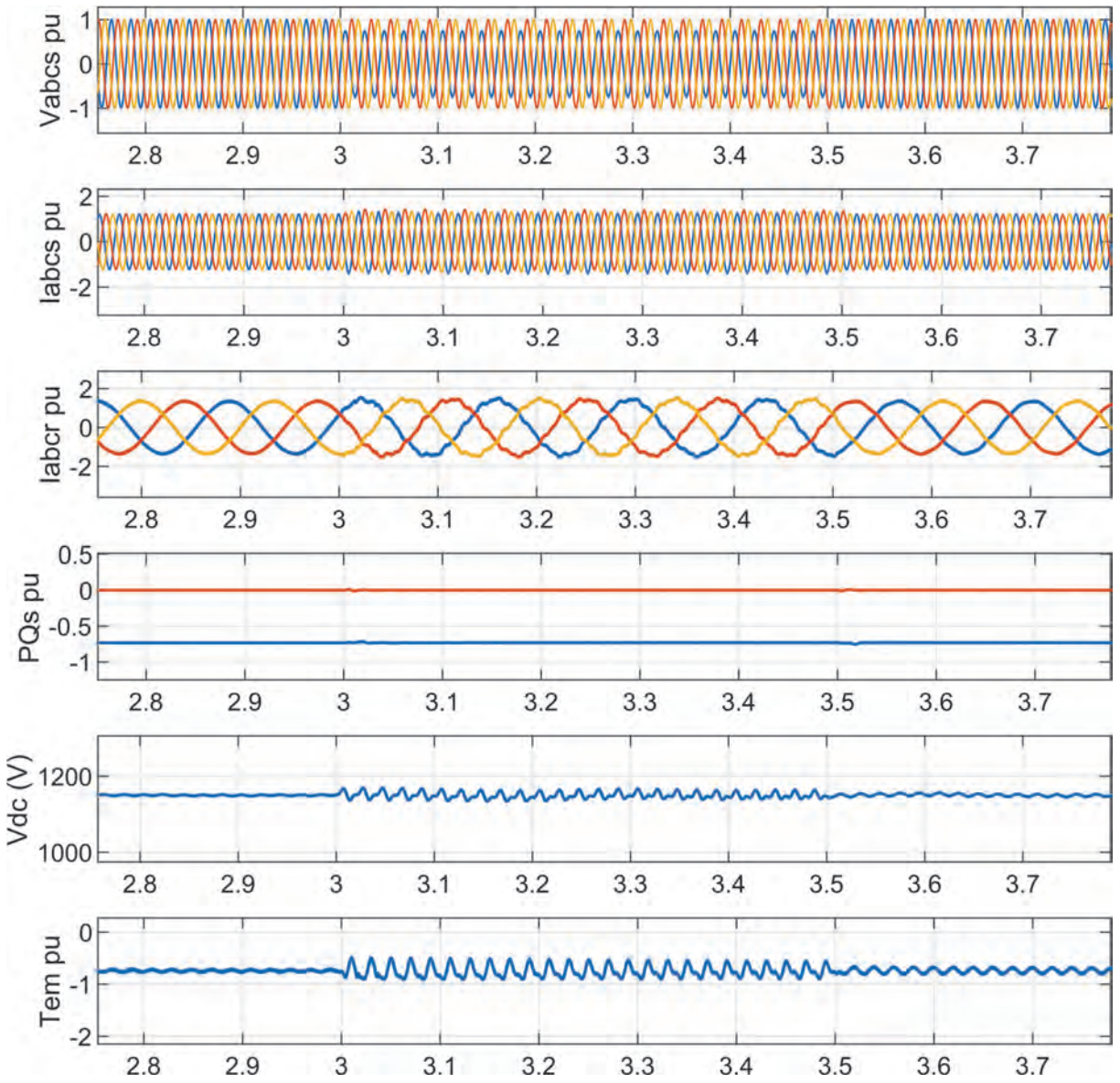


Figure 4.15 DFIG Simulation under 25 % (non-severe) asymmetrical voltage dip with traditional vector control

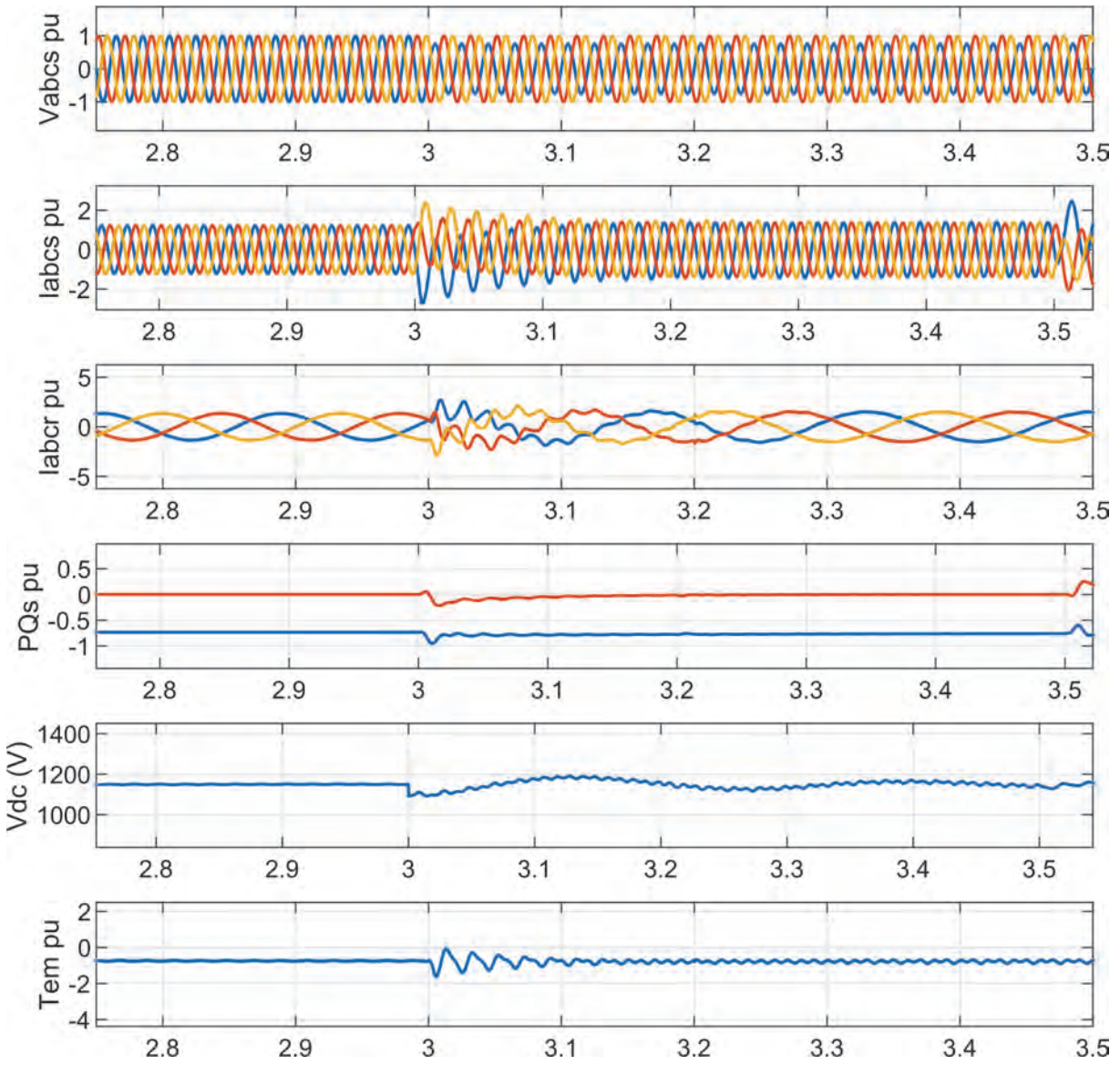


Figure 4.16 DFIG Simulation under 25 % (non-severe) Asymmetrical voltage dip with demagnetizing current control

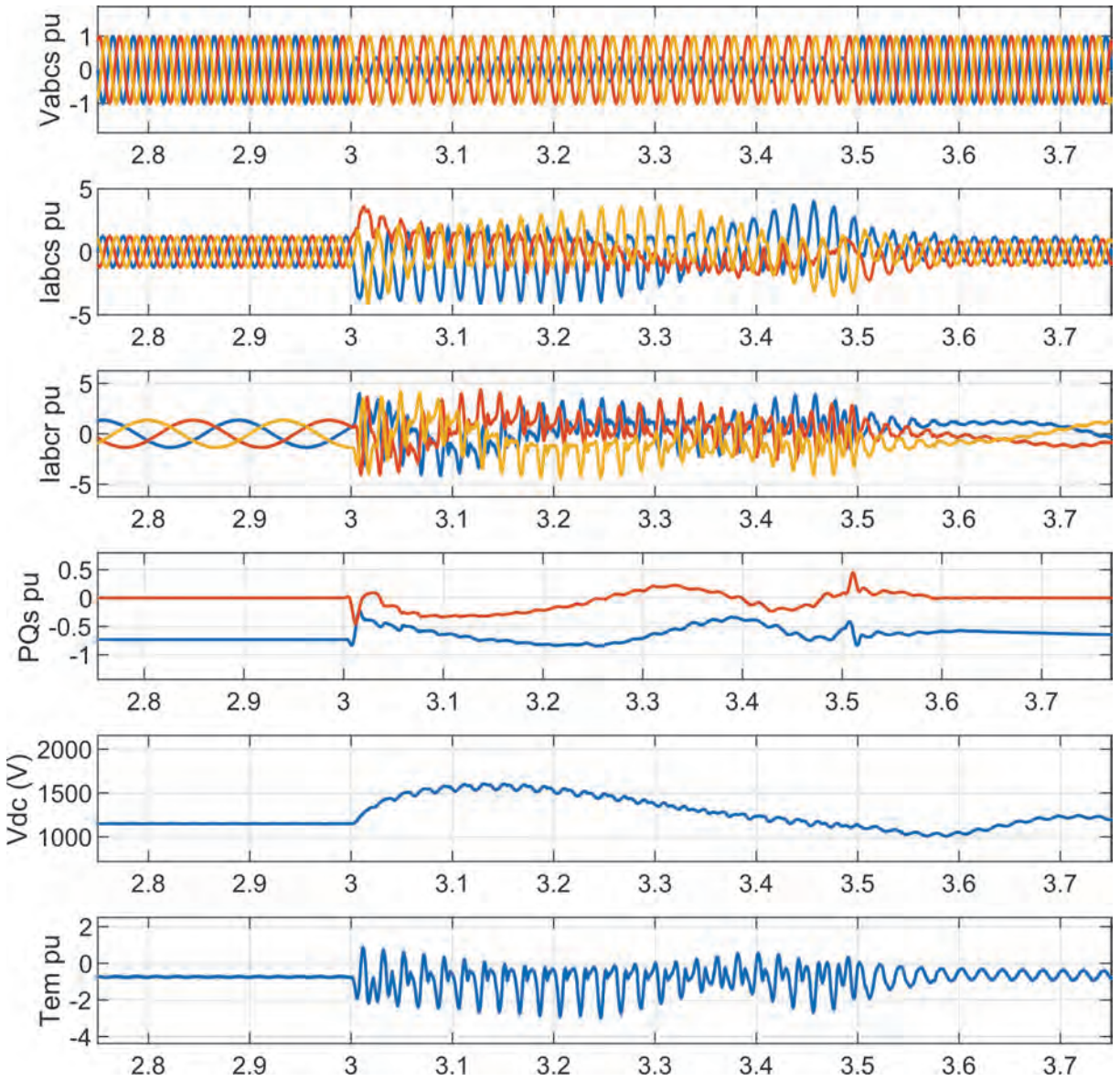


Figure 4.17 DFIG Simulation under 65 % (severe) asymmetrical voltage dip with traditional vector control

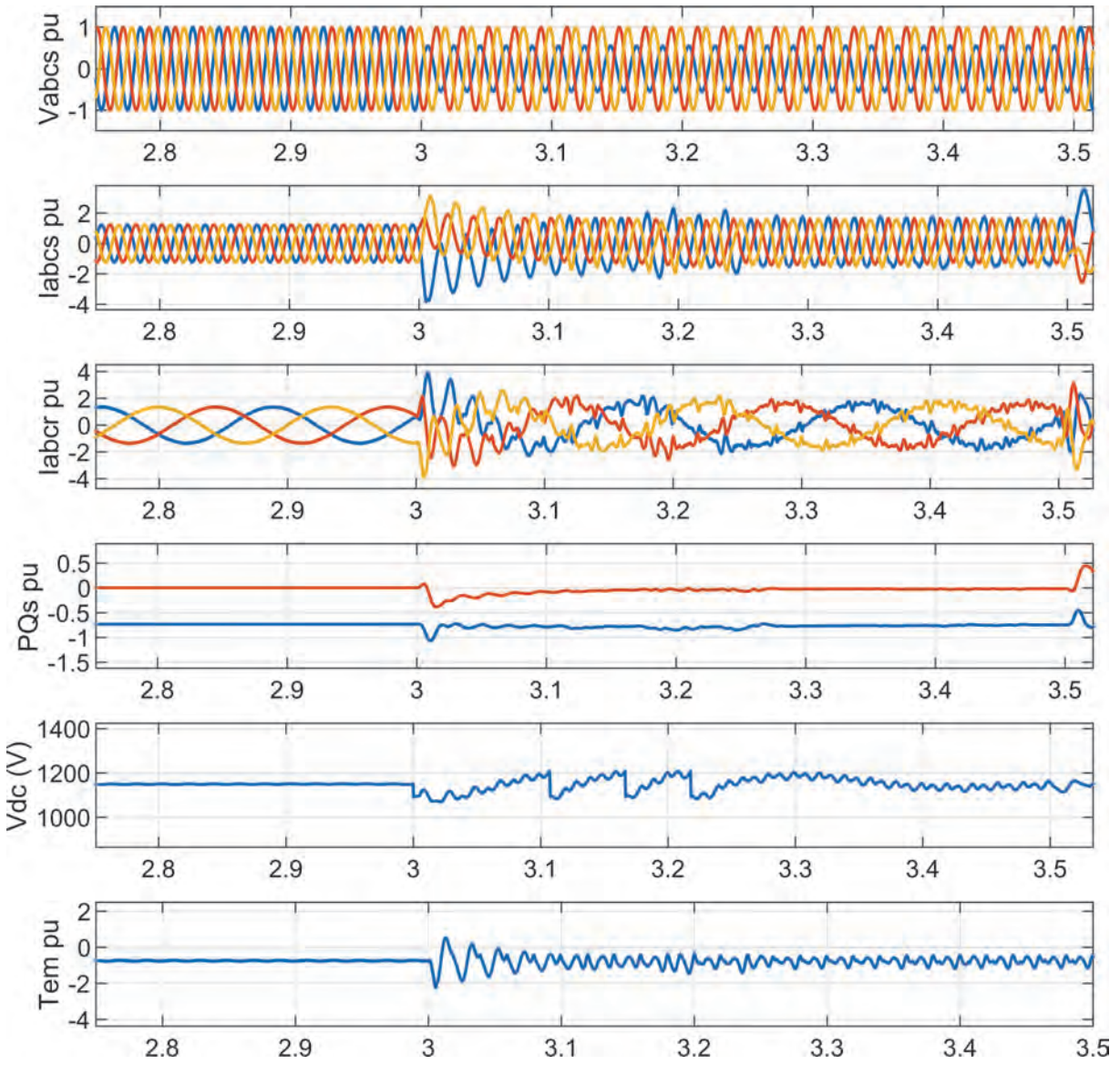


Figure 4.18 DFIG Simulation under 45 % (severe) asymmetrical voltage dip with with demagnetizing current control

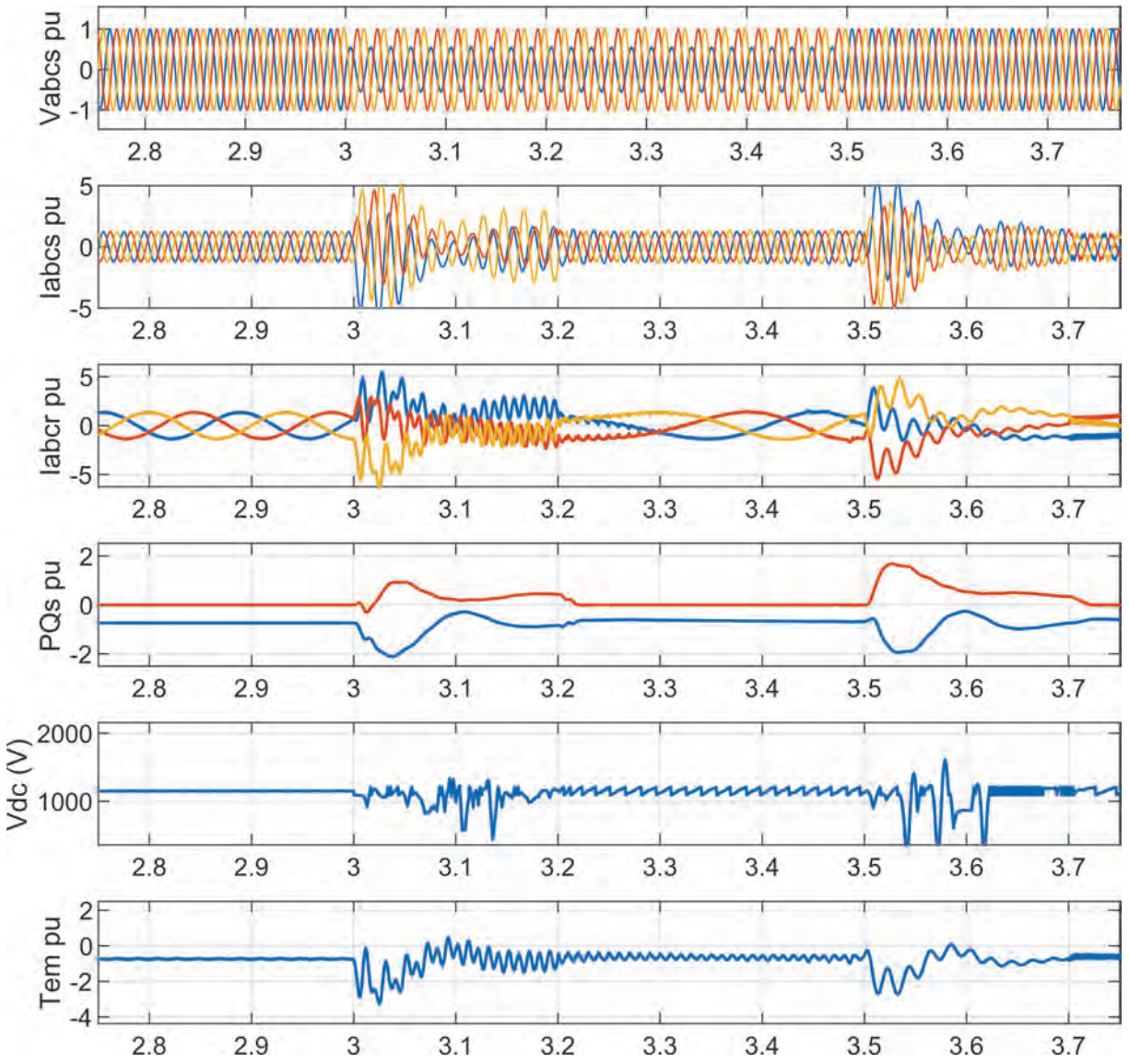


Figure 4.19 DFIG Simulation under 45 % (severe) asymmetrical voltage dip with combined crowbar protection and dual vector control

4.6 Laboratory Experimental Results

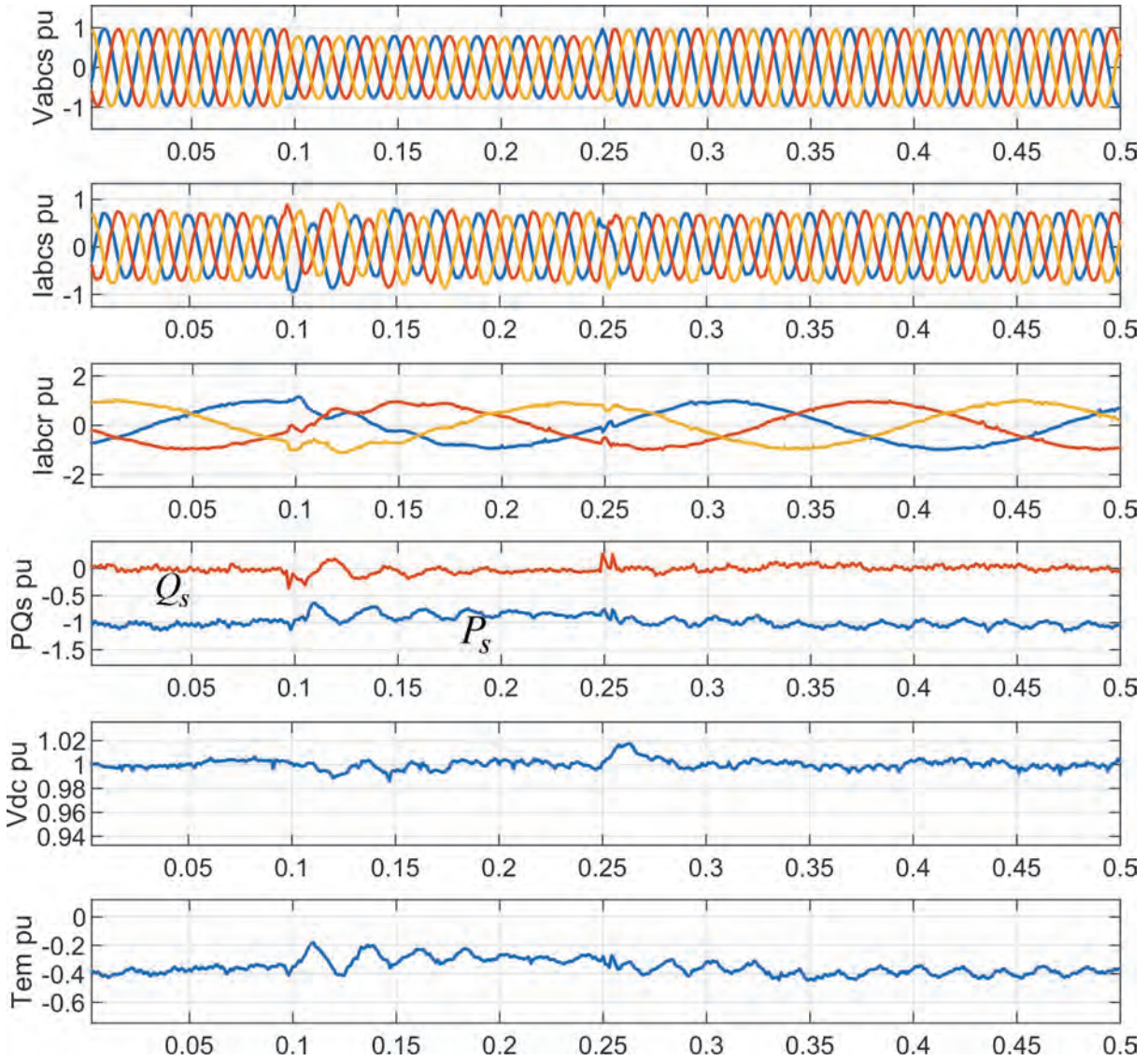


Figure 4.20 Experimental DFIG under 20 % symmetrical voltage dip

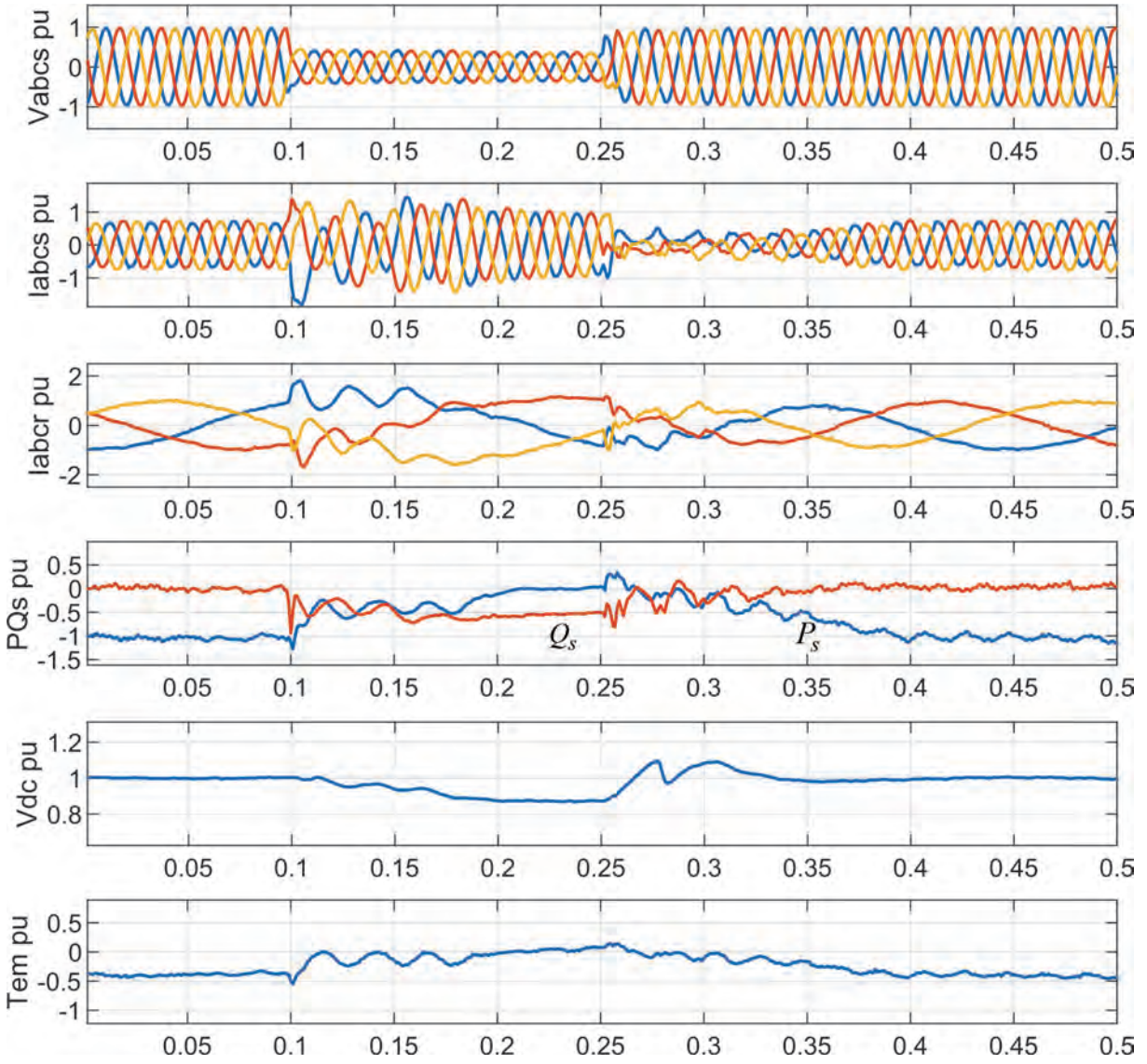


Figure 4.21 Experimental DFIG under 60 % symmetrical voltage dip

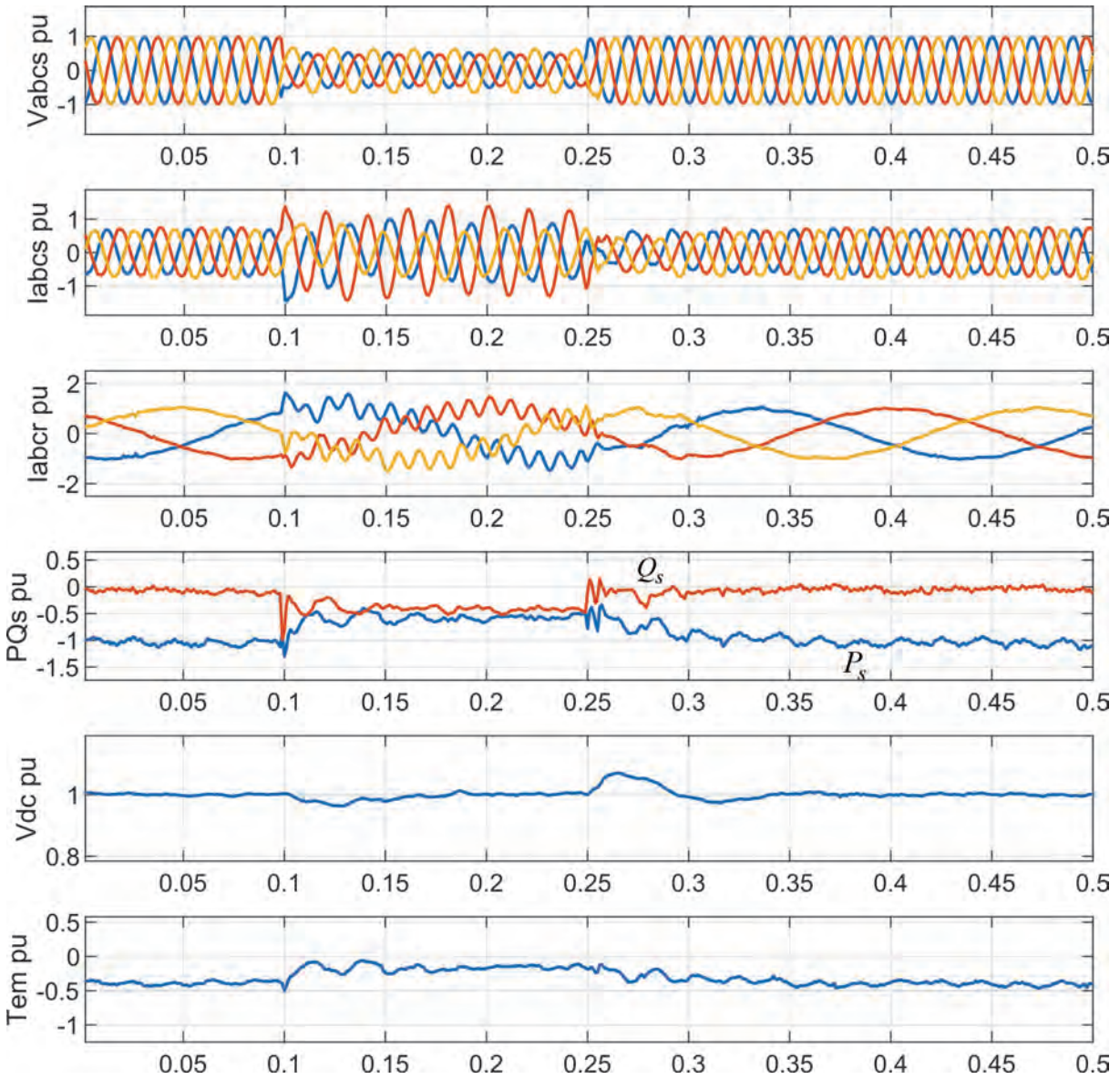


Figure 4.22 Experimental DFIG under 20-60-60 % non-severe Asymmetrical voltage dip

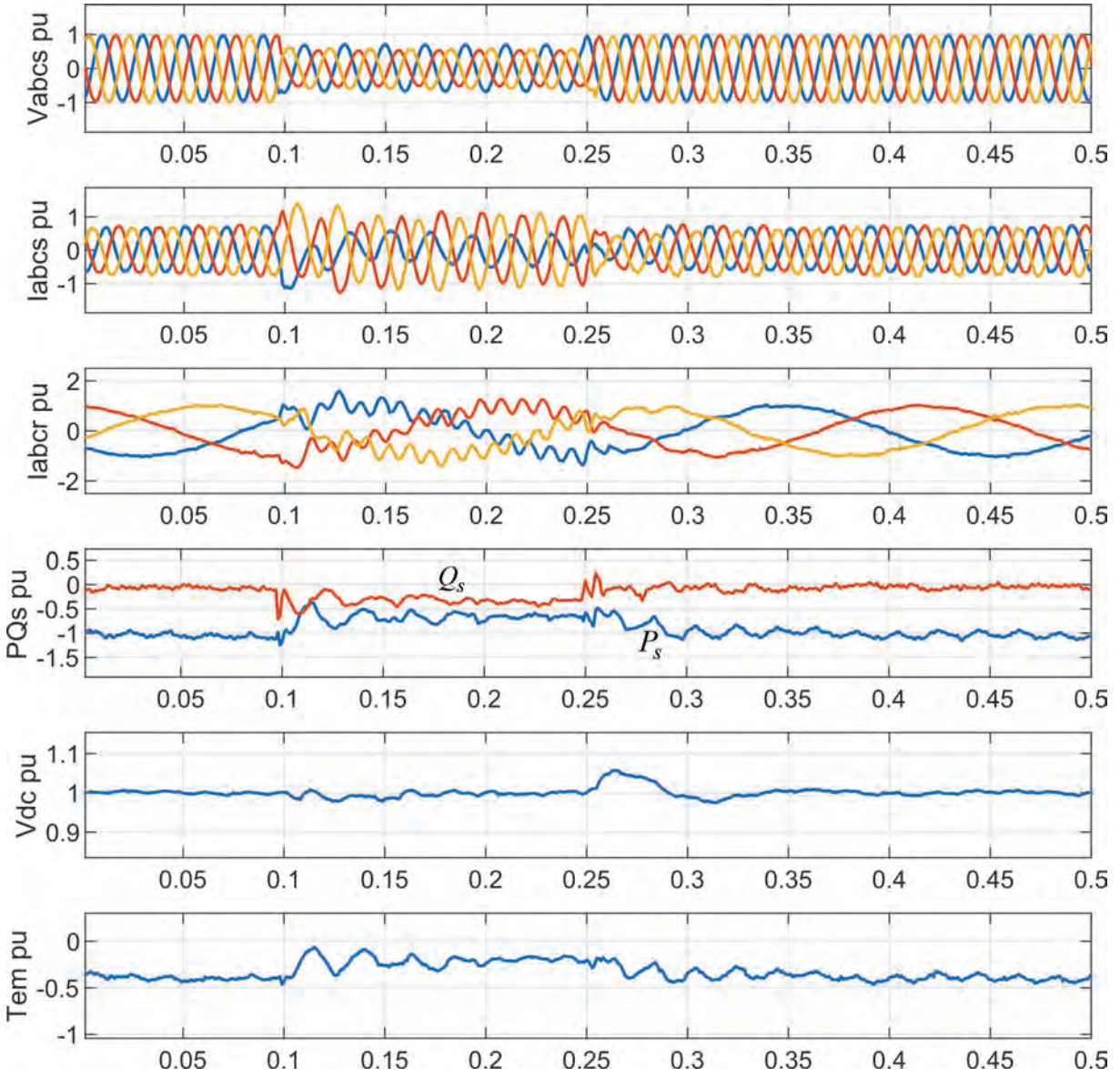


Figure 4.23 Experimental DFIG LVRT under 40-20-60 % severe Asymmetrical voltage dip

4.7 Discussion

It can be deduced that an increased fault severity results in the loss of rotor current control in Figure 4.17. These results are in line with expectations. Under an asymmetrical voltage dip of this magnitude, the combined effects of natural flux and negative sequence result in the saturation of the RSC. Consequently, the PI regulators cannot solely control the rotor currents; in this case, some auxiliary hardware solution of FRT is needed.

The solution to this has been the combined injection of demagnetizing and negative sequence current as seen in Figure 4.18. This method proves to mitigate the impact of both natural and negative sequence fluxes that are induced by the asymmetrical voltage dip. It can be seen that the balanced rotor and stator currents are achieved despite the unbalanced grid voltage.

The results presented in Figure 4.19 were obtained from the incorporation of the crowbar protection system and the dual vector control method. The dual vector control was realized using Equation A.5. It appears that for the 0.2 s of the fault, the crowbar is enabled allowing the stator natural flux of phase A to decay instantly, after that, the dual control technique is engaged in order to balance the stator currents.

Under a 20 % (non-severe) symmetrical voltage dip applied in Figure 4.10 it can be deduced that the fault is so small that the current regulators can still independently control the rotor currents. After the fault clears at 3.5 s, the rotor currents are easily restored. Some slight oscillations can be noticed from the rotor currents and electromagnetic torque. This due to the presence of some undamped natural flux and uncontrolled negative sequence. With the injection of the combined demagnetizing current in Figure 4.11 these oscillations decay quickly.

The results in Figure 4.14 are from the simulation of the crowbar protection scheme together with the series dynamic resistor connected on the stator side. It can be observed that when the fault is applied at 3 s, the transient reactive power is received from the grid. This is due to the activation of the crowbar protection scheme. Then after 3.2 s when the crowbar protection is deactivated the RSC control system is restored; now that the natural flux has been dumped the DFIG supplies the reactive power to the grid as demanded by grid code.

It can be understood from Figure 4.14 that although the incorporation of the crowbar protection scheme infringes the grid code for some few milliseconds, it can effectively accelerate the decay of the natural flux during that period, and therefore making it possible to control rotor currents through the RSC after it has been deactivated.

To analyze the fault ride-through capability of the machine test bench, the severe symmetrical voltage dip of 60 % was applied as shown in Figure 4.21. The South African grid connection code presented in Figure D.4 prohibits the connection of a DFIG if the voltage magnitude falls below 0.6 pu [14]; the machine test stand protection system will isolate the DFIG unit in the occurrence of any voltage dips above 0.6 pu. It for this reason that the author could not go beyond 60 % in the machine test stand.

In Figure 4.20 the symmetrical voltage dip was applied between 0.1 s and 0.25 s; while the machine is running at 1360 rpm the DFIG can deliver reactive power to the grid as demanded by the grid code even though the fault can be categorised as a severe voltage dip.

Chapter 5

Conclusion and Recommendations for Further Studies

5.1 Conclusion

The preliminary research goal was to examine the effects of symmetrical and asymmetrical voltage dips in a DFIG WECS. The findings suggest that with the traditional vector control system, the rotor side converter (RSC) can independently ride-through the non-severe voltage dips (of $< 30\%$ in depth). However, it appears that under severe voltage dips (of $>30\%$ in depth) the RSC cannot be solely controlled through traditional vector control method.

As aforementioned in the limitations section, the limits of the machines tests bench could not be exceeded to match the simulation results. Also, the machine test stand incorporates protection features which caused it to behave differently. Although the measured results could not cover all

the cases in the simulation environment, some correlation can be noticed, particularly in terms of the effects of fault type, severity and low voltage ride-through capability. Overall, the experimental results assisted the author in verifying simulation.

To answer the main questions about the mitigation of effects of symmetrical and asymmetrical grid voltage dips, the study has been successfully carried out in Chapter 4 whereby the effects of the voltage dips were considered. By using the signal delay cancellation method, the sequence components of the grid voltage were efficiently extracted and used in the calculation of references for the dual vector control method.

The findings of this research have validated the hypothesis that the crowbar protection scheme cannot be used without violating the grid code for a few seconds of the fault duration. The combined control of natural and negative flux is found to be effective in achieving balanced rotor and stator currents during asymmetrical voltage dips when compared to the dual vector control. However, it has been deduced that this strategy is not suitable for reactive power control during a voltage dip but it is good for the safety of the power electronic converter.

5.2 Recommendations for Further Studies

It has been verified by this research that the effects of grid voltage dips in the operation of WECS cannot be adequately mitigated through available control and hardware strategies. Integration of renewable energy power plants with the nationally integrated power system is still a challenging subject due to the lack of inherent synchronous inertia that wind farms exhibit. The contemporary WECS discussed in this thesis are connected to the grid via power electronic converters, and they

are therefore not a directly mechanically-coupled rotating mass as a conventional synchronous generator. Future research should look closely at solutions of the inertia aspect of WECS.

Bibliography

- [1] S Sewchurran and I.E Davidson. “Introduction to the South African Renewable Energy Grid Code Version 2.9 Requirements - Part (I) Introduction”. In: *IEEE Africon 2017 Proc* (2017), pp. 1220–1224.
- [2] V Yaramasu and B Wu. *Model Predictive Control of Wind Energy Conversion Systems*. IEEE Series on Power Engineering. New Jersey, Canada: John Wiley & Sons, 2017.
- [3] H Abu-Rub, M Malinowski, and K Al-Haddad, eds. *Power Electronics for Renewable Energy Systems, Transportation and Industrial Applications*. New Jersey, Canada: John Wiley & Sons, 2014.
- [4] Department of Energy. *State of Renewable Energy in South Africa*. Tech. rep. Pretoria, South Africa: Department of Energy, Sept. 2015.
- [5] A Eberhard and R Naude. *The South African Renewable Energy IPP Procurement Programme*. Tech. rep. Graduate School of Business, University of Cape Town, 2017, pp. 1–80.
- [6] S Sewchurran and I.E Davidson. “Introduction to the South African Renewable Energy Grid Code Version 2.9 Requirements - Part (III) Discussions and Conclusions”. In: *IEEE Africon 2017 Proc* (2017), pp. 1231–1234.

- [7] M Stiebler. *Wind Energy Systems for Electric Power Generation*. Springer series in Green Energy and Technology. New York: Springer, 2008.
- [8] T Burton, D Sharpe, N Jenkins, and E Bossanyi. *Wind Energy Handbook*. New York: John Wiley & Sons, 2001.
- [9] G Abad, J Lopez, M.A Rodriguez, L Marroyo, and G Lwanski. *Doubly Fed Induction Machine: Modelling and Control for Wind Energy Generation*. IEEE Series on Power Engineering. New Jersey, Canada: John Wiley & Sons, 2011.
- [10] P.M.J Roque and S.P.D Chowdhury. “Expansion of Wind Power Technology in South Africa: Challenges and Opportunities”. In: *2017 IEEE PES-IAS PowerAfrica (2017)*, pp. 560–565.
- [11] A Abdelbaset, Y.S Mohamed, A.M El-Sayed, and A.E.H Ahmed. *Wind Driven Doubly-fed Induction Generator: Grid Synchronization and Control*. Power Systems. Gewerbestrase, Switzerland: Springer, 2018.
- [12] D Xu, F Blaabjerg, W Chen, and N Zhu. *Advanced Control of Doubly Fed Induction Generator for Wind Power Systems*. IEEE Series on Power Engineering. New Jersey, Canada: John Wiley & Sons, 2018.
- [13] O Anaya-Lara, D Campos-Gaona, E Moreno-Goytia, and G Adam. *Offshore Wind Energy Generation: Control, Protection, and Integration to Electrical Systems*. West Sussex, United Kingdom: John Wiley & Sons, 2014.
- [14] *Grid Connection Code for Renewable Power Plants (RPPs) Connected to the Electricity Transmission System (TS) or the Distribution System (DS) in South Africa*. Version 2.9. NERSA. July 2016.
- [15] B Wu, Y Lang, N Zargari, and S Kouro. *Power Conversion and Control of Wind Energy Systems*. IEEE Series on Power Engineering. New Jersey, Canada: John Wiley & Sons, 2011.

-
- [16] I. Erlich and U. Bachmann. “Grid code requirements concerning connection and operation of wind turbines in Germany”. In: *IEEE Power Engineering Society General Meeting, 2005*. June 2005, 1253–1257 Vol. 2. DOI: [10.1109/PES.2005.1489534](https://doi.org/10.1109/PES.2005.1489534).
- [17] C. Feltes, S. Engelhardt, J. Kretschmann, J. Fortmann, and I. Erlich. “Dynamic performance evaluation of DFIG-based wind turbines regarding new German grid code requirements”. In: *IEEE PES General Meeting*. July 2010, pp. 1–7. DOI: [10.1109/PES.2010.5589562](https://doi.org/10.1109/PES.2010.5589562).
- [18] L. Yang, Z. Xu, J. Ostergaard, Z. Y. Dong, and K. P. Wong. “Advanced Control Strategy of DFIG Wind Turbines for Power System Fault Ride Through”. In: *IEEE Transactions on Power Systems* 27.2 (May 2012), pp. 713–722. DOI: [10.1109/TPWRS.2011.2174387](https://doi.org/10.1109/TPWRS.2011.2174387).
- [19] J. Yang, D. G. Dorrell, and J. E. Fletcher. “Fault ride-through of doubly-fed induction generator with converter protection schemes”. In: *2008 IEEE International Conference on Sustainable Energy Technologies*. Nov. 2008, pp. 1211–1216. DOI: [10.1109/ICSET.2008.4747191](https://doi.org/10.1109/ICSET.2008.4747191).
- [20] J. Zhai and H. Liu. “Reactive power control strategy of DFIG wind farms for regulating voltage of power grid”. In: *2014 IEEE PES General Meeting | Conference Exposition*. July 2014, pp. 1–5. DOI: [10.1109/PESGM.2014.6939441](https://doi.org/10.1109/PESGM.2014.6939441).
- [21] G. Gontijo, T. Tricarico, D. Krejci, B. França, and M. Aredes. “A novel stator voltage distortion and unbalance compensation of a DFIG with series grid side converter using adaptive resonant controllers”. In: *2017 Brazilian Power Electronics Conference (COBEP)*. Nov. 2017, pp. 1–6. DOI: [10.1109/COBEP.2017.8257280](https://doi.org/10.1109/COBEP.2017.8257280).
- [22] Y. Zhou, P. Bauer, J. A. Ferreira, and J. Pierik. “Operation of Grid-Connected DFIG Under Unbalanced Grid Voltage Condition”. In: *IEEE Transactions on Energy Conversion* 24.1 (Mar. 2009), pp. 240–246. ISSN: 1558-0059. DOI: [10.1109/TEC.2008.2011833](https://doi.org/10.1109/TEC.2008.2011833).

- [23] J. Hu, J. Zhu, and D. G. Dorrell. “Predictive Direct Power Control of Doubly Fed Induction Generators Under Unbalanced Grid Voltage Conditions for Power Quality Improvement”. In: *IEEE Transactions on Sustainable Energy* 6.3 (July 2015), pp. 943–950. ISSN: 1949-3029. DOI: [10.1109/TSTE.2014.2341244](https://doi.org/10.1109/TSTE.2014.2341244).
- [24] T Orowska-Kowalska, F Blaabjerg, and J Rodríguez. *Advanced and Intelligent Control in Power Electronics and Drives*. New York: Springer, 2014.
- [25] I. Villanueva, A. Rosales, P. Ponce, and A. Molina. “Grid-Voltage-Oriented Sliding Mode Control for DFIG Under Balanced and Unbalanced Grid Faults”. In: *IEEE Transactions on Sustainable Energy* 9.3 (July 2018), pp. 1090–1098. ISSN: 1949-3037. DOI: [10.1109/TSTE.2017.2769062](https://doi.org/10.1109/TSTE.2017.2769062).
- [26] J. Lopez, P. Sanchis, E. Gubia, A. Ursua, L. Marroyo, and X. Roboam. “Control of Doubly Fed Induction Generator under symmetrical voltage dips”. In: *2008 IEEE International Symposium on Industrial Electronics*. June 2008, pp. 2456–2462. DOI: [10.1109/ISIE.2008.4677148](https://doi.org/10.1109/ISIE.2008.4677148).
- [27] L. Xu and Y. Wang. “Dynamic Modeling and Control of DFIG-Based Wind Turbines Under Unbalanced Network Conditions”. In: *IEEE Transactions on Power Systems* 22.1 (Feb. 2007), pp. 314–323. ISSN: 0885-8950. DOI: [10.1109/TPWRS.2006.889113](https://doi.org/10.1109/TPWRS.2006.889113).
- [28] J. C. Das. “Symmetrical Components Using Matrix Methods”. In: *Understanding Symmetrical Components for Power System Modeling*. IEEE, 2017, pp. 1–14. ISBN: null. DOI: [10.1002/9781119226895.ch1](https://doi.org/10.1002/9781119226895.ch1). URL: <https://ieeexplore.ieee.org/document/7827518>.
- [29] J. Yang, J. E. Fletcher, and J. O'Reilly. “A Series-Dynamic-Resistor-Based Converter Protection Scheme for Doubly-Fed Induction Generator During Various Fault Conditions”. In: *IEEE Transactions on Energy Conversion* 25.2 (June 2010), pp. 422–432. ISSN: 1558-0059. DOI: [10.1109/TEC.2009.2037970](https://doi.org/10.1109/TEC.2009.2037970).

-
- [30] P Krause, O Wasynczuk, S Sudhoff, and S Pekarek. *Analysis of Electric Machinery and Drive Systems*. IEEE Series on Power Engineering. New Jersey, Canada: John Wiley & Sons, 2013.
- [31] T Wildi. *Electrical Machines, Drives, and Power Systems: Fifth Edition*. New Jersey: Prentice Hall, 2002.
- [32] A. A. Salah and D. G. Dorrell. “Operating Induction Machine in DFIG Mode Including Rotor Asymmetry”. In: *2019 Southern African Universities Power Engineering Conference/Robotics and Mechatronics/Pattern Recognition Association of South Africa (SAUPEC/RoboMech/PRASA)*. Jan. 2019, pp. 469–474. DOI: [10.1109/RoboMech.2019.8704826](https://doi.org/10.1109/RoboMech.2019.8704826).
- [33] H Abu-Rub, A Iqbal, and J Guzinski. *High Performance Control of AC Drive with MATLAB/Simulink*. West Sussex, United Kingdom: John Wiley & Sons, 2012.
- [34] L. Riachy, Y. Azzouz, and B. Dakyo. “Optimal power coefficient for load balancing and reactive power compensation In DFIG-WTS”. In: *IECON 2016 - 42nd Annual Conference of the IEEE Industrial Electronics Society*. Oct. 2016, pp. 4199–4204. DOI: [10.1109/IECON.2016.7793843](https://doi.org/10.1109/IECON.2016.7793843).

Appendix A

Formulae

A.1 Constants

Sigma

$$\sigma = 1 - \frac{L_m^2}{L_s L_r} \quad (\text{A.1})$$

Rotor and stator time constants

$$\tau_s = \frac{L_s}{R_s} \quad \tau_r = \frac{L_r}{R_r} \quad (\text{A.2})$$

Rotor and stator constants

$$k_r = \frac{L_m}{L_r} \quad k_s = \frac{L_m}{L_s} \quad (\text{A.3})$$

A.2 Control targets for the RSC under unbalanced grid voltage

Target 1: Constant stator power

$$\begin{bmatrix} i_{dr1} \\ i_{qr1} \\ i_{dr2} \\ i_{qr2} \end{bmatrix} = -\frac{2 L_s P_{s0}}{3 L_m D} \begin{bmatrix} v_{ds1} \\ v_{qs1} \\ -v_{ds2} \\ -v_{qs2} \end{bmatrix} - \frac{2 L_s Q_{s0}}{3 L_m R} \begin{bmatrix} v_{qs1} \\ -v_{ds1} \\ -v_{qs2} \\ v_{ds2} \end{bmatrix} + \frac{1}{\omega_s L_m} \begin{bmatrix} v_{qs1} \\ -v_{ds1} \\ -v_{qs2} \\ v_{ds2} \end{bmatrix} \quad (\text{A.4})$$

Target 2: Balanced stator current

$$\begin{bmatrix} i_{dr1} \\ i_{qr1} \\ i_{dr2} \\ i_{qr2} \end{bmatrix} = -\frac{2 L_s}{3 L_m D + R} \begin{bmatrix} v_{ds1} & v_{qs1} \\ v_{qs1} & -v_{ds1} \\ 0 & 0 \\ 0 & 0 \end{bmatrix} \begin{bmatrix} P_{s0} \\ Q_{s0} \end{bmatrix} + \frac{1}{\omega_s L_m} \begin{bmatrix} v_{qs1} \\ -v_{ds1} \\ -v_{qs2} \\ v_{ds2} \end{bmatrix} \quad (\text{A.5})$$

Target 3: Constant electromagnetic torque

$$\begin{bmatrix} i_{dr1} \\ i_{qr1} \\ i_{dr2} \\ i_{qr2} \end{bmatrix} = -\frac{2 L_s P_m 0 \omega_s}{3 L_m D \omega} \begin{bmatrix} v_{ds1} \\ v_{qs1} \\ v_{ds2} \\ v_{qs2} \end{bmatrix} + \left(\frac{2 L_s Q_{s0}}{3 L_m R} + \frac{1}{\omega_s L_m} \right) \begin{bmatrix} v_{qs1} \\ -v_{ds1} \\ -v_{qs2} \\ v_{ds2} \end{bmatrix} \quad (\text{A.6})$$

Target 4: Balanced rotor current

$$\begin{bmatrix} i_{dr1} \\ i_{qr1} \\ i_{dr2} \\ i_{qr2} \end{bmatrix} = -\frac{2 L_s}{3 L_m} \frac{2}{D+R} \begin{bmatrix} v_{ds1} & v_{qs1} \\ v_{qs1} & -v_{ds1} \\ 0 & 0 \\ 0 & 0 \end{bmatrix} \begin{bmatrix} P_{s0} \\ Q_{s0} \end{bmatrix} + \frac{1}{\omega_s L_m} \begin{bmatrix} v_{qs1} \\ -v_{ds1} \\ 0 \\ 0 \end{bmatrix} + \frac{1}{\omega_s \sigma L_r} \frac{L_m}{L_s} \begin{bmatrix} 0 \\ 0 \\ v_{qs2} \\ -v_{ds2} \end{bmatrix} \quad (\text{A.7})$$

Appendix B

Parameters and Variables

B.1 DFIG parameters

| Parameter | Value | Units | Description |
|------------|-------|---------------------|--|
| P_s | 2 | MW | DFIG rated power |
| $V_{s,ll}$ | 690 | V | Rated stator voltage |
| $I_{s,ll}$ | 1760 | A | Rated stator current |
| f_s | 50 | Hz | Grid/Stator frequency |
| R_s | 2.6 | m Ω | Stator resistance |
| R'_r | 2.9 | m Ω | Stator referred rotor resistance |
| L_{1s} | 0.087 | mH | Stator leakage inductance |
| L'_{1r} | 0.087 | mH | Stator referred rotor leakage inductance |
| L_m | 2.5 | mH | Magnetizing inductance |
| N_{sr} | 1/3 | pu | Stator-to-rotor turns ratio |
| p | 2 | — | Number of pole pairs |
| J | 127 | kg · m ² | Inertia constant |
| D | 0.001 | — | Damping ratio |

Table B.1 DFIG parameters for MATLAB/Simulink[®] simulation [34]

| Parameter | Value | Units | Description |
|-----------|-------|---------------|---------------------|
| R_g | 20 | $\mu\Omega$ | Filter resistance |
| L_g | 200 | μH | Filter inductance |
| V_{bus} | 1150 | V | DC bus voltage |
| C_{bus} | 80 | mF | DC bus capacitance |
| f_{sw} | 4 | kHz | Switching frequency |

Table B.2 GSC simulation parameters

| Parameter | Value | Units | Description |
|------------------|--------------|--------------|----------------------|
| P_s | 0.85 | kW | Rated power |
| $V_{n,ll}$ | 20 | V | Rated voltage |
| I_n | 3.5 | A | Rated stator current |
| f_s | 50 | Hz | Frequency |
| n | 1000-2000 | rpm | Rated speed |
| pf | 0.75 | – | Rated power factor |

Table B.3 Test bench generator nameplate ratings

Appendix C

Additional Results

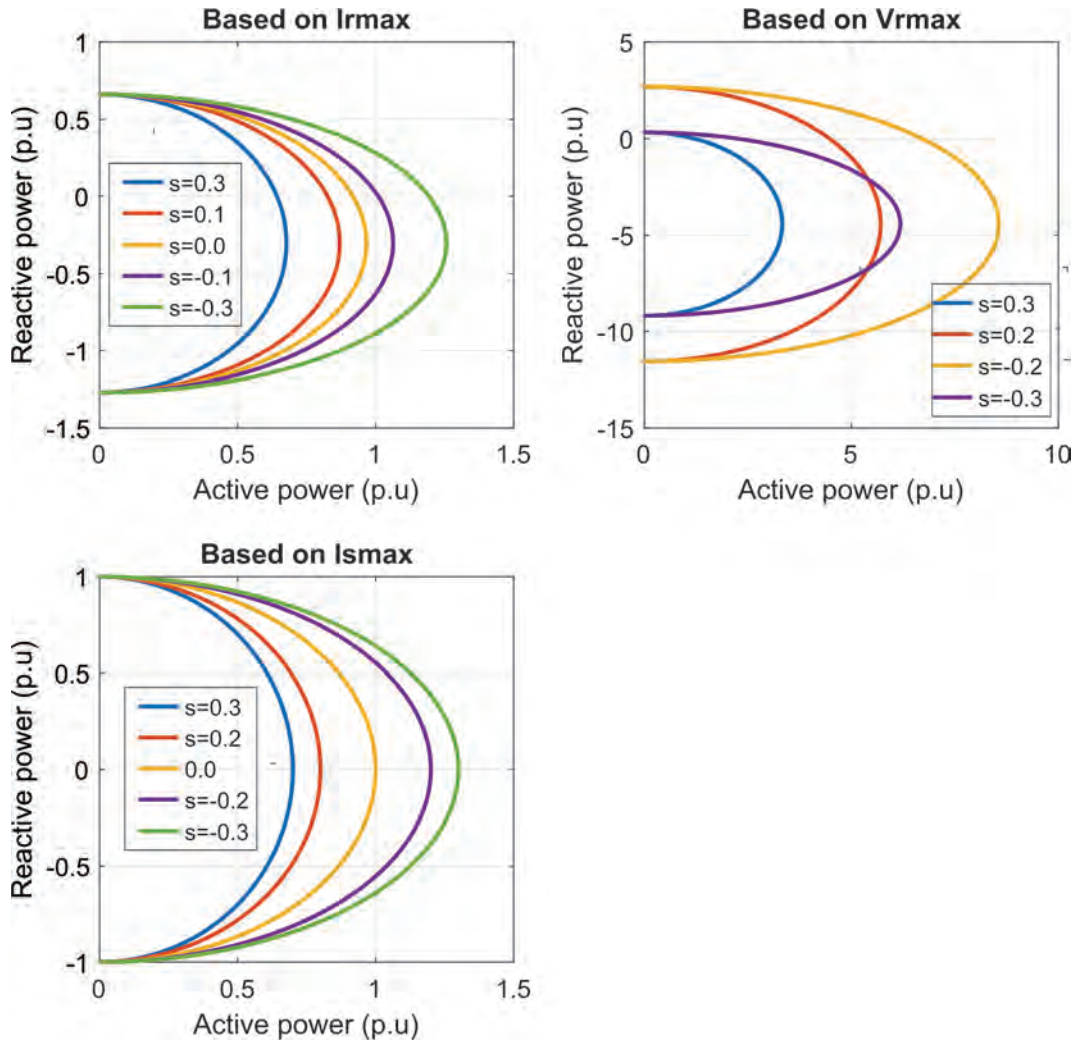


Figure C.1 Locus diagrams for different limitations in pu system where s is the slip ratio

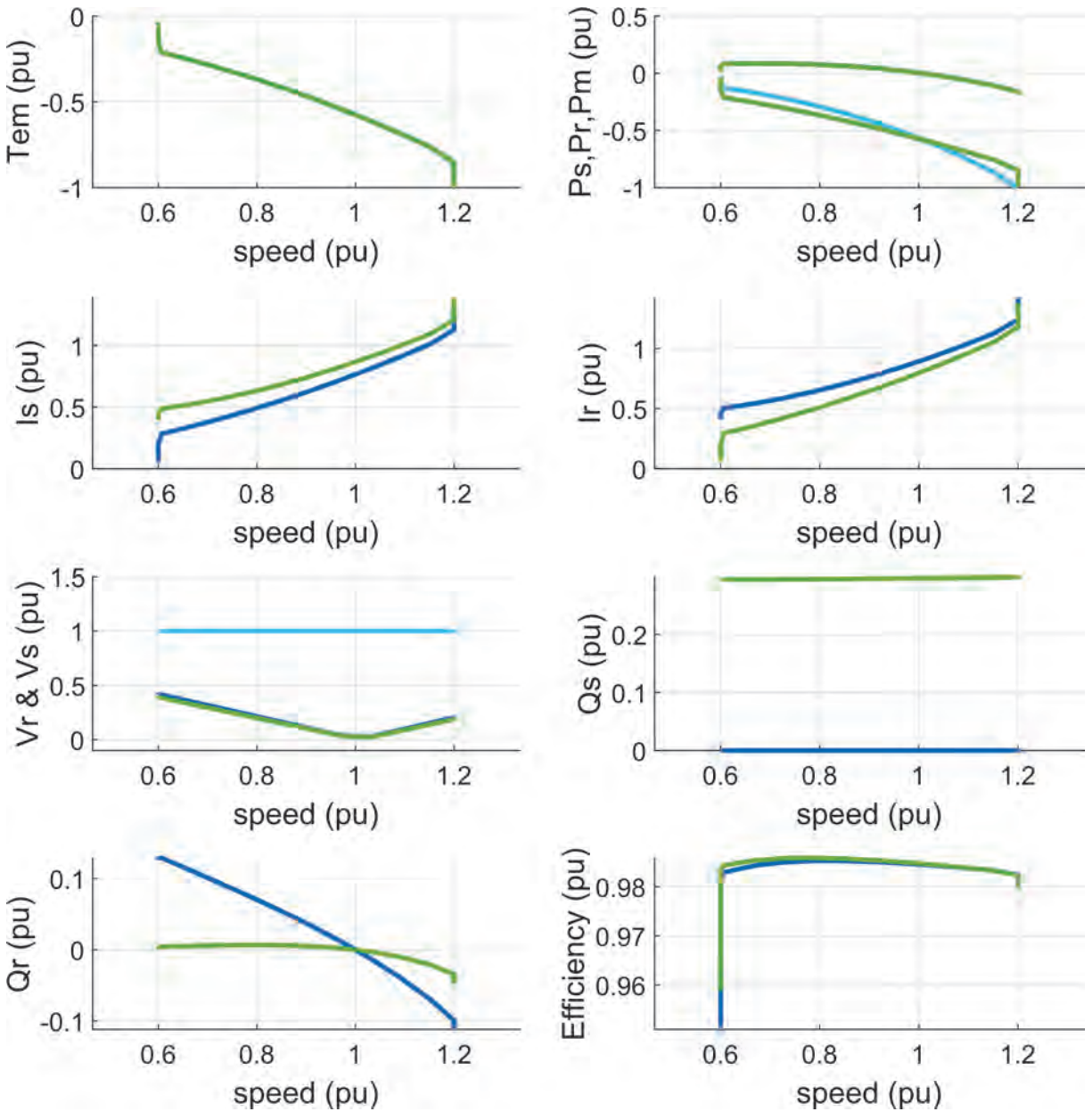


Figure C.2 Steady state capability in pu of 2 MW DFIG with $Q_s = 0$ and $i_{dr} = 0$ magnetizing strategies

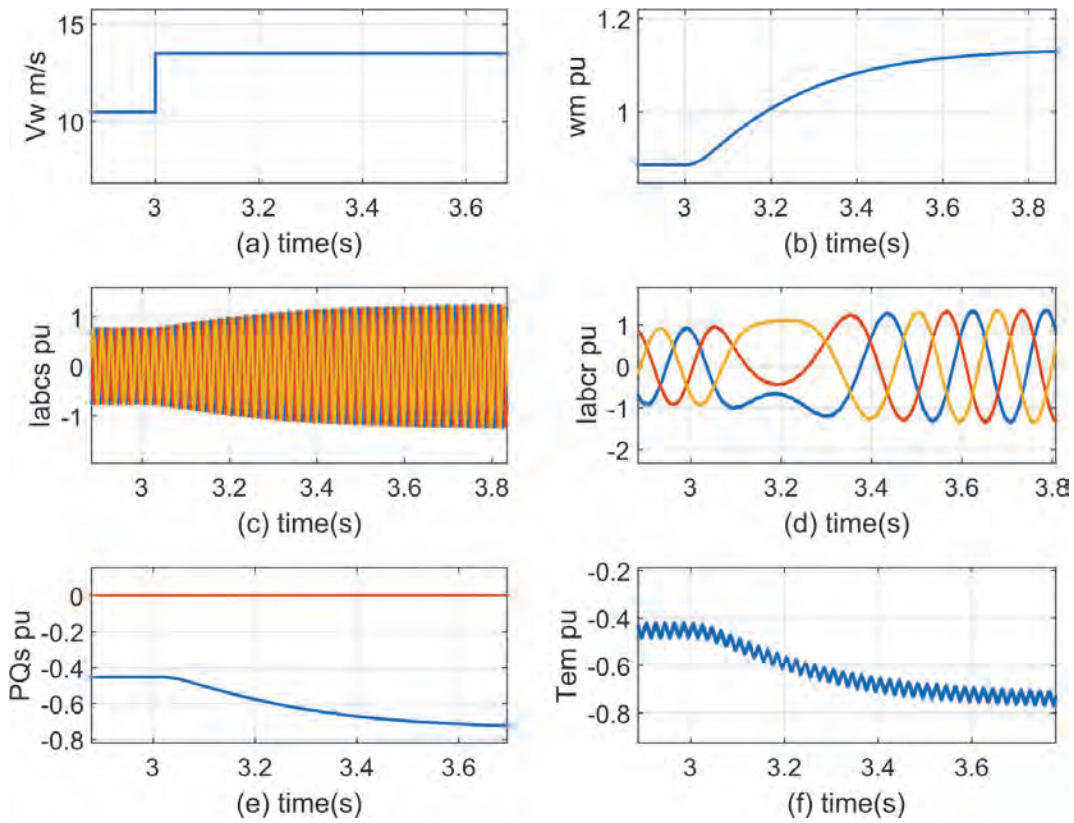


Figure C.3 Dynamic response under wind speed step change from subsynchronous to super-synchronous mode

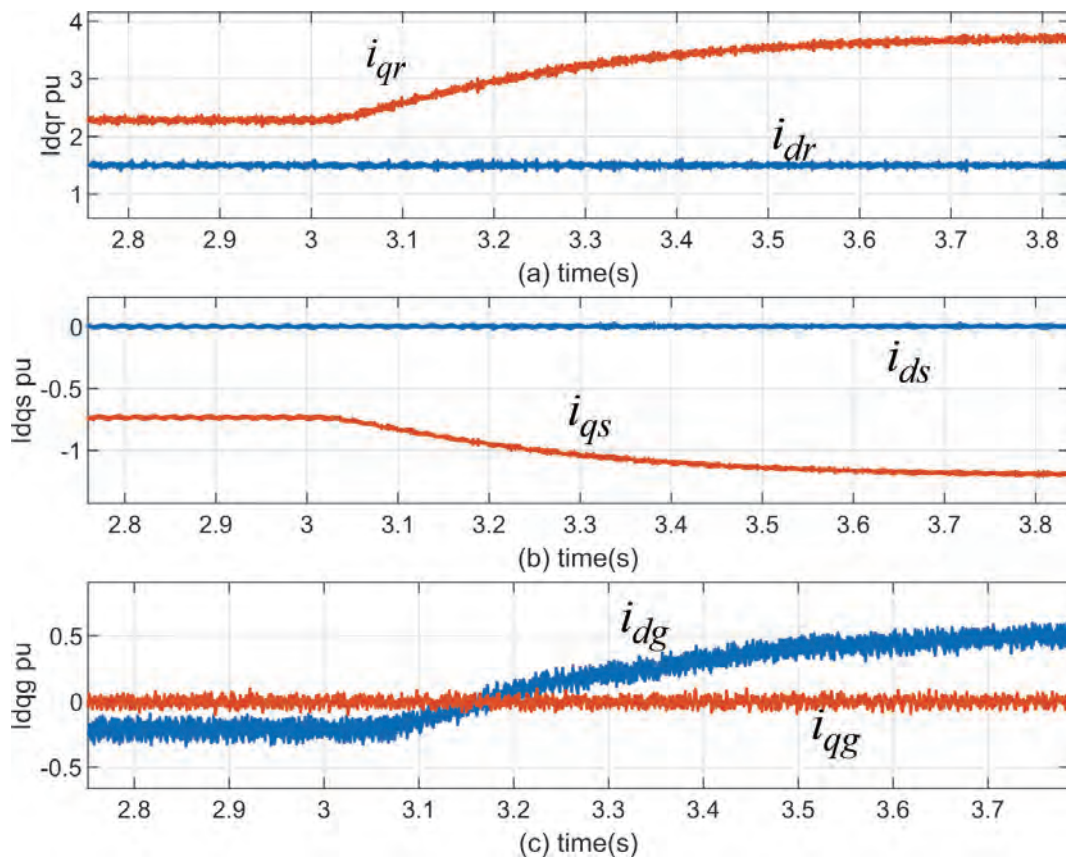


Figure C.4 Dynamic response of dq currents under wind speed step change from sub-synchronous to super-synchronous mode

Appendix D

Diagrams and Circuits

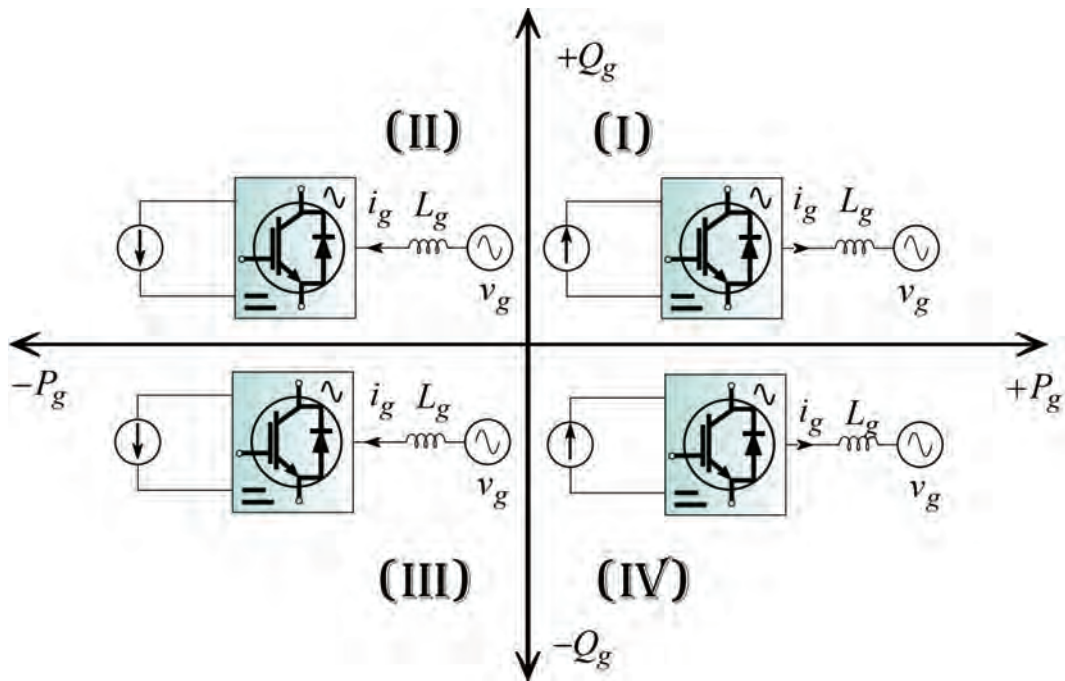


Figure D.1 Power flow between grid and dc link with PF consideration

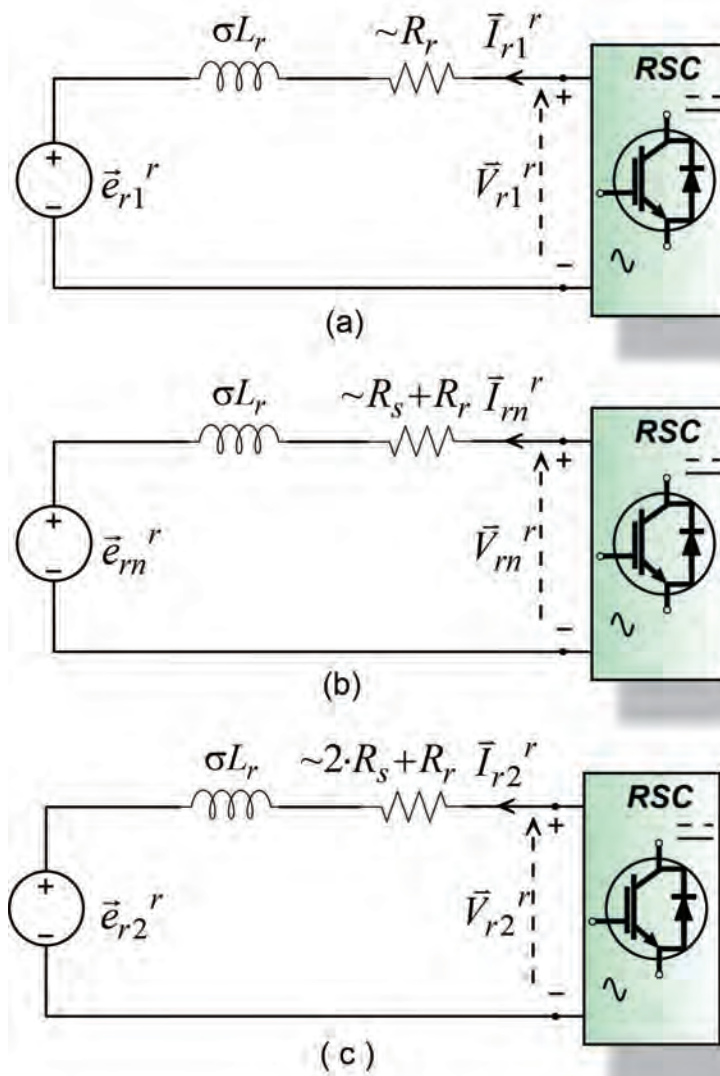


Figure D.3 Rotor side circuit diagrams under voltage dips [9] (a) Positive sequence machine (b) Natural machine (c) Negative sequence machine

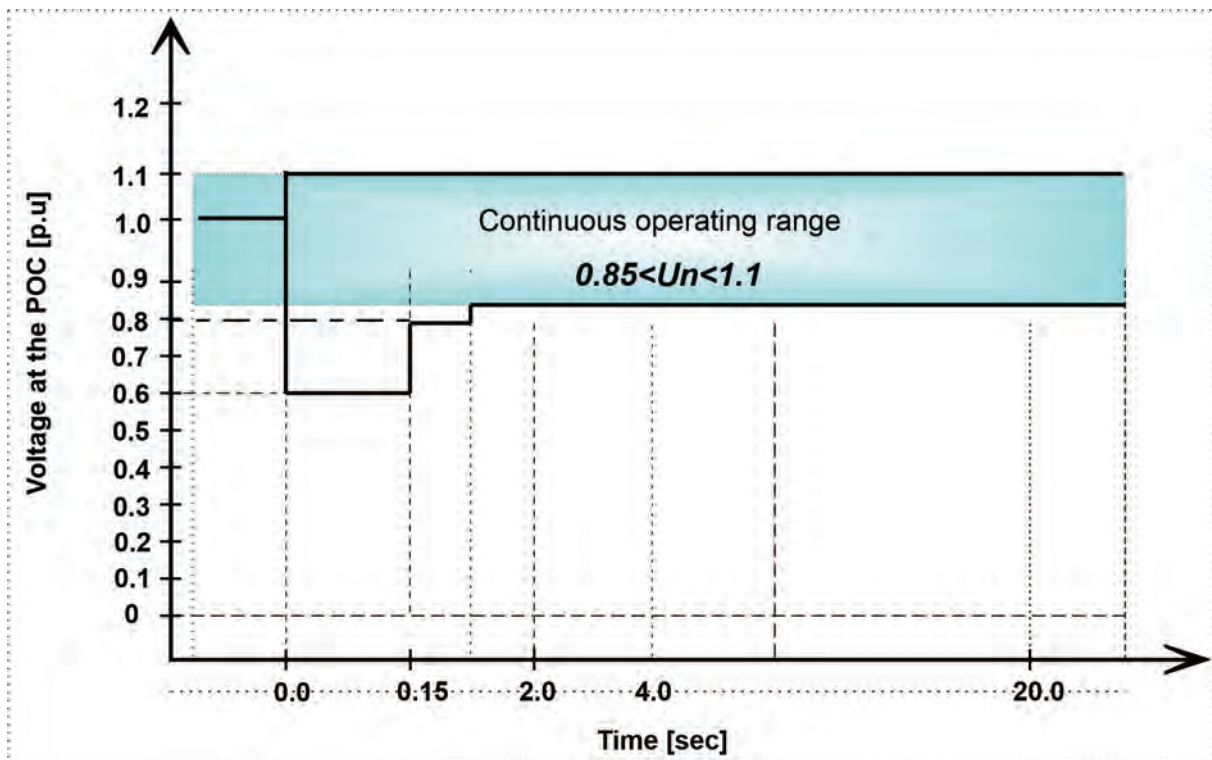


Figure D.4 South African grid code LVRT requirement for RPPs of category A1 and A2 [14]